Scratch Tests: A New Way of Evaluating the Fracture Toughness of Materials
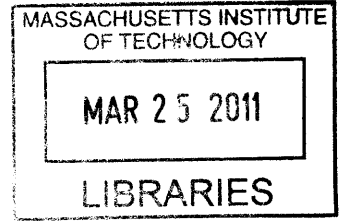
by

Ange-Therese Akono

Ingenieur Diplomée de l'Ecole Polytechnique (2009)

Submitted to the Department of Civil and Environmental Engineering
in partial fulfillment of the requirements for the degree of

Master of Science in Civil and Environmental Engineering

at the

MASSACHUSETTS INSTITUTE OF TECHNOLOGY

February 2011

Signature of Author ....
Department of Civil and Environmental Engineering
January 28, 2011

Certified by...
Franz-Josef Ulm
Professor of Civil and Environmental Engineering
Thesis Supervisor

Accepted by..
Heidi M. Nepf
Chairman, Departmental Committee on Graduate Students

Scratch Tests: A New Way of Evaluating the Fracture Toughness of Materials

by

Ange-Therese Akono

Abstract

This thesis develops, validates and implements a fracture mechanics model for the assessment of the fracture toughness of materials from scratch tests. Dimensional Analysis highlights two major processes at work during scratch tests: plastic yielding and fracture dissipation. An original set-up of controlled laboratory tests on paraffin wax allows us to identify fracture processes as predominant. An analytical model for scratch tests with a rectangular blade and a back-rake angle is then developed. This model applies to linear elastic isotropic brittle materials and links the fracture toughness to the average horizontal and vertical forces recorded in the scratch test, and to the width and depth of the scratch. Finite Element simulation show that the model is highly accurate for back-rake angles smaller than 25°. From the model, an inverse technique to predict the fracture toughness is developed and implemented. This technique is validated for scratch tests on cement paste, Jurassic limestone, red sandstone and Vosges sandstone, and applied to oil cements hydrated at high temperature and pressure. The application shows that the scratch tests is highly reproducible, almost non-destructive, and not more sophisticated than classical strength-of-materials tests; which makes this 'old' technique highly attractive for both materials research and industrial applications.

Thesis Supervisor: Franz-Josef Ulm
Title: Professor of Civil and Environmental Engineering

Contents

4

List of Figures

9

List of Tables

Acknowledgments

First and foremost, I want to thank God for His mercy and His love that have withheld me during this whole year. For His grace that accompanied me every day and made me more than an overcomer in front of every trial I have faced.

Secondly, I am very grateful to my advisor, Franz-Josef Ulm that gave me the opportunity to carry out an interesting research in a unique environment. I am thankful for the reservoir of scientific knowledge and experience, the patience and the trust that is freely imparted to each of his students.

I gratefully acknowledge the financial support by discretionary funds of the George Macomber Chair for FJU at MIT. I also gratefully acknowledge the scholarship for graduate studies that I have received from TOTAL and that has contributed to make my education more delightful. Thank you Brima Wurie for continually and steadfastly defending the interest of graduate African students. May you enjoy your retirement as these students will surely miss you.

This work would not have been possible without the continual encouragements of Pedro M. Reis that always had a positive word even in the darkest circumstances. The commitment and expertise of John Germaine was essential in building the experimental set-up. I am forever thankful to Hillary Ryan whose technical skills completed the experimental set-up. I am also thankful to Stevens Rudolph and to the MIT Central Shop for technical assistance.

A special thanks to the members of my research group: Habibi MJ, Muhannad, Amer, Alberto, Zenzile, Romain, Hegoi, Enrico, Simone and Rolland. Working with you makes each little rock and stone more concrete to me.

A great thanks to my choir: MIT Gospel Choir. To my church: Pentecostal Tabernacle. To my bishop: Brian Greene. You have contributed to make my first year in the United States and in Cambridge a warm and friendly experience.

Last but not least. To my dear friend Basile Vigneron, thank you for your faith in me and your patience. To my mother who prays day and night for me. To my brothers

and sisters so far from me. To my nephews and niece whose childhood I am missing.

Part I

General Presentation

Chapter 1

Introduction

1.1 Industrial context

The scratch test is most likely the oldest mechanics-of-materials test for property characterization. It suffices to recall the Mohs scale of mineral hardness which rationalized, in 1822, the scratch resistance into a quantitative metric for the classification of various minerals. The idea of the scratch test is simple: plowing and cutting with a scratch device the surface of a weaker material; and quantifying the scratch resistance by means of the scratch hardness [40]:

$$F_T = H_T A_L B \tag{1.1}$$

where F_T is the horizontal force applied to the apparatus; and A_{LB} is the projected load bearing area resisting the horizontal force; that is, the horizontal projection of the contact area between the scratch device and the scratched material. Thanks to progress in force and depth sensing measurement devices, the scratch test remains a popular alternative to other material property test methods, and is relevant today in many fields of engineering, ranging from macroscopic testing of adhesion properties of coatings [32], to damage and wear of metals and polymers [41, 43, 14], and strength of rocks [36, 35].

1.2 Research Objectives and Approach

The classical approach presented above (Eq. (1.1)) is based on the works of Bard and Ulm [7] and of Schei *et al.* [36, 35], and assumes that scratch tests are strength-driven. Another approach based on the works of Atkins [3, 4, 2] and Patel *et al.* [28] interprets scratch tests from a fracture perspective. Therefore, there exists two schools of thought about the scratch tests: strength versus fracture. The aim of this work is to assert the validity of each approach and to develop a framework to predict the fracture toughness from results of scratch tests. The approach developed here has three components: experimental, analytical and numerical.

1.3 Thesis Outline

This thesis is divided in three parts. Part I considers scratch tests from the perspective of Dimensional Analysis and presents the two currents of thought: strength versus fracture. Part II investigates the fracture scaling of scratch tests on paraffin wax: an analytical model, that is later supported by Finite Element simulations, is developed to explain that scaling. Part III develops an inverse technique to extract the fracture toughness from scratch tests, based on the analytical results derived in Part II. This technique is further validated by tests on cement paste, Jurassic limestone, red sandstone and Vosges sandstone. An industrial application of the approach to oil-cement slurries is also shown. In the final and conclusive part, the limits of the proposed inverse technique are discussed and further perspectives for future research are outlined.

1.4 Research Significance

Although scratch test is a common tool in the industry, the mechanisms at work during the test are not very well understood. One of the goal of this thesis is to determine whether plastic yielding or fracture dissipation is the driving process at work during the

test. Another goal of interest for industry is the determination of the fracture toughness of materials from results of scratch tests. In fact, the main advantage of scratch tests over conventional fracture testing methods, such as the three-point bending test on notched specimens or the compact tension test, is that it requires little sample preparation. Therefore it is convenient for materials that are too soft to be machined into a specimen for conventional fracture testing methods. Another advantage is the small amount of material required to get meaningful data. Finally, the test is almost non-destructive allowing the samples to be reused for other testing methods.

Chapter 2

Dimensional Analysis of Scratch Tests

This chapter introduces the scratch tests and the quantities involved through a dimensional analysis. The focus is on identifying the relevant mechanical and geometrical quantities that need to be considered in scratch test analysis, be this from a strength or fracture perspective.

2.1 Introduction

A scratch test consists in pushing a tool of a given geometry at a controlled depth d and with a constant velocity into the material as displayed in Fig. 2-1. In this thesis, the tool considered is a blade of rectangular cross section, width d and thickness t, and inclined at an angle θ with regard to the vertical axis. θ is also called the back-rake angle. During the test, a horizontal force F_T and a vertical force F_V are generated. If we assume an Amontons-Coulomb friction law, the horizontal and vertical forces are related to θ and to the friction coefficient $\mu = \tan \beta$ between the blade and the material by:

$$F_V = F_T \tan(\theta + \beta) \tag{2.1}$$

Finally, the horizontal projected contact area for a rectangular blade is $A_{LB} = wd$; therefore the scratch hardness is equal to:

$$H_T = \frac{F_T}{wd} \qquad (2.2)$$
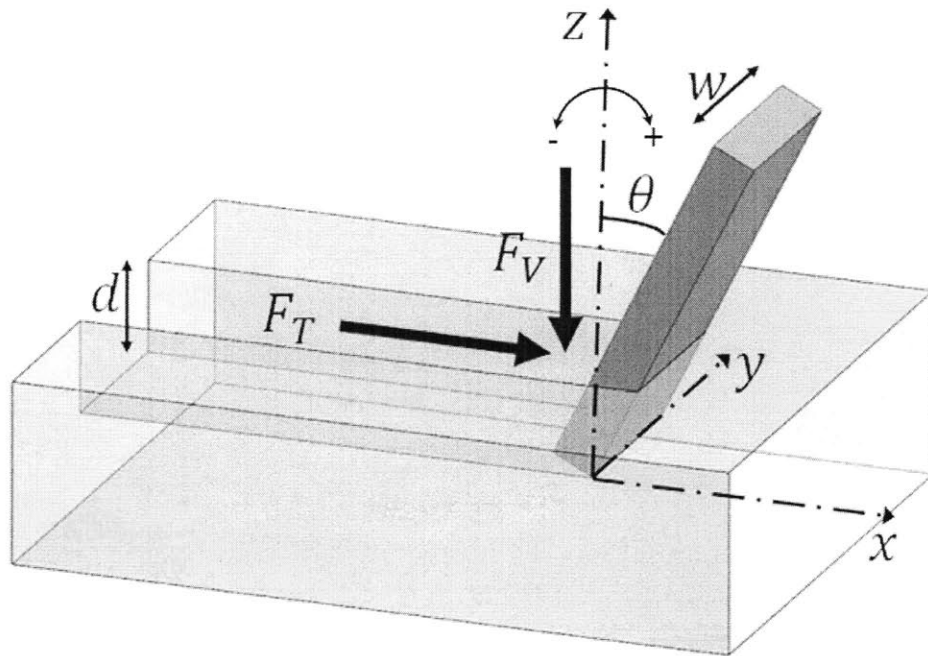
Figure 2-1: Schematic of a scratch test. Courtesy of Pedro M. Reis.

Provided the test is slow enough to avoid rate effects, and provided the frictional effects between the blade and the material are negligible, plastic yielding and fracture propagation are the two major dissipative processes that can occur. During plastic yielding, a part of the material is permanently displaced to the sides and to the front of the groove left by the blade. On the other hand, during fracture propagation, chips of material are removed as the blade moves into the material. In this chapter we will review these approaches in the light of existing approaches found in the literature.

To this end, we will first proceed with a dimensional analysis. Then we will present the two currents of thought on scratch tests. First, the strength interpretation with the work of Schei *et al.* [36, 35] and Bard and Ulm [7]. Then the fracture interpretations with the work of Atkins [3, 2, 4] and Patel *et al.* [28]. Finally, we will discuss the validity and limits of each approach.

2.2 Dimensional Analysis

The quantity of interest for a strength-driven, respectively fracture-driven, process is the ultimate strength σ_u of dimension function $[L^{-1}MT^{-2}]$, respectively the fracture toughness K_c of dimension function $[L^{-1/2}MT^{-1}]$. For 2-D problems, the scaling of the nominal stress at failure, σ_N, is given by two size effect laws [9, 10]: in the case of large scale plastic yielding, and if the material is perfectly plastic, then σ_N is equal to the ultimate strength, σ_u, of the material. On the other hand, if fracture dissipation is predominant over plastic dissipation, and within the framework of Linear Elastic Fracture Mechanics (LEFM), σ_N is inversely proportional to the square root of D, where D is a length parameter of the system(Fig. 2-2).

$$\sigma_N = \sigma_u, \qquad \text{Strength Theory} \qquad (2.3)$$

$$\sigma_N = \frac{K_c}{\sqrt{D}}, \qquad \text{Linear Elastic Fracture Mechanics} \qquad (2.4)$$

For scratch tests, the nominal strength is given by the scratch hardness:

$$\sigma_N \equiv H_T \qquad (2.5)$$
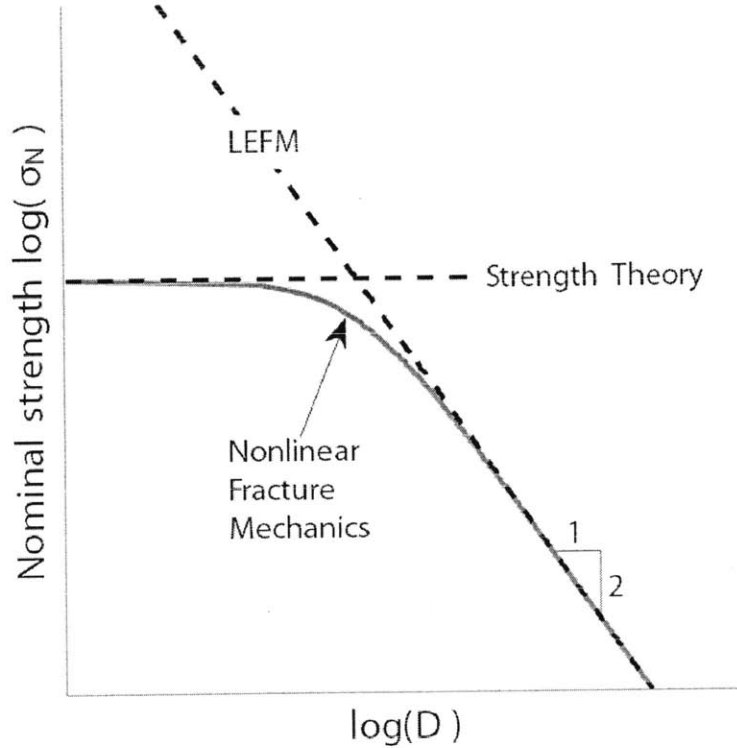
Figure 2-2: Strength and fracture scaling. Source [9, 10].

2.2.1 Strength Scaling of Scratch Tests

The key quantity for strength models of scratch tests is the scratch hardness H_T defined by Eqs. (1.1) and (2.2). This scratch hardness depends on the following quantities:

- The elasto-plastic and fracture properties of the scratched material: Young's modulus E, Poisson's ratio ν, ultimate tensile strength σ_0, and fracture toughness K_c

- The geometric parameters of the scratch test: the width of the blade w, the depth of scratch d, the back-rake angle θ and the friction coefficient μ.

That is:

$$H_T = f\left(E, \nu, \sigma_0, K_c, w, d, \theta, \mu\right) \tag{2.6}$$

26

The exponent matrix in a LMT base dimension system reads:

$$
\begin{array}{c|c||cccccccc}
 & [H_T] & [E] & [\nu] & [\sigma_0] & [K_c] & [w] & [d] & [\theta] & [\mu] \\
\hline\hline
L & -1 & -1 & 0 & -1 & -1/2 & 1 & 1 & 0 & 0 \\
M & 1 & 1 & 0 & 1 & 1 & 0 & 0 & 0 & .0 \\
T & -2 & -2 & 0 & -2 & -2 & 0 & 0 & 0 & 0
\end{array}
\tag{2.7}
$$

The rank of the matrix is $k = 2$. By choosing (d, σ_0) as a system of dimensional independent variables, the Π-theorem [15] allows reducing Eq. (2.6) to:

$$
H_T = \sigma_0 \times \Pi \left(\frac{\sigma_0}{E}, \nu, \mathcal{I} = \frac{d}{(K_c/\sigma_0)^2}, \frac{w}{d}, \theta, \mu \right)
\tag{2.8}
$$

where Π is the dimensionless hardness-to-strength ratio that depends on dimensionless parameters relevant to the scratch geometry (width-to-depth ratio w/d; back-rake angle θ) and the material (strength-to-stiffness ratio σ_0/E, friction coefficient μ, and Irwin's number $\mathcal{I} = d/(K_c/\sigma_0)^2$). $\mathcal{I}$ quantifies the transition from a pure strength process, $\mathcal{I} \ll 1$, to a pure fracture process, $\mathcal{I} \gg 1$.

2.2.2 Fracture Scaling of Scratch Tests

Classical Dimensional Analysis With a Focus on Fracture Scaling

We are interested in:

$$
F_T = f(w, d, E, K_c, \sigma_0, \theta, \mu)
\tag{2.9}
$$

The exponent matrix in a LMT baste system reads:

$$
\begin{array}{c|c||ccccccc}
 & [F_T] & [w] & [d] & [E] & [K_c] & [\sigma_0] & [\theta] & [\mu] \\
\hline\hline
L & 1 & 1 & 1 & -1 & -1/2 & -1 & 0 & 0 \\
M & 1 & 0 & 0 & 1 & 1 & 1 & 0 & 0 \\
T & -2 & 0 & 0 & -2 & -2 & -2 & 0 & 0
\end{array}
\tag{2.10}
$$

The rank of the matrix is $k = 2$. Choosing d and K_c as dimensionally independent variables, the Π-theorem [15] allows to construct the following invariants:

$$\Pi = \frac{F_T}{K_c d^{3/2}} = F\left(\Pi_1 = \frac{w}{d}; \Pi_2 = \frac{Ed^{1/2}}{K_c}; \Pi_3 = \frac{\sigma_0 d^{1/2}}{K_c}; \theta, \mu\right) \tag{2.11}$$

Dimensional Analysis With an Extended Base Dimension System

We now consider an extended base dimension system, $[Q] = L_x L_y L_z M T^{-2}$, where L_i stands for the length base dimensions in the $i = x, y, z$ directions. In fact, extended base dimension systems apply when the length dimension in one direction is independent of the characteristic base dimension of length in the others direction. In this case, we assume a scale separability condition: the scratch direction x is much greater than the width w of the scratch device, and w is much greater than the depth of the scratch d, so that the three length quantities can be expressed in separate length units:

$$d \ll w \ll x \tag{2.12}$$

Given this scale separability condition, we employ a $L_x L_y L_z M T$ base dimension system, in which we express the physical quantities of the problem in the form:

$$[Q] = L_x^\alpha L_y^\beta L_z^\gamma M^\delta T^\epsilon \tag{2.13}$$

Therefore, we need to return to the very definition of the involved quantities. For instance, the fracture toughness is related to the Young's modulus E and to fracture energy G_f [1] by Eq. (2.14) [26, 34]:

$$K_c = \sqrt{\frac{EG_f}{\kappa}} \tag{2.14}$$

---

[1]G_f is the energy per unit surface created by fracture.

where $\kappa = 1$ in plane stress and $\kappa = 1 - \nu^2$ in plane strain. Therefore the dimension function of K_c can be related to that of E and G_f by:

$$[K_c] = [E]^{1/2} [G_f]^{1/2} \tag{2.15}$$

In its turn, E is a longitudinal modulus and its dimension function in the extended base dimension reads:

$$[E] = [\sigma_{xx}] = \frac{[F_T]}{L_y L_z} \tag{2.16}$$

where $[F_T] = L_x M T^{-2}$ is the dimension function of the scratch force, and $[A] = [wd] = L_y L_z$ is the dimension function of the load bearing area of this force. In return, the dimension function of the fracture energy G_f represents the energy per unit of crack surface Γ created, which is oriented in the z-direction; thus $[\Gamma] = L_x L_y$. Prior to fracturing, the energy is equal to the work provided to the system by the scratch force, thus $[W] = [F_T] L_x$; hence the dimension function of the fracture energy:

$$[G_f] = \frac{[W]}{[\Gamma]} = \frac{[F_T] L_x}{L_x L_y} \tag{2.17}$$

It then follows from definition Eq. (2.15):

$$[K_c] = \frac{[F_T]}{L_y L_z^{1/2}} = \frac{L_x M T^{-2}}{L_y L_z^{1/2}} \tag{2.18}$$

29

The exponent matrix in the extended base dimension system $L_x L_y L_z M T^{-2}$ thus reads:

	$[F_T]$	$[E]$	$[\nu]$	$[\sigma_0]$	$[K_c]$	$[w]$	$[d]$	$[\theta]$	$[\mu]$
L_x	1	1	0	1	1	0	0	0	0
L_y	0	-1	0	-1	-1	1	0	0	0
L_z	0	-1	0	-1	$-1/2$	0	1	0	0
M	1	1	0	1	1	0	0	0	0
T	-2	-2	0	-2	-2	0	0	0	0

$$(2.19)$$

The rank of the matrix is $k = 3$. By taking (K_c, d, w) as set of dimensionally independent variables, the Π-theorem [15] provides:

$$F_T = K_c w \sqrt{d} \times \Pi \left(\frac{\sigma_0}{E}, \nu, \mathcal{I} = \frac{w}{(K_c/\sigma_0)^2}, \theta, \mu \right) \tag{2.20}$$

A comparison of Eqs. (2.4) and (2.20) yields:

$$H_T \propto \frac{K_C}{\sqrt{d}} \tag{2.21}$$

Therefore the scaling proposed here captures the size effect inherent to fracture processes.

After having established the expected scaling for both strength or fracture in a scratch test, we will now present the approaches developed in the past to study scratch tests from a perspective of a strength-driven or fracture-driven process.

2.3   Scratch Tests: a Strength Perspective

The strength interpretation of scratch tests is based on the works of Schei *et al.* [36, 35] and of Bard and Ulm [7]. Both approaches relate the uniaxial compressive strength of the material, UCS, to the scratch hardness using empirical, analytical and numerical arguments.
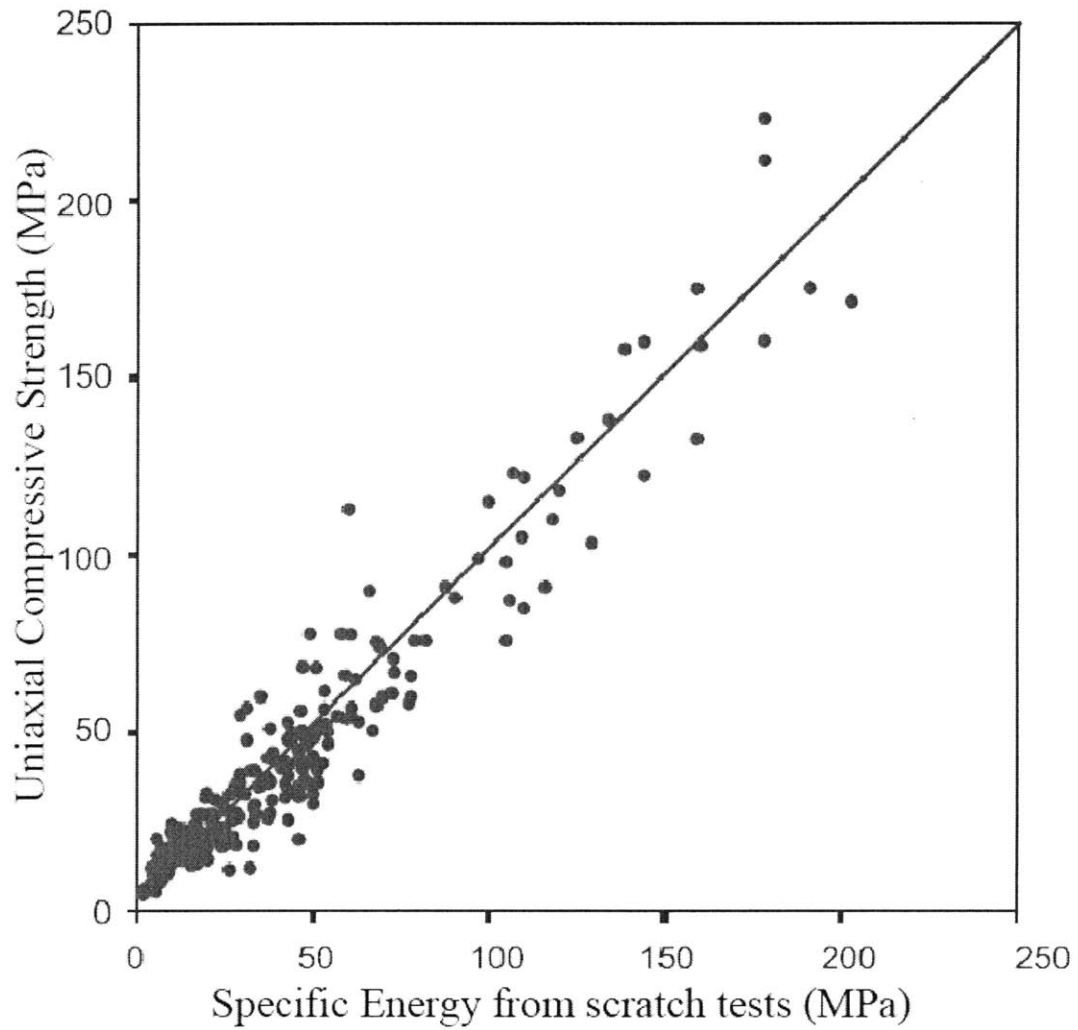
Figure 2-3: Correlation between the intrinsic specific energy ε and the uniaxial compressive strength UCS for 92 sandstones, 86 limestones, 19 shales and 4 chalks. Courtesy of Epslog S. A.

2.3.1 Schei *et al.* [35, 36]

Schei *et al.* [35, 36] studied the scratch testing of sedimentary rocks with a blade of rectangular cross section and with a back-rake angle, $\theta \approx 15° - 20°$. For a given width w of the blade, they witnessed two modes of failure of the material, depending on the depth d of scratch:

- A ductile mode, at small depths, associated with yielding of the material. In this mode, both the mean horizontal force and the mean horizontal peak force vary linearly with d.

- A brittle mode, at higher depths, associated with fracture propagation and the chipping of the material. In this mode, the variations of both the mean horizontal force and the mean horizontal peak force with d were non-linear. More precisely, both quantities could be approximated by a parabola going through the origin.

The transition from the ductile mode to the brittle mode occurred at a depth defined by:

$$d^* = \left(\frac{K_c}{UCS} \right)^2 \tag{2.22}$$

where K_c is the fracture toughness and UCS the uniaxial compressive strength. A cutting model was developed for the ductile mode. It is based on the concept of an intrinsic specific energy, ε, which is the energy strictly required to cut a unit volume of material, discarding any friction effects. For a perfectly sharp blade, the intrinsic specific energy is defined by:

$$\varepsilon = \frac{dF_T}{dA_{LB}} = \left. \frac{dF_T}{d(wd)} \right|_{w=constant} \tag{2.23}$$

where $A_{LB} = wd$ is the projected contact area of a rectangular blade. For several limestones, sandstone, shales and chalks, a close correlation was found between the specific energy ε and the uniaxial compressive strength UCS, as shown in Fig. 2-3.

32

2.3.2   Bard and Ulm [7]

Bard and Ulm [7] developed a lower-bound yield design approach for the scratch test, which neglects elastic contributions ($\sigma_0/E \to 0$) and fracture processes ($\mathcal{I} \ll 1$). The lower-bound solutions were then validated by means of Finite Element simulations and upper-bound yield design approaches. The relationship between the scratch hardness H_T and UCS, assuming a frictionless blade-material contact, are listed in Table 2.3.2. They found that the ratio of the scratch hardness, H_T, to the uniaxial compressive strength, UCS, was always strictly greater than unity.

Criterion	Hardness normalized by the UCS	UCS-cohesion relation
Tresca	$\frac{H_T}{UCS} = 1 + \sin\theta$	$UCS = 2c$
Von Mises	$\frac{H_T}{UCS} = \frac{2}{\sqrt{3}}(1 + \sin\theta)$	$UCS = \sqrt{3}k$
Mohr-Coulomb	$\frac{H_T}{UCS} = \dfrac{(1-\sin^2\theta)(1-\sin\phi)}{1-\sin\theta\sqrt{1-\sin^2\phi\cos^2\theta}-\sin\phi\cos^2\theta}$	$UCS = \frac{2\cos\phi}{1-\sin\phi}c$
Drucker-Prager	$\frac{H_T}{UCS} = \dfrac{2}{3}\dfrac{(1-\sin^2\theta)(\sqrt{3}-\alpha)}{\sqrt{1+\frac{\alpha^2}{3}}-\sin\theta\sqrt{1+\frac{\alpha^2}{2}-\alpha^2\cos^2\theta}-\alpha\cos^2\theta}$	$UCS = \frac{3}{\sqrt{3}-\alpha}k$

Table 2.1: Values of the hardness normalized by the uniaxial compressive strength for the four strength criteria considered. c is the cohesion and k is the ultimate shear strength. Source [7].

Bard and Ulm [7] then analyzed three series of 20 scratch tests each on a cement paste material prepared at a water-to-cement ratio of 0.44. The three series corresponded to three different widths of the blade w=2.5, 5, 10 mm. The back-rake angle was $\theta = 15°$ while the depth of the scratch d ranged from 0.1 to 0.6 mm. The intrinsic specific energy ε defined by Eq. (2.23) was 54.3, 37.9 and 26.8 MPa, respectively for $w = 2.5$, 5, 10 mm. The decrease of the intrinsic specific energy with the width and the curved shape of the plot (F_T, wd), displayed in Fig. 2-4, indicates that the scratch hardness is not a constant but that it also depends on the contact area. This result is in contradiction with the linear scaling predicted by definition Eq. (2.2) of the scratch hardness. Actually, that linear scaling is valid only for small values of wd. That is why Bard and Ulm [7] propose

33
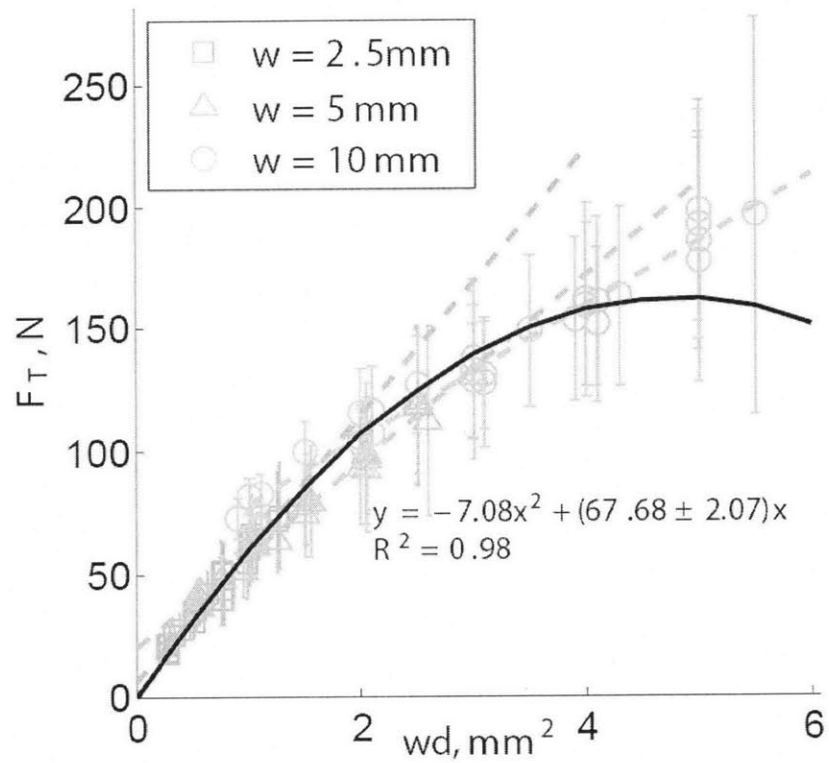
Figure 2-4: Schei's approach versus Bard's approach. $\varepsilon = 54.3, 37.9, 26.8$ MPa for respectively $w = 2.5, 5, 10$ mm. Following Eq. (2.24), $H_T = 60$ MPa. Scratch tests on cement paste w/c=0.44. Tests carried out by Epslog S. A.; data courtesy of Schlumberger.

another definition of the scratch hardness as the initial slope of the function $F_T(wd)$:

$$H_T = \left.\frac{dF_T}{d(wd)}\right|_{wd=0} \tag{2.24}$$

This initial slope is conveniently determined from a quadratic fitting of the curve (F_T, wd) as illustrated in Fig. 2-4. Eq. (2.24) applied to cement paste yields : $H_T = 67.7 \pm 2.1$ MPa. Moreover, if we assume a Tresca criterion, respectively Von Mises criterion, the UCS is found to be equal to 53.8 ± 1.7 MPa, respectively 46.6 ± 1.4 MPa. Both values are not far off the experimental value of the uniaxial compressive strength: $UCS^{\text{exp}} = 43 \pm 2$ MPa.

Therefore it results from Schei et al.'s [35, 36] and Bard and Ulm's [7] work that the strength interpretation is valid for small values of the horizontal projected load bearing area $A_{LB} = wd$. Schei et al. [35, 36] predict that the ratio of the scratch hardness to the uniaxial compressive strength is close to unity. However Bard and Ulm [7] show that this ratio is always strictly greater than unity. Finally, for high values of wd, F_T varies in a non-linear way with wd. This non-linearity is characteristic of size effect and hints toward fracture.

2.4   Scratch Tests: a Fracture Perspective

Atkins' [3, 4, 2] and Patel et al.'s [28] models rely on slip line field theory, which is an upper bound model that assumes that energy dissipation occurs along a shear plane of given inclination ϕ with regard to the horizontal axis as shown in Fig. 2-5. An heuristic energy balance shows that the external work provided by the horizontal force is either stored in the material as strain energy or dissipated in fracture, friction and plastic processes:

$$dU_{ext} = F_T dx = dU_{fract} + dU_{friction} + dU_{plast} \tag{2.25}$$
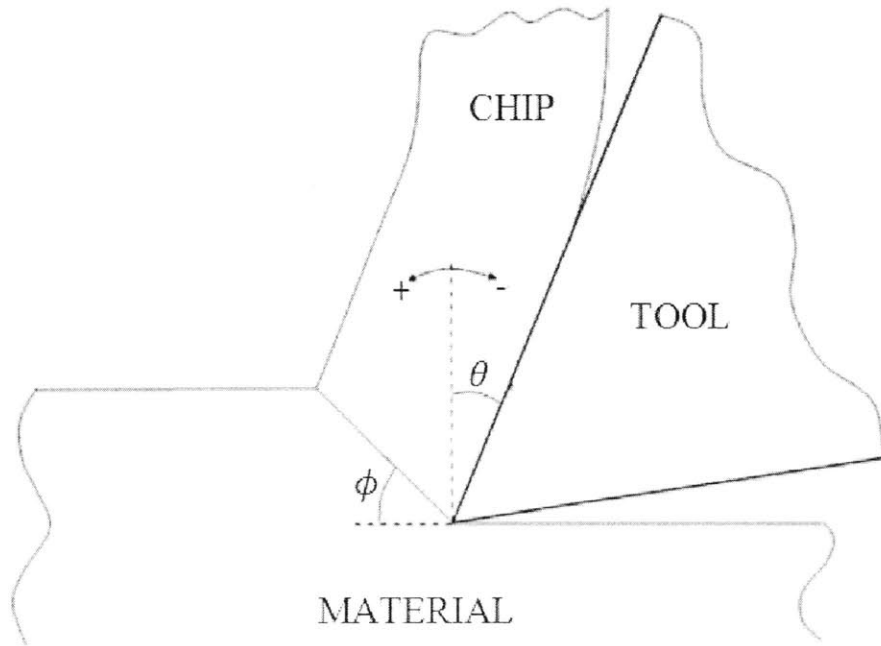
Figure 2-5: Chip formation by shear. θ is the back-rake angle and ϕ is the shear plane angle. Source [42].

The strength properties come into play via plastic dissipation, and the fracture properties via crack propagation. The fracture dissipation is $dU_{fract} = G_f w dx$ where G_f is the fracture energy, that is the energy required to create a unit of crack surface. The main difference between cutting and scratching is that in cutting the blade's width is greater or equal than that of the material whereas in scratch testing the blade width is significantly smaller to avoid boundary's effects. The differences between Atkins' [3, 4, 2] and Patel *et al.*'s [28] approaches reside in the way they evaluated both the incremental friction work and the incremental plastic work.

2.4.1 Atkins [3, 4, 2]

Atkins [3, 4, 2] accounts for friction dissipation via an Amontons-Coulomb friction model with a friction coefficient μ:

$$dU_{friction} = F_T sec(\beta + \theta) \sin \beta \frac{\sin \phi \, dx}{\cos(\phi + \theta)} \tag{2.26}$$

The plastic dissipation is given by the area under the stress-strain curve as $\int k \, d\gamma$, where k is the material shear yield stress and γ is the shear strain on the shear plane. It is proposed:

$$dU_{plast} = k\gamma wd \, dx; \quad \gamma = \frac{1}{\tan \phi} + \tan(\phi + \theta) \tag{2.27}$$

Therefore, Eq. (2.25) relates the horizontal force to the fracture energy G_f and to the shear yield stress k according to:

$$\frac{F_T}{w} = k\frac{\gamma}{Q}d + \frac{G_f}{Q} \tag{2.28}$$

where Q is a friction correction factor given by:

$$Q = 1 - \frac{\sin \beta \sin \phi}{\cos(\beta + \theta) \cos(\phi + \theta)} \tag{2.29}$$

The shear plane angle ϕ is determined via a Merchant's minimization scheme. This scheme consists in replacing Q and γ by their respective expressions in Eq. (2.28) and then minimizing the resulting expression of F_T with regard to ϕ. This yields the following implicit equation for ϕ:

$$\left[1 - \frac{\sin \beta \sin \phi}{\cos(\beta + \theta) \cos(\phi + \theta)} \right] \left[\frac{1}{\cos^2(\phi + \theta)} - \frac{1}{\sin^2 \phi} \right]$$
$$= -[\cot \phi + \tan(\phi + \theta) + Z] \left[\frac{\sin \beta}{\cos(\beta + \theta)} \left\{ \frac{\cos \phi}{\cos(\phi + \theta)} + \frac{\sin \phi \sin(\phi + \theta)}{\cos^2(\phi + \theta)} \right\} \right] \tag{2.30}$$

Once ϕ is known, the fracture energy G_f and the shear strength k are determined using Eq. (2.28), and from the slope and the positive intercept of the curve (F_T, d).

2.4.2 Patel *et al.* [28]

Unlike Atkins [3, 4, 2], Patel *et al.* [28] postulate the existence of a horizontal force $-wG_f\underline{e}_x$ that is responsible for the crack propagation. This force acts on the blade-material interface and enters the force balance equation[1]. In particular, the shear force acting on the blade-material interface is not $F_T \sin(\alpha) + F_V \cos\alpha$ but $(F_T - wG_f)\sin\alpha + F_V \cos\alpha$. Consequently, the incremental friction dissipation reads:

$$dU_{friction} = [(F_T - wG_f)\sin\alpha + F_V \cos\alpha]\frac{\sin\phi}{\cos(\phi - \alpha)}dx \qquad (2.31)$$

The plastic dissipation is calculated as the work of the shear force F_s acting on the shear plane. Moreover the material is assumed to obey a Tresca criterion so that F_s is equal to half the material tensile yield strength σ_y times the width of cut w and times the length of the shear plane $d/\sin\phi$. Consequently, the plastic dissipation is postulated to read as:

$$dU_{plast} = \frac{\sigma_y}{2}\frac{wd}{\sin\phi}\frac{\cos\alpha}{\cos(\phi - \alpha)} \qquad (2.32)$$

By equating the external work and the sum of the fracture, plastic and friction dissipation, and by using a Merchant's minimization scheme to determine ϕ, Patel *et al.* [28] arrive at:

$$\frac{F_T}{w} = G_f + \sigma_y d\sqrt{1 + \frac{2}{\sigma_y d}\frac{F_V}{w}} \qquad (2.33)$$

---

[1]This approach cannot be supported by LEFM and by thermodynamics of irreversible processes. The fracture energy G_f, or more precisely the energy release rate G, is a thermodynamic force equal, with opposite sign, to the derivative of the potential energy with regard to the crack surface Γ. As such it is a thermodynamic force that does not appear explicitly in any equilibrium equation, i.e. force balance or momentum balance.

2.4.3 Discussion

Atkins' method [3, 4, 2] is applied to the cement paste material of section 2.3.2 as well as to red sandstone and Vosges sandstone, materials that will be further considered in Part III of this thesis (see Chapter 6). The MATLAB algorithm used to derive G_f and k assumes that the friction coefficient μ is constant for all w and d (this algorithm is given in Appendix A). For cement paste, G_f ranges from 1.79×10^3 N/m for $w = 2.5$ mm to 4.06×10^3 N/m for $w = 10$ mm; whereas k decreases from 13.7 MPa for $w = 2.5$ mm to 6.6 MPa for $w = 10$ mm. For red sandstone, G_f ranges from 24.88×10^3 N/m for $w = 2.5$ mm to 9.09×10^3 N/m for $w = 15$ mm; whereas k decreases from 37.7 MPa for $w = 2.5$ mm to 8.8 MPa for $w{=}15$ mm. Finally, for Vosges sandstone, G_f is negative for $w = 2.5$ and 5 mm, then it increases from 2.71×10^3 N/m for $w = 10$ mm to 3.85×10^3 N/m for $w = 15$ mm. As for k, it ranges from 12.5 MPa for $w = 2.5$ mm to 6.9 MPa for $w = 15$ mm. The values of G_f and k are displayed in Table 2.2

Atkins [3, 4, 2] assumes that the intercept of $F_T(d)$ is always positive. We could not confirm this assumption for small widths. For instance, for Vosges sandstone and for $w = 2.5$ and 5 mm, a negative intercept was found, that resulted in negative values of the fracture energy. Moreover, both G_f and k appear to be size-dependent. For cement paste and Vosges sandstone, G_f globally increases with w and for red sandstone G_f decreases with w. As for k, it globally decreases with w. Finally, for all three materials, G_f is one order of magnitude greater than the values expected. In fact, typical values of the fracture energy for cement paste and rock materials are $10 - 100$ N/m [29].

Patel *et al.*'s Merchant minimization scheme [28] was applied to the same materials (the MATLAB script used is given in Appendix B). For cement paste, G_f increases from 1.00×10^3 N/m to 3.29×10^3 N/m whereas σ_y decreases from 34.1 MPa to 14.1 MPa. For red sandstone, G_f ranges from 18.08×10^3 Nm/ to 5.52×10^3 N/m whereas σ_y decreases from 72.4 MPa to 19.4 MPa. Finally, for Vosges sandstone, G_f increases from 0 N/m to 1.76×10^3 N/m whereas σ_y decreases from 33.7 MPa to 18.0 N/m. These data are displayed in Table 2.3

Material	width	G_f ($\times 10^3$ N/m)	ΔG_f ($\times 10^3$ N/m)	k (MPa)	Δk (MPa)
Cement Paste	2.5	1.79	0.02	13.7	0.0
	5	3.05	0.06	9.5	0.1
	10	4.06	0.12	6.6	0.2
Red Sandstone	2.5	24.88	0.37	37.7	0.4
	5	16.14	0.14	19.8	0.1
	10	8.33	0.29	10.5	0.5
	15	9.09	0.25	8.8	0.3
Vosges Sandstone	2.5	-0.27	0.00	12.5	0.0
	5	-0.98	0.00	10.7	0.0
	10	2.71	0.03	9.0	0.0
	15	3.85	0.06	6.9	0.1

Table 2.2: Atkins' method [3, 4, 2] applied to cement paste, red sandstone and Vosges sandstone. The cement paste is the material presented in section 2.3.2. For each material, μ was assumed to be independent of w and d. Tests carried out by Epslog S. A.; data courtesy of Schlumberger.

The same observations as for Atkins' [3, 4, 2] model apply here. That is, G_f is a decreasing function of w for both cement paste and Vosges sandstone whereas, for all materials, σ_y is a decreasing function of w. Therefore both Atkins' [3, 4, 2] and Patel et al.'s [28] methods fail to capture the size effects related to fracture, as well as the size-independence of the fracture properties.

2.5 Chapter Summary

The aim of this chapter was to present and confront the two currents of thought on scratch tests: strength versus fracture. The strength approach predicts a linear scaling between the horizontal force F_T and the projected contact area wd and is valid only for small values of wd. In return the fracture models presented here fail to capture the size effects related to fracture, and they predict size-dependent fracture properties. This motivates the work presented in this thesis, which will focus on the development of a new framework to better understand fracture dissipation and related size effects in scratch tests.

Material	width	G_f $(\times 10^3 \ N/m)$	σ_y (MPa)
Cement Paste	2.5	1.00	34.1
	5	1.81	25.8
	10	3.29	14.1
Red Sandstone	2.5	18.08	72.4
	5	10.12	44.6
	10	5.52	22.1
	15	6.15	19.4
Vosges Sandstone	2.5	0.00	33.7
	5	0.00	27.0
	10	0.70	23.0
	15	1.76	18.0

Table 2.3: Patel *et al.*'s method [28] applied to cement paste, red sandstone and Vosges sandstone. Tests carried out by Epslog S. A.; data courtesy of Schlumberger.

Part II

Fracture Approach to Scratch Tests

Chapter 3

Scratch Tests on Paraffin Wax

Our first focus is to understand the underlying mechanism of scratch tests, in the light of the two conflicting point of views: strength-driven versus fracture-driven process. The purpose of this part is the development of a framework for the investigation of the fracture scaling in scratch tests. To this end, Chapter 3 develops a controlled scratch test experiment that makes it possible to identify the validity domain of the strength and fracture interpretations. In Chapter 4 two analytical models based on LEFM derive the fracture toughness from the forces and the geometry of scratch tests. Finally, in Chapter 5, the models proposed in Chapter 4 are confronted with Finite Element simulations to assert their accuracy.

3.1 Experimental Development

In order to explore the fracture scaling in scratch tests, a controlled scratch test was designed using paraffin wax as a model material. In our experiments, a paraffin block of dimensions 3.4×5.7×22 cm is clamped at its lateral sides, set on a linear stage and moved at a constant velocity of 1.3 mm/s against a vertical steel cutter-blade at a depth d (measured from the block's top surface). This blade of rectangular cross section (6.35 mm thick and w wide) is held by a rigid frame that ensures a constant depth and a zero

back-rake angle during the test.

In the following chapter we describe the materials used, the built-in experimental set-up, and analyze the results in the light of the dimensionless relations Eqs. (2.8) and (2.20) which we recall:

$$H_T = \sigma_0 \times \Pi \left(\frac{\sigma_0}{E}, \nu, \mathcal{I} = \frac{d}{(K_c/\sigma_0)^2}, \frac{w}{d}, \theta, \mu \right) \tag{3.1}$$

$$F_T = K_c w \sqrt{d} \times \Pi \left(\frac{\sigma_0}{E}, \nu, \mathcal{I} = \frac{w}{(K_c/\sigma_0)^2}, \theta, \mu \right) \tag{3.2}$$

In our tests, the quantities $\frac{\sigma_0}{E}$ and ν are constants given by the elasto-plastic properties of paraffin wax. Also, the back-rake angle θ is zero in our tests, so that the only two invariants for our tests series are the Irwin number $\mathcal{I} = \frac{d}{(K_c/\sigma_0)^2}$ and the ratio $\frac{w}{d}$. Our strategy is to determine K_c and σ_0 via independent tests and then see which scaling, strength or fracture, prevails in the scratch analysis according to Eqs. (3.1) and (3.2).

3.2   Materials and Methods

3.2.1   Materials

We consider paraffin wax for its thermal stability, nearly-linear elasticity and brittle mechanical properties. The paraffin wax used is EXXO 2730 from the company Polygon Wax [30]. Its density is 0.9kg/m^3, its melting point $52.2°\text{C}$, and the oil content 0.1%. In order to reduce the shrinkage of wax and the cavitation in the molds, an additive, Vybar 260 [1], was added in 1% in mass.

Our specimens were prepared by casting wax in parallelepiped steel molds of dimensions $3.4\times5.7\times34$ cm. A mix of wax and Vybar was melted at $60°\text{C}$ and poured in

---

[1]Vybar is an additive that eliminates bubbles and prevents cavitation during the cooling of wax. Vybar 260 is especially designed for waxes whose melting point is below $54°\text{C}$.
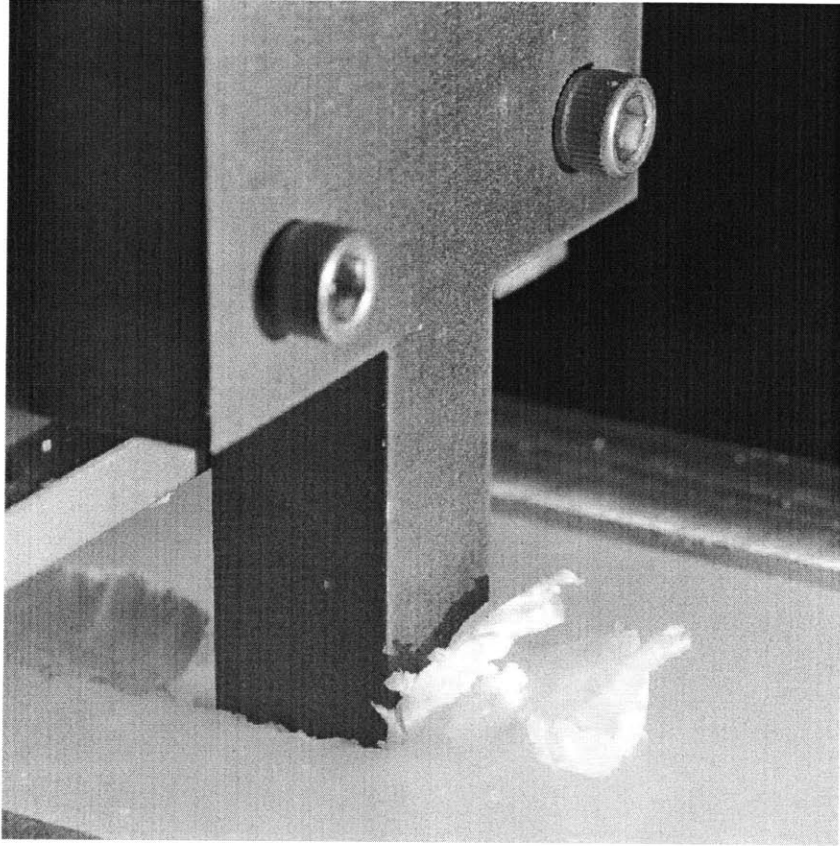
Figure 3-1: scratch test experiment on paraffin wax.

several stages to prevent the formation of holes during the cooling due to the shrinkage of wax. To accelerate the cooling process, the molds were placed into a water bath at room temperature (22°C) in a ventilated location. The molds were then left to harden overnight (8-12 hours) to ensure that the wax reached a complete rigid state.

To ensure that the final specimens of wax had flat faces, the faces of the parallelepiped steel molds were rigorously parallel and the molds set on a levelled glass surface. As a consequence, the roughness of the top faces, measured by a scan of the scratch path prior to the test, varied from 0.03 mm to 0.76 mm with a mean of 0.22 mm and a standard deviation of 0.16 mm.

3.2.2 Material Tests

The compressive tensile and fracture properties of paraffin wax were measured via independent testing methods.

Uniaxial Compression Tests
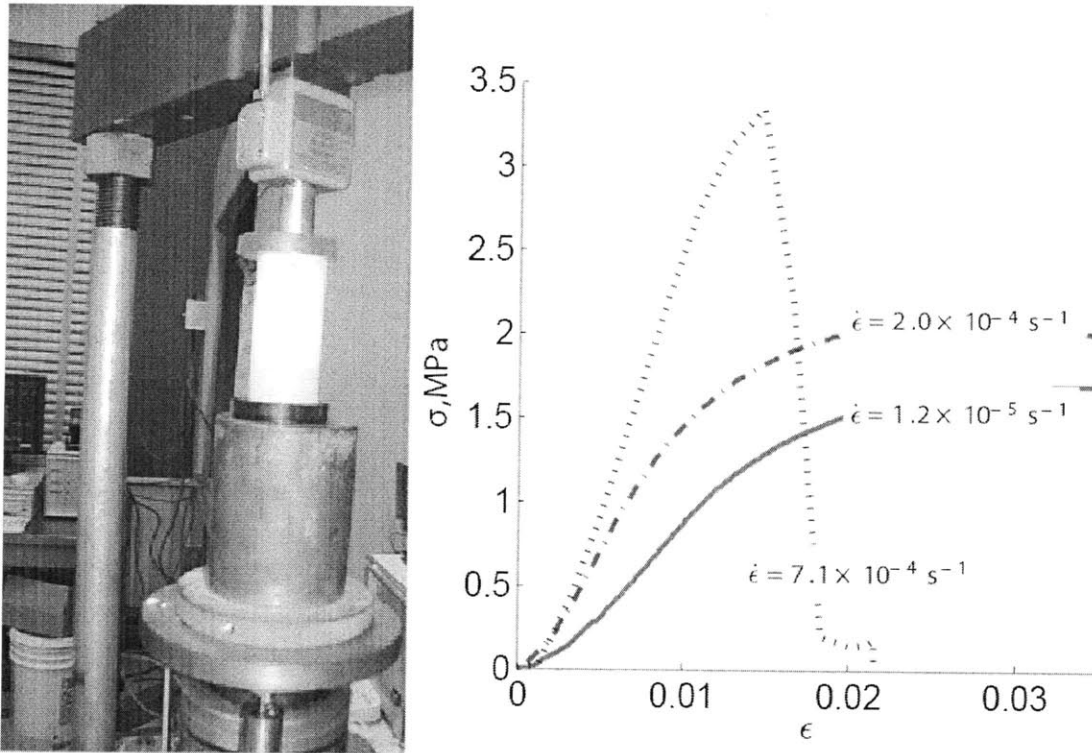
Figure 3-2: Uniaxial compression tests on paraffin wax. Left: Experimental set-up. Right: True strain-true stress curve.

Uniaxial compressive tests were carried out on cylindrical paraffin wax samples of radius $R = 35$ mm and of height $H \geq 70$ mm at room temperature of 22°C. Three strain rates, $\dot{\epsilon} = 2 \times 10^{-5}, 2 \times 10^{-4}, 2 \times 10^{-3}$ s^{-1} were considered and for each strain rate value, three tests were carried out. For the first two strain rates $\dot{\epsilon} = 2 \times 10^{-5}$ s^{-1} and $\dot{\epsilon} = 2 \times 10^{-4}$ s^{-1}, the failure mode was plastic yielding. At these strain rates the values

strain rate (s^{-1})	σ_y (MPa)	UCS (MPa)
2 10^{-3}	N/A	3.53±0.12
2 10^{-4}	1.67±0.14	2.19±0.10
2 $1-^{-5}$	1.29±0.03	1.64 ± 0.01

Table 3.1: Uniaxial compression tests on paraffin wax. Measured compressive yield stress and uniaxial compressive strength

of the compressive yield stress σ_y, determined at a strain of 0.2% offset were 1.2±0.03 MPa for $\dot{\epsilon} = 2 \times 10^{-5}$ s^{-1} and 1.67±0.14 MPa for $\dot{\epsilon} = 2 \times 10^{-4}$ s^{-1}. The values of the uniaxial compressive strength at these strain rates were 1.47±0.01 MPa for $\dot{\epsilon} = 2 \times 10^{-5}$ s^{-1} and 2.19±0.10 MPa for $\dot{\epsilon} = 2 \times 10^{-4}$ s^{-1}. The ductility ratio, defined as the ratio of the failure stress to the yield stress, decreased with the strain rate from 3.5 to 1.25. For $\dot{\epsilon} = 2 \times 10^{-3}$ s^{-1} the failure was brittle and the uniaxial compressive strength was 3.53±0.12 MPa. The values of the uniaxial compressive strength and of the compressive yield strength are reported in Table 3.2.2 while the experimental set-up as well as the true strain-true stress curves are displayed in Fig. 3-2.

Tension Tests on a Plate With a Centered Hole

When carrying out standard uniaxial tension tests, failure would occur by fracture at the supports and not by necking at the center of the specimen, due to the great softness of paraffin wax. For this reason, it was not possible to measure the tensile properties via standard uniaxial tension tests. Therefore we tested finite plates of dimension 10×2×0.5 cm with a hole of radius 0.64 cm in the center. Appendix C develops a lower bound and an upper bound models that show that this method yields the ultimate tensile strength σ_0 with an uncertainty of 15%. Three series of four tests each were carried out at the following strain rates: 1.1×10^{-4} s^{-1}, 1.1×10^{-3} s^{-1} and 1.1×10^{-4} s^{-2}. The failure mode was quasi-brittle and the ultimate tensile strength σ_0 was 2.02±0.18 MPa, 1.72±0.15 MPa and 2.15±0.28 MPa for $\dot{\epsilon} = 1.1 \times 10^{-4}$ s^{-1}, 1.1×10^{-3} s^{-1} and 1.1×10^{-2} s^{-2} respectively. In contrast to compression tests, the tensile strength exhibits no clear strain rate effect, for which reason we use the value at the highest strain rate, $\sigma_0 = 2.15 \pm 0.28$ MPa. The

47

true strain-true stress curves are shown in Fig. 3-3.
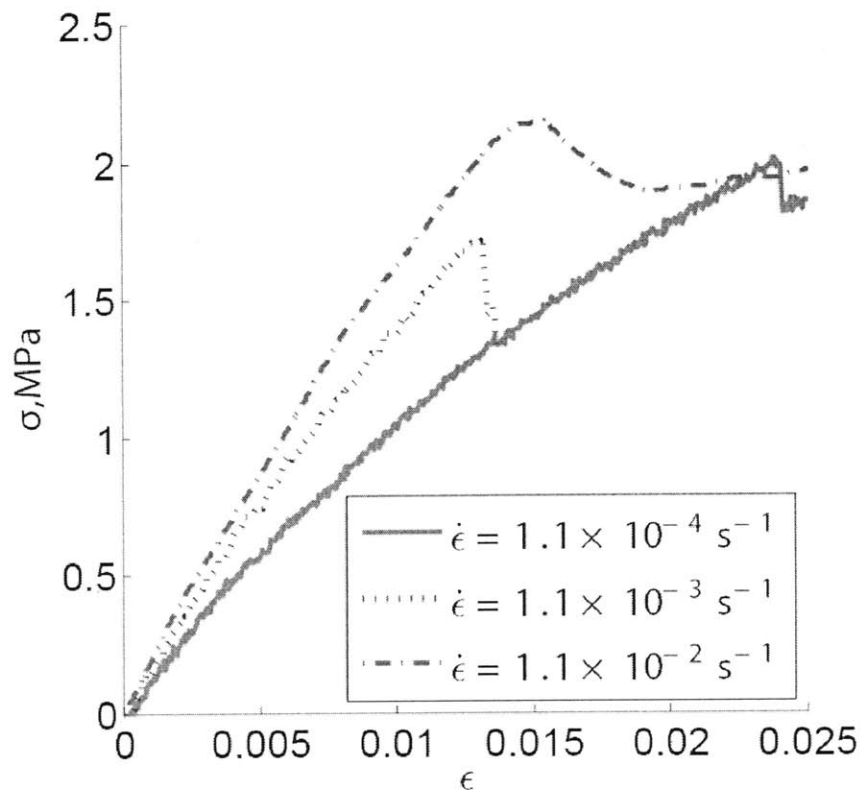
Figure 3-3: Tensile tests on paraffin wax: true-strain true-stress curve.

Three-point bending tests

Three-point bending tests were performed on samples of length $L = 150$ mm and with a rectangular cross section $W \times B$. The samples had a notch of length a in their middle, made with a fine razor. The experimental set-up is displayed in Fig. 3-4. The fracture toughness K_c is related to the maximal prescribed force P_{max} by[5]:

$$K_c = f\left(\frac{a}{W}\right) \frac{PL}{BW^{3/2}} \tag{3.3}$$

48
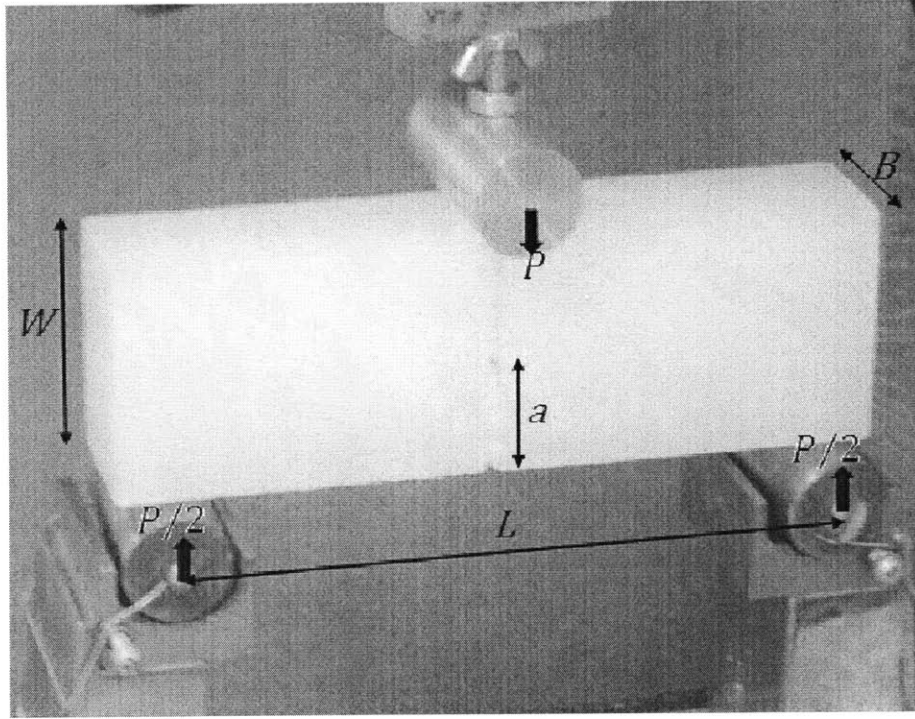
Figure 3-4: Three-point bending tests on notched paraffin wax specimens.

where $f(a/W)$ is a correction factor given by[5]:

$$f\left(\frac{a}{W}\right) = \frac{3(a/W)^{1/2}\left[1.99 - (a/W)(1 - a/W) \times (2.15 - 3.93a/W + 2.7a^2/W^2)\right]}{2(1 + 2a/W)(1 - a/W)^{3/2}} \quad (3.4)$$

A set of three tests were performed with a middle point velocity equal to 4.15×10^{-2} cm/s. The resulting fracture toughness was $K_c = 0.146 \pm 0.01$ MPa$\sqrt{\text{m}}$. We must then check that the ASTM standard [6] for fracture toughness measurement is satisfied, that

W (mm)	B (mm)	L (mm)	a (mm)	$f(a/W)$	P_{max} (N)	K_c (MPa$\sqrt{\text{m}}$)
56	34	150	15	1.40	303	0.141
57	34	150	23	2.04	240	0.128
57	34	150	27	2.45	170.2	0.135

Table 3.2: Three-point bending tests on paraffin wax. Geometric parameters and results. In all tests the velocity of the midpoint deflection was 4.15×10^{-2} cm/s.

49

is:

$$(L, \ B, \ L, \ W, \ a, \ W-a) \geq 16 \times r_c \tag{3.5}$$

where r_c is the fracture process zone which measures the extent of the plastic zone. r_c is given by [34, 26, 34]:

$$r_c = \frac{1}{2\pi} \left(\frac{K_c}{\sigma_0} \right)^2 \tag{3.6}$$

where K_c and σ_y are respectively the fracture toughness and the ultimate tensile strength. From the value of the ultimate tensile strength given above, 2.15±0.28 MPa for $\dot{\epsilon} = 1.1 \times 10^{-2}$ s^{-1}, r_c is estimated to 1.30 mm, and $16 \times r_c = 20.8$ mm, which is smaller the geometric parameters mentioned in Eq. (3.5) and listed in Table 3.2.

In short the measured compressive, tensile and fracture properties are:

$$UCS = 3.53 \pm 0.12 \text{ MPa}, \quad \sigma_0 = 2.15 \pm 0.28 \ MPA \quad K_c = 0.146 \pm 0.01 \text{ MPa}\sqrt{\text{m}} \tag{3.7}$$

3.2.3 Experimental Set-up of Scratch Test

In our tests, a steel blade was used and held by a frame of compliance less than 0.31 mm/kN to maintain both the depth of the scratch d and the back-rake angle $\theta = 0$ constant. The depth sensor had an absolute precision of 10 μm. The horizontal and vertical forces were recorded using respectively a 500lbs Futek S-beam and a 500lbs HoneyWell AL-JP load cell. Finally, a NI USB-6009 National Instrument data acquisition card along with a home-made Labview script were used to acquire the data and to control the Stepper motor that generated the linear motion. A schematic of the experimental set-up is provided in Fig. 3-5.
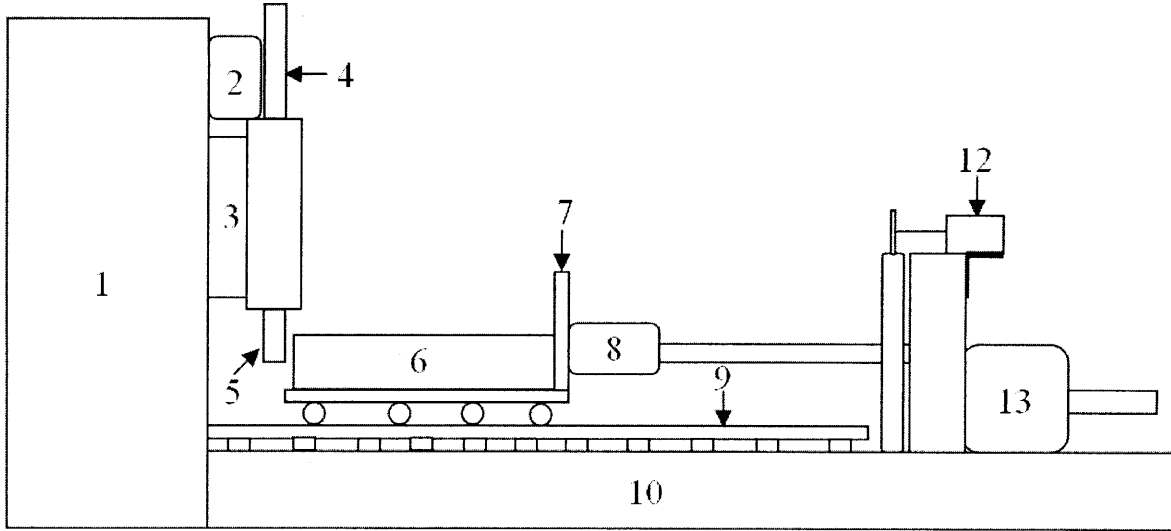
Figure 3-5: Schematic of the built-in scratch tester for paraffin wax. 1 rigid steel frame. 2 500lbs S-beam load cell Futek to acquire the vertical force. 3 linear rails. 4 micrometer to accurately set the depth. 5 steel blade. 6 block of paraffin wax. 7 vice holding the block of paraffin wax. 8 500lbs load cell HoneyWell AL-JP to acquire the horizontal force. 9 linear steel ball bearing rails. 12 stringpot to measure the displacement. 13 Stepper motor to drive the linear stage.

3.3 Results

A total of 55 scratch tests on paraffin wax were performed. The depth d of scratch varied from 2.5 to 12.5 mm while the width w of the blade ranged from 2.5 to 20 mm. The ratio w/d varied from 0.2 to 8, spanning nearly two orders of magnitude. Figs. 3-6 and 3-7 plot respectively the strength and fracture scaling as captured by Eqs. (2.8) and (2.20), respectively.

Fig. 3-6 plots the dependence of the average of F_T as a function of the blade's projected area wd. As expected, for low values of the projected area, F_T scales linearly with wd which is significant of a strength process (the slope being the strength of the material). From a quadratic fit, the scratch hardness, defined by Eq. (2.24), is found to be 4.69±0.23 MPa. The ratio of H_T/UCS of the scratch hardness to the uniaxial
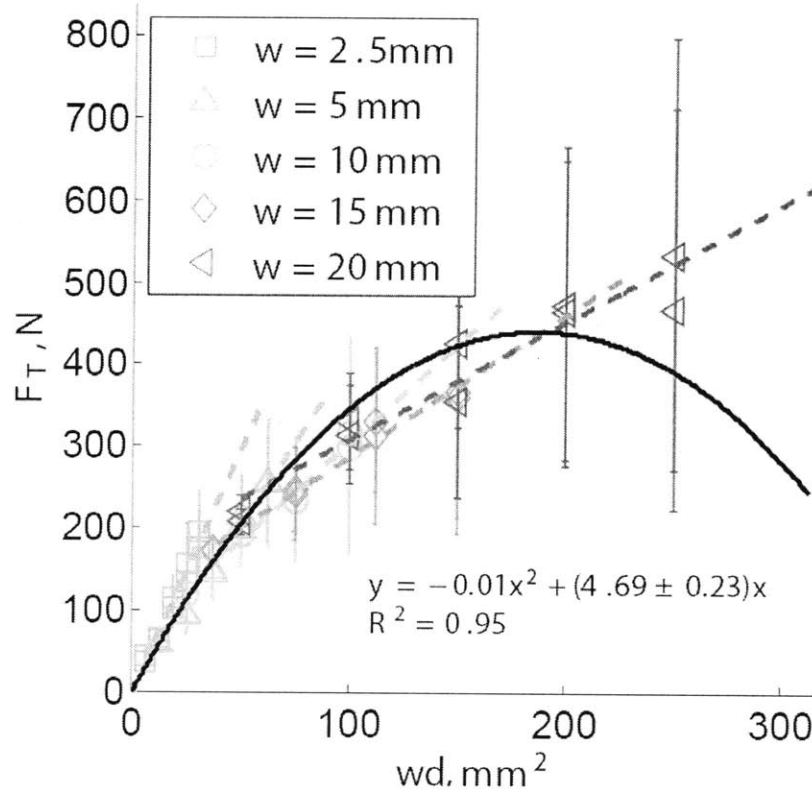
Figure 3-6: Paraffin wax. Strength scaling. The bars represent the standard deviation. The slopes of the dotted lines are the specific energy for each width(cf Eq. (2.13)). The quadratic fit gives H_T with a 95% confidence interval.

compressive strength is equal to 1.32, which is strictly greater than 1 or $2/\sqrt{3}$. Therefore, Table 2.3.2 enables us to infer the presence of internal friction in paraffin wax. Fig. 3-6 also displays the intrinsic specific energy ε for different scratch widths as foreseen by Schei et al.'s approach (see Section 2.3.1). ε is a decreasing function of w whose value range from 5.97 MPa for w=2.5mm to 1.44 MPa for w=20 mm. This is another indication that a fracture process is at play in the scratch response and confirms previous findings for cement paste (cf Fig. 2-4). Another evidence of size effects characteristic of fracture is the non-linearity of the plot (F_T, $wd0$ for high values of wd.

Fig. 3-7 displays the dimensionless force $F_T/(K_c w\sqrt{d})$ versus w/d. The data points were fitted to a polynomial function of degree 3 in $1/x$, $y = a_0 + a_1/x + b_1/x^2 + c_1/x^3$, using

52
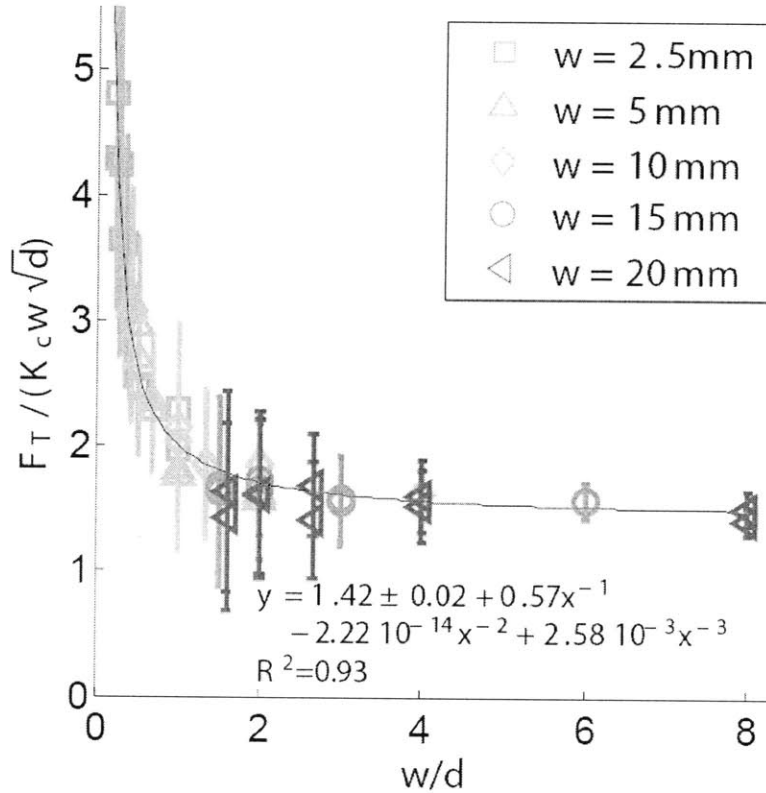
Figure 3-7: Paraffin wax.Fracture scaling. The bars represent the standard deviation. The confidence interval in the value of the asymptote is taken at 95%.

a weighted non-linear least squares regression. This was performed with the curve fitting tool in MATLAB: the initial startpoint (a_0, a_1, a_2, a_3) was random and the coefficients a_0 and a_3 were constrained to be positive to ensure that the fitted function were always positive. There is a convergence toward a constant value of 1.43 ± 0.02. This convergence provides strong evidence that fracture is at play in the scratch response as captured by Eq. (2.20).

3.4 Chapter Summary

The aim of this chapter was to explore the validity domain of the strength and fracture approach via controlled experiments on paraffin wax. The results yield a second confir-

mation that the strength approximation is valid for small values of the projected contact area wd. They also indicate that the fracture scaling found in Chapter 2 is valid for great values of w/d as the dimensionless force $F_T/(K_c w\sqrt{d})$ converges toward a constant. To understand the value of this constant, it is now necessary to develop an analytical model. This is the focus of the next chapter.

Chapter 4

Analytical Modeling of Scratch Tests

This chapter is devoted to the development of analytical models, based on Linear Elastic Fracture mechanics (LEFM), that derive the fracture toughness from the forces, F_V and F_T, generated in the scratch test, and that take into account the geometrical parameters, width w and depth d, of scratch tests. The first model applies a constant uniaxial stress field in scratch tests with a vertical blade, $\theta = 0$. The second model uses an airy stress function approach applied to tests with a non-zero back-rake angle, $\theta > 0$, to improve the representation of stresses in the scratched material. In both models, the energy release rate, which upon crack propagation is equal to the fracture energy, is evaluated using the J-Integral. Finally, the first model is confronted with the scratch test results on paraffin wax.

4.1 Theoretical Background

4.1.1 J-Integral

In linear elastic fracture processes, the spontaneous change in potential energy is due to the creation of additional fracture surface $\Gamma = p\ell$ of crack length ℓ situated on the perimeter p of the scratch device. The energy release rate G is the thermodynamic driving

force of the dissipation due to crack propagation, and is given by the relation:

$$\frac{dD}{dt} = -\frac{dE_{pot}}{dt} = -\frac{\partial E_{pot}}{\partial \Gamma}\dot{\Gamma} = G\,p\dot{\ell} \tag{4.1}$$

where E_{pot} is the potential energy stored in the system. For mode I(plane tensile) and mode II(plane shear) fracture processes, this fracture energy relates to the fracture toughness by [26, 34]:

$$G_f = \kappa\frac{K_c^2}{E} \tag{4.2}$$

where $\kappa = 1$ in plane stress and $\kappa = 1 - \nu^2$ in plane strain. E is the Young's modulus and ν is the poisson's ratio.

For planar crack growth and within the framework of LEFM, the energy release rate can be estimated using a contour integral method, known as the J-Integral (cf [17, 33]). The fundamental idea of this method is to estimate the change in potential energy during a fracture process from the perspective of an observer that is attached to a propagating crack. In a displacement-driven test, the observer thus defined witnesses two sources of potential energy change: one due to the change in free energy density ψ in a material volume V enclosing the crack tip; the other due to the energy release that is convectively transported at a speed $\underline{V} \cdot \underline{n} = -\dot{\ell}n_x$ passed the (fixed) observer:

$$\frac{dE_{pot}}{dt} = \int_V \frac{\partial \psi}{\partial t}\,dV - \int_A \psi\dot{\ell}n_x\,dA \tag{4.3}$$

where A is the closed boundary of V. For a linear elastic material, for which $\psi = \frac{1}{2}\underline{\underline{\sigma}} : \nabla\underline{u}$, the divergence theorem allows a change of the volumetric term into a surface integral:

$$\int_V \frac{\partial \psi}{\partial t}\,dV = \int_V \underline{\underline{\sigma}} : \frac{\partial \nabla\underline{u}}{\partial t}\,dV = \oint_A \underline{T} \cdot \frac{\partial \underline{u}}{\partial x}\dot{\ell}\,dA \tag{4.4}$$

where $\underline{T} = \underline{\underline{\sigma}} \cdot \underline{n}$ are surface tractions, and where we made use of the fact that in a displacement-controlled fracture test, the displacement rate seen by the moving observer

is equal to $\frac{\partial u}{\partial t} = \dot{\ell}\frac{\partial u}{\partial x}$. A comparison of Eqs. (4.3)-(4.4) provides the following expression of the energy release rate:

$$G = \frac{1}{p}\oint_A \left(\psi n_x - \underline{T}\frac{\partial u}{\partial x}\right) da \qquad (4.5)$$

Compared to the classical form of the $J-$Integral [33], in which the fracture perimeter coincides with the fracture width, $dA = pds$, we have chosen to consider a difference between these lengths, in order to employ the technique for different scratch geometries.

4.1.2 Airy stress function

An *Airy stress function* $\varphi(x,z)$ is a function introduced to satisfy the equations of equilibrium of plane problems:

$$\sigma_{xx} = \frac{\partial^2 \varphi}{\partial z^2}; \quad \sigma_{xz} = -\frac{\partial^2 \varphi}{\partial x \partial z}; \quad \sigma_{zz} = \frac{\partial^2 \varphi}{\partial x^2}; \qquad (4.6)$$

With this definition of φ, and provided that the body forces are negligible, the equilibrium equations are automatically verified:

$$\frac{\partial \sigma_{xx}}{\partial x} + \frac{\partial \sigma_{xz}}{\partial z} = 0 \qquad (4.7)$$

$$\frac{\partial \sigma_{xz}}{\partial x} + \frac{\partial \sigma_{zz}}{\partial z} = 0 \qquad (4.8)$$

Moreover, if the material's behavior is linear elastic isotropic, the compatibility Equation reads:

$$\frac{\partial}{\partial x^2}\left(\sigma_{xx} + \sigma_{zz}\right) + \frac{\partial}{\partial z^2}\left(\sigma_{xx} + \sigma_{zz}\right) = 0 \qquad (4.9)$$

therefore φ is biharmonic. That is:

$$\Delta\Delta\varphi = 0 \qquad (4.10)$$

where Δ is the laplacian operator defined in 2-D by:

$$\Delta\varphi(x,z) = \frac{\partial^2\varphi}{\partial x^2} + \frac{\partial^2\varphi}{\partial z^2} \tag{4.11}$$

Eq. (4.10) is exact in plane strain conditions and yields a good approximation for thin plates in plane stress conditions. Therefore, solving for a statically compatible stress field boils down to finding an Airy stress function $\varphi(x,z)$ verifying Eq. (4.10) in a way that the stress boundary conditions are satisfied.

Moreover, if body forces are negligible, and if the behavior is linear elastic isotropic described by E and ν, then the displacements are related to the Airy stress function by:

$$u_x(x,z) = \frac{1}{E}\left(-(1+\nu)\frac{\partial\phi}{\partial x} + \kappa\frac{\partial V}{\partial z}\right) + U_x \tag{4.12}$$

$$u_z(x,z) = \frac{1}{E}\left(-(1+\nu)\frac{\partial\phi}{\partial z} + \kappa\frac{\partial V}{\partial x}\right) + U_z \tag{4.13}$$

where (U_x, U_z) is a plane rigid displacement, that does not provoke strains.

4.2   Fracture Toughness Derivation

In the following section, we will use the tools presented above to estimate the energy release rate G, considering separately the case $\theta = 0$ and $\theta > 0$.

4.2.1   Scratch Tests With a Vertical Blade ($\theta = 0$)

Considering the simplified geometry illustrated in Fig. 4-1, we hypothesize the existence of crack planes surrounding the blade. For the scratch problem at hand, we choose a closed volume that includes the blade-material interface, the stress-free surface at the top ($\underline{n} \cdot \underline{e}_x = 0$; $\underline{T} = \underline{0}$), the (stress free) fracture surfaces in prolongation of the scratch probe surface ($\underline{n} \cdot \underline{e}_x = 0$; $\underline{T} = \underline{0}$), and closing material surfaces far removed from the surfaces ($\psi = 0$; $\frac{\partial \underline{u}}{\partial x} = 0$); so that the only contribution to the surface integral comes

58
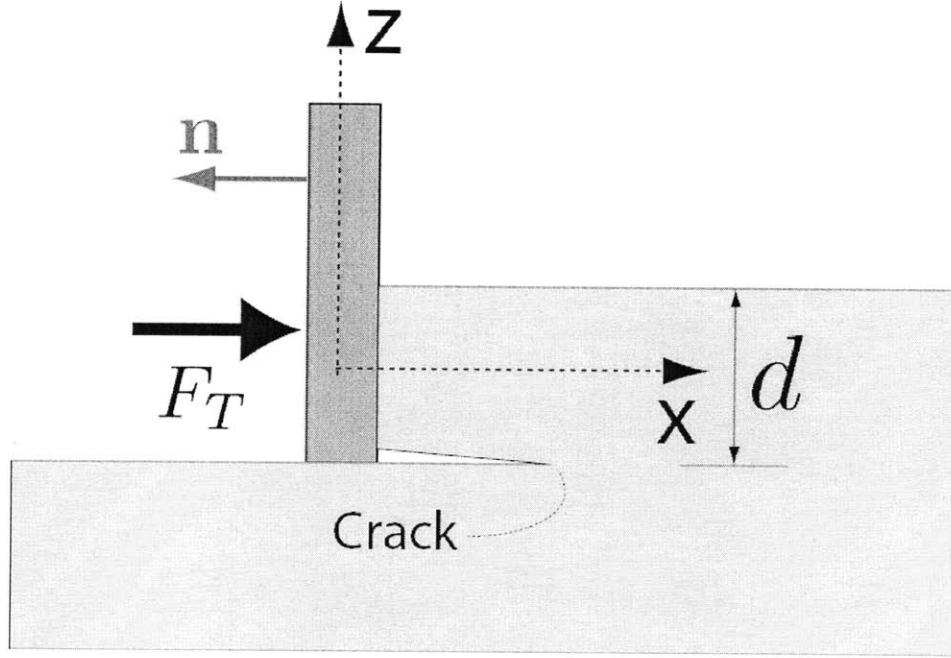
Figure 4-1: Simplified geometry of a scratch test with a vertical blade (θ=0). Courtesy of Pedro Reis.

from the blade-material interface S:

$$G = \frac{1}{p} \int_{(S)} \left(\psi n_x - \underline{T} \cdot \frac{\partial \underline{u}}{\partial x} \right) dS \tag{4.14}$$

Physically speaking, the energy release so defined can be associated with the energy stored, prior to chipping, into a material domain in front of the scratch blade.

Consider then a rectangular blade ($\underline{n} = -\underline{e}_x$) of width w that generates a crack surface $\Gamma = (w + 2d)\,\ell$. Noting that $\underline{T} = \underline{\underline{\sigma}} \cdot \underline{n} = -\sigma_{xx}\underline{e}_x$, $\sigma_{xx} = -F_T/(wd)$; $\psi = \frac{1}{2}\sigma_{xx}\varepsilon_{xx} = \kappa\sigma_{xx}^2/(2E)$; $u_{x,x} = \kappa\sigma_{xx}/E$ (where $\kappa = 1$ in plane stress and $\kappa = 1 - \nu^2$ in plane strain applications) and $dS = wdz$, we obtain:

$$G = \frac{\int_{(d)} (\sigma_{xx} u_{x,x} - \psi)\, dz}{1 + 2\frac{w}{d}} = \frac{\kappa F_T^2}{2Ew^2 d \left(1 + 2\frac{w}{d}\right)} \tag{4.15}$$

59

As the scratch probe is pushed along the scratch path, fracture surfaces are generated along the probes bottom and lateral surfaces, releasing in the course the fracture energy, i.e. $G \equiv G_f$. Eq. (4.2) relates the fracture energy G_f, to the fracture toughness of the material K_c. Expressed in terms of the dimensionless force $F_T/(K_c w \sqrt{d})$ we thus find:

$$\frac{F_T}{K_c w \sqrt{d}} \leq \sqrt{2\left(1 + 2\frac{d}{w}\right)} \tag{4.16}$$

In particular, if $w/d \gg 1$, the dimensionless force $F_T/(K_c w \sqrt{d})$ converges toward $\sqrt{2} = 1.41$. This value is within the range of the asymptotic value of $F_T/(K_c w \sqrt{d})$, 1.43±0.02, found for paraffin wax in Chapter 3.
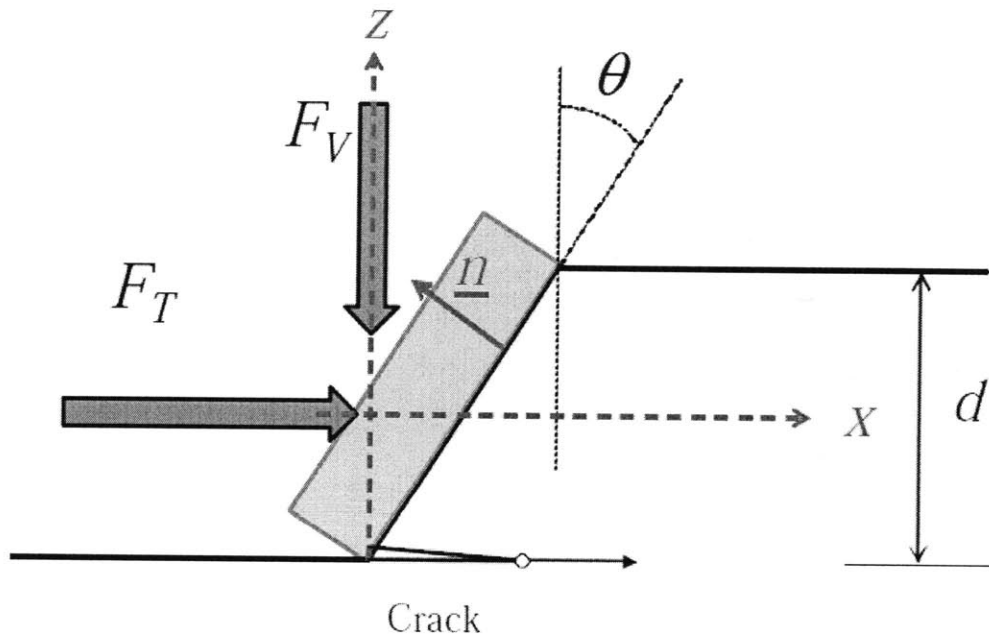
Figure 4-2: Simplified geometry of a scratch test with an inclined blade ($\theta > 0$).

4.2.2 Scratch Tests With an Inclined Angle $\theta > 0$

The next case we consider is a scratch test with an inclined blade shown in Fig. 4-2. We first solve for the stress and displacement field, using the Airy stress function method. Then we apply the J-Integral to evaluate the fracture energy, and thus the fracture toughness.

Elastic Stress and Displacement Fields

The boundary value problem we aim to solve is to find a stress field $\underline{\underline{\sigma}}(x,z)$ that is symmetric and that satisfies:

- The equilibrium equations, that is, in the absence of body forces, Eqs. (4.7) and (4.8)

- The stress boundary conditions, which means here the stress-free boundary conditions on the top face and on the crack face, as well as the vertical and tangential force boundary conditions at the blade-material interface:

$$\sigma_{zz}\left(x, z = \pm d/2\right) = \sigma_{xz}\left(x, z = \pm d/2\right) = 0 \tag{4.17}$$

$$\int_{(S)} \underline{\underline{\sigma}}.\underline{n} \, dS = F_T \, \underline{e}_x - F_V \, \underline{e}_z \tag{4.18}$$

where $\underline{n} = \cos\theta \, \underline{e}_x + \sin\theta \, \underline{e}_z$ is the outward unit normal to the interface.

- The compatibility equation, Eq. (4.9)

In order to satisfy Eq. (4.17), we consider the subset of stress fields given by the following Airy stress function:

$$\varphi(x,z) = -bx\left(z^3 - 3z\frac{d^2}{4}\right) + cz^2 \tag{4.19}$$

61

Where (b, c) are constants to be determined from the boundary conditions. Using Eq. (4.6), the stresses are then given by:

$$\sigma_{xx} = 2c - 6bxz \tag{4.20}$$

$$\sigma_{xz} = 3bd^2 \left(\frac{z^2}{d^2} - \frac{1}{4} \right) \tag{4.21}$$

$$\sigma_{zz} = 0 \tag{4.22}$$

The expression of the constants b and c is found by solving for the boundary conditions at the blade-material interface (i.e. Eq. (4.18)):

$$b = -2 \frac{F_V}{wd^3} \tag{4.23}$$

$$c = -\frac{F_T}{2wd} \tag{4.24}$$

Finally, the displacements given by Eq. (4.13) read for the chosen function Eq.(4.19):

$$u_x = \frac{1}{E} \left[b \left((1 + \nu + \kappa)z^3 - 3\kappa zx^2 - \frac{3}{4}(1+\nu)zd^2 \right) + 2\kappa cx \right] + U_x \tag{4.25}$$

$$u_z = \frac{1}{E} \left[b \left(\kappa x^3 + 3(1 + \nu - \kappa)xz^2 - \frac{3}{4}(1+\nu)xd^2 \right) - 2(1 + \nu - \kappa)cz \right] + U_z \tag{4.26}$$

Now that the stress, strain and displacement fields are known, we can evaluate the J-Integral to compute the energy release rate G.

Energy Release Rate and Fracture Toughness

For the evaluation of the J-Integral, we choose a closed contour which includes the blade-material interface (outward unit normal $\underline{n} = -\cos\theta\underline{e}_x + \sin\theta\underline{e}_z$), the crack tip, the stress-free surfaces at $x \geq d/2 \tan\theta$ and $z = \pm d/2$, and closing material surfaces far removed from the crack-tip, so that the only contribution to the J-Integral comes from

62

the blade-material interface S. Recalling Eq. (4.5), we have:

$$G = \frac{1}{p} \oint_{(S)} \left(\psi n_x - \underline{T} \cdot \frac{\partial \underline{u}}{\partial x} \right) dS = \frac{w}{p} \int_{(S)} \left(\psi n_x - \underline{T}(\underline{n}) \cdot \frac{\partial \underline{u}}{\partial x} \right) dS \qquad (4.27)$$

where ψ is the free energy volume density, $\underline{T}(\underline{n}) = \underline{\underline{\sigma}} \cdot \underline{n}$ is the stress vector at the blade-material interface, $\underline{\xi}$ is the displacement field, and $p = w + 2d$ is the perimeter of the projected contact area of the blade with the material. Knowing the stress and displacement fields, we can now compute the two components of the energy release rate; that is the free energy contribution and the displacement-gradient contribution.

The contribution from the free energy at the surface is calculated on account of the stress solution Eq. (4.22) from:

$$\psi = \frac{1}{2} \underline{\underline{\sigma}} : \underline{\underline{\epsilon}} = \kappa \frac{\sigma_{xx}^2}{2E} + (1+\nu) \frac{\sigma_{xz}^2}{E} \qquad (4.28)$$

(Note that $\sigma_{yy} \epsilon_{yy} = 0$ in both plane stress ($\sigma_{yy} = 0$) and plane strain ($\epsilon_{yy} = 0$) applications.). This yields:

$$
\begin{aligned}
G_1 &= \frac{w}{w + 2d} \int_{(S)} \psi n_x dS \\
&= -\frac{w}{w + 2d} \int_{z=-d/2}^{z=-d/2} \psi \left(\left(z + \frac{d}{2} \tan \theta \right), z \right) dz \\
&= \frac{w}{w + 2d} \frac{1}{E} \left[-2c^2 \kappa d + c\kappa b d^3 \tan \theta - \frac{3}{5} b^2 d^5 \left(\frac{1+\nu}{2} + \frac{\kappa}{\cos^2 \theta} - \kappa \right) \right] \qquad (4.29)
\end{aligned}
$$

On account of Eq. (4.22) and of Eq. (4.26), the stress vector - displacement gradient scalar product acting on the inclined surface contributes to the energy release rate as

63

follows:

$$G_2 = \frac{w}{w + 2d} \int_{(S)} -\underline{T}(\underline{n}) \frac{\partial \underline{\xi}}{\partial x} dS$$

$$= -\frac{w}{w + 2d} \frac{1}{\cos \theta} \int_{z=-d/2}^{z=-d/2} \underline{T}(\underline{n}) \cdot \frac{\underline{\xi}}{\partial x} |_{x=(z+d/2 \tan \theta)} \, dz$$

$$= \frac{w}{w + 2d} \frac{1}{E} \left[4c^2 \kappa d - c\kappa b d^3 \tan \theta - \frac{3}{5} b^2 d^5 \left(-\frac{1 + \nu}{2} - \frac{\kappa}{\cos^2 \theta} + \frac{7}{8} \kappa \right) \right] \qquad (4.30)$$

The J-Integral thus provides the following expression of the energy release rate:

$$G = G_1 + G_2 = \frac{w}{w + 2d} \frac{\kappa}{E} \left(2c^2 d + \frac{3}{40} b^2 d^5 \right) \qquad (4.31)$$

Finally, by replacing b and c by their respective values (Eq. (4.24)), we obtain:

$$G = G_1 + G_2 = \frac{w}{w + 2d} \frac{\kappa}{E} \left(\frac{1}{2} F_T^2 + \frac{3}{10} F_V^2 \right) \qquad (4.32)$$

Upon fracture propagation, the energy release rate equals the fracture energy, which in turn, within the limit of LEFM, can be linked to the fracture toughness by Eq. (4.2). This means that the scratch test provides a means to determine the fracture toughness from:

$$\frac{\sqrt{F_T^2 + \frac{3}{5} F_V^2}}{w \sqrt{d}} \leq K_c \sqrt{2 \left(1 + 2\frac{w}{d} \right)} \qquad (4.33)$$

Eq. (4.33) is similar to Eq. (4.16) with the difference that F_T is replaced by an equivalent force $F_{eq} = \sqrt{F_T^2 + \frac{3}{5} F_V^2}$. In fact, for $\theta = 0$ the vertical force is fully transmitted into the material via the horizontal blade-material interface, and therefore does not need to be accounted for; whereas for $\theta > 0$, the vertical force, as well as the horizontal force, can only be transmitted through the inclined interface. This is consistent with Amontons-Coulomb's law of friction (Eq. (2.1)) for which the friction coefficient on the

64

inclined interface is given by:

$$\mu = -\theta + \tan^{-1}\left(\frac{F_V}{F_T}\right) \tag{4.34}$$

The found scaling relation is thus in agreement with the dimensional analysis, that is, Eq. (2.20).

4.3   Chapter Summary

In this chapter, two models were developed that link the fracture toughness to the forces and geometry of the scratch tests. For large values of w/d, K_c is given by $\frac{F_{eq}}{w\sqrt{d}}$ where $F_{eq} = F_T$ if the blade is vertical ($\theta = 0$) and $F_{eq} = \sqrt{F_T^2 + \frac{3}{5}F_V^2}$ if the blade is inclined ($\theta > 0$). This scaling captures the classical size effect inherent to linear elastic fracture processes as described by Eq. (2.5). It is also in agreement with the scaling predicted by dimensional analysis (Eq. (2.20)). The two models hold the promise to become tools for fracture toughness determination. However, before we can use them for inverse applications, we need to assess their accuracy. This is the focus of the next chapter.

Chapter 5

Model Validation by Finite Element

This chapter focusses on the validation of the analytical models derived in Chapter 4. This is achieved by Finite Element (FE) simulations using Abaqus Version 6.9-1. The model and methods used to simulate a scratch test and compute the energy release rate are described and then applied to understand the dominant mode of fracture propagation. Finally, the accuracy of the analytical solutions Eqs. (4.16) and (4.33), derived in Chapter 4, is evaluated.

5.1 Finite Element Analysis of Scratch Test

For the FE simulation, the scratch test is modeled by the 2-D structure shown in Fig. 5-1. The horizontal displacement is constrained on the RIGHT side of the structure and both the horizontal and vertical displacements are constrained on the BOTTOM side of the structure. The main geometric parameters of the problem are the depth of the scratch d, the inclination angle of the interface θ, or back-rake angle, the length of the crack ℓ, and the out-of-plane width of the structure, w. Three further length scales may affect the numerical analysis. There are: L_1, L_2 and H, representing the distance of the crack from the borders. We choose them at least an order of magnitude greater than ℓ and d, first in order to approximate the assumption of a crack in an infinite medium, secondly
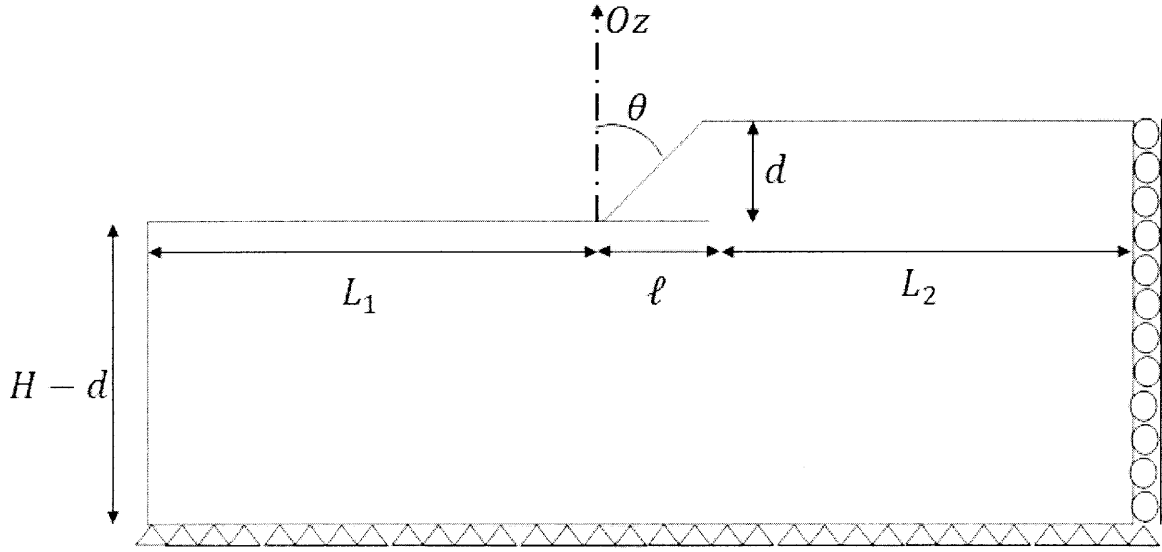
Figure 5-1: Finite Element modeling of scratch tests. The structure above was modeled in ABAQUS 6.9-1 with the following boundary conditions: RIGHT $u_x = 0$, BOTTOM $u_x = u_z = 0$.

to minimize the effect of the displacement constraints at the boundaries. In fact, by Saint-Venant's principle the influence of the displacement constraints at the boundaries should become negligible far from those boundaries.

Two kinds of loading conditions are considered. Using force boundary conditions, a uniform traction is prescribed on the interface in both directions, $\underline{e}_x$ and $\underline{e}_z$. Using displacement boundary conditions, a rigid blade is in contact with the interface, and a horizontal displacement u is applied to the blade, while its vertical displacement is constrained. Moreover, in the simulation, we assume frictional interface condition with different values for the friction coefficient, $\mu = 0, 0.1, 0.2$. The back-rake angle θ considered in the simulation, varies between $0°$ and $60°$. Because of non-linearities due to the contact condition between the faces of the crack and between the blade and the material, the simulations did not converge for $\theta > 45°$, for displacement boundary conditions. In all cases, the loading resulted in a resultant force $F_T \underline{e}_x - F_V \underline{e}_z$ acting on the interface.

67

Assuming the material to be linear elastic isotropic, the stress intensity factors, K_I and K_{II}, in mode I (plane tensile) and II (plane shear), respectively, depend on the loading and on the geometrical parameters of the structure. Dimensional analysis yields:

$$\frac{K_I}{\frac{F_T}{w\sqrt{d}}} = \mathcal{F}_I \left(\frac{F_T}{F_V}, \theta, \frac{l}{d}, \frac{L_1}{d}, \frac{L_2}{d}, \frac{H}{d} \right) \tag{5.1}$$

$$\frac{K_{II}}{\frac{F_T}{w\sqrt{d}}} = \mathcal{F}_{II} \left(\frac{F_T}{F_V}, \theta, \frac{l}{d}, \frac{L_1}{d}, \frac{L_2}{d}, \frac{H}{d} \right) \tag{5.2}$$

The goals of the following investigation are multiple:

- To test the validity of the scaling above, Eqs. (5.1) and (5.2), for a wide range of inclination angle $0 \le \theta \le 60°$.

- To understand the fracture mechanism at work during the scratch test and assess the relative importance of plane tensile fracturing (mode I) compared to plane shear fracturing (mode II).

To this purpose, we will describe the Finite Element model first and then present and discuss the results obtained.

5.2   Finite Element Model

5.2.1   Mesh and Crack Modeling

The structure is meshed with 8-node biquadratic plane strain quadrilateral elements, (CPE8R), available in Abaqus 6.9-1. The mesh has 24,060 elements and 72,843 nodes. The mesh is refined around the crack and a circle of special elements with midside nodes to the quarter point are used around the crack tip. This is done in order to capture the singularity of stresses generated by the presence of the crack.
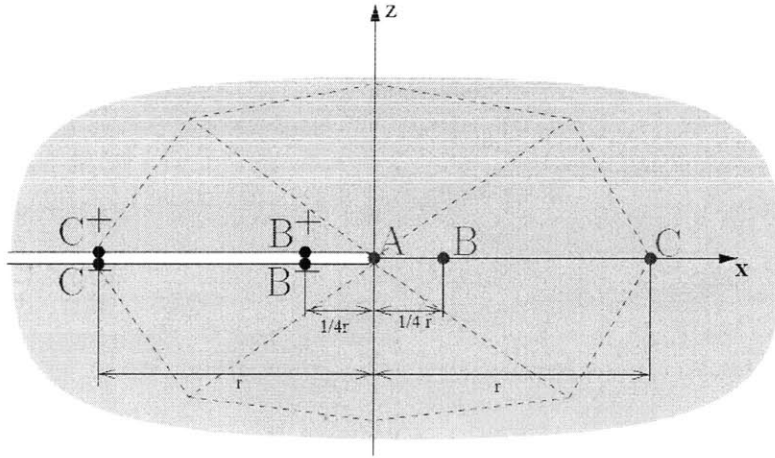
Figure 5-2: Fracture toughness calculation. Source [21]

The method presented here, to compute the stress intensity factors, is taken from Bonnet [21] in his lecture notes of MEC568, at the Ecole Polytechnique. The stress intensity factors are estimated from the jump in displacement between the upper and lower faces of the crack. Consider a quadratic triangular element near the crack tip as shown in Fig. 5-2. If the subscript + designates the nodes on the upper face of the crack and − designates the nodes on the lower face, the displacement jump at the quarter-nodes B_- and B_+ and end-nodes C_- and C_+ is defined by:

$$\Delta \underline{u}_B = \underline{u}_{B_+} - \underline{u}_{B_-};$$ (5.3)

$$\Delta \underline{u}_C = \underline{u}_{C_+} - \underline{u}_{C_-};$$ (5.4)

The stress intensity factors in mode I and I are then given by:

$$K_I = \frac{E\sqrt{2\pi}}{8\kappa} \frac{1}{\sqrt{\frac{1}{4}r}} \left[2\Delta \underline{u}_B - \frac{1}{2}\Delta \underline{u}_C \right] \cdot \underline{n}$$ (5.5)

$$K_{II} = \frac{E\sqrt{2\pi}}{8\kappa} \frac{1}{\sqrt{\frac{1}{4}r}} \left[2\Delta \underline{u}_B - \frac{1}{2}\Delta \underline{u}_C \right] \cdot \underline{t}$$ (5.6)

69

where $\underline{n} = \underline{e}_z$ is the normal to the crack surface, and $\underline{t} = \underline{e}_x$ is the direction of crack propagation. Finally, restricting ourselves to plane strain conditions ($\kappa = 1 - \nu^2$), the fracture energy release rate G relates to the fracture toughness in mode I and II by [26, 34]:

$$G = \frac{\kappa}{E} \left(K_I^2 + K_{II}^2 \right) \tag{5.7}$$

where the elastic constants used are: $E = 1$, $\nu = 0.3$.

5.2.2 Force Boundary Conditions

For modeling force-driven scratch tests, we apply at the inclined interface a horizontal and a vertical force, denoted by F_T and F_V, respectively. One way of doing this in Abaqus is to apply two general tractions $\underline{t}_x = t_x \underline{e}_x$ and $\underline{t}_z = -t_z \underline{e}_z$ at the interface. If we impose the tractions in the undeformed configuration and prevent them from rotating with the surface, then the horizontal and vertical resultants at the interface are constant, and given by:

$$\frac{F_T}{w} = \int_{Interface} \underline{t}_x \cdot \underline{e}_x \, da = \frac{d}{\cos\theta} t_x \tag{5.8}$$

$$\frac{F_V}{w} = \int_{Interface} \underline{t}_z \cdot \underline{e}_z \, da = -\frac{d}{\cos\theta} t_z \tag{5.9}$$

where w is the out-of-plane width of the structure, set equal to 1. We introduce a friction coefficient μ to account for an Amontons-Coulomb type friction at the interface. If $\beta = \tan^{-1}(\mu)$ is the friction angle, t_x and t_z are then related by:

$$t_z = \tan(\theta + \beta) t_x \tag{5.10}$$

In our simulations t_x is linearly increased from 0 to 0.01MPa.
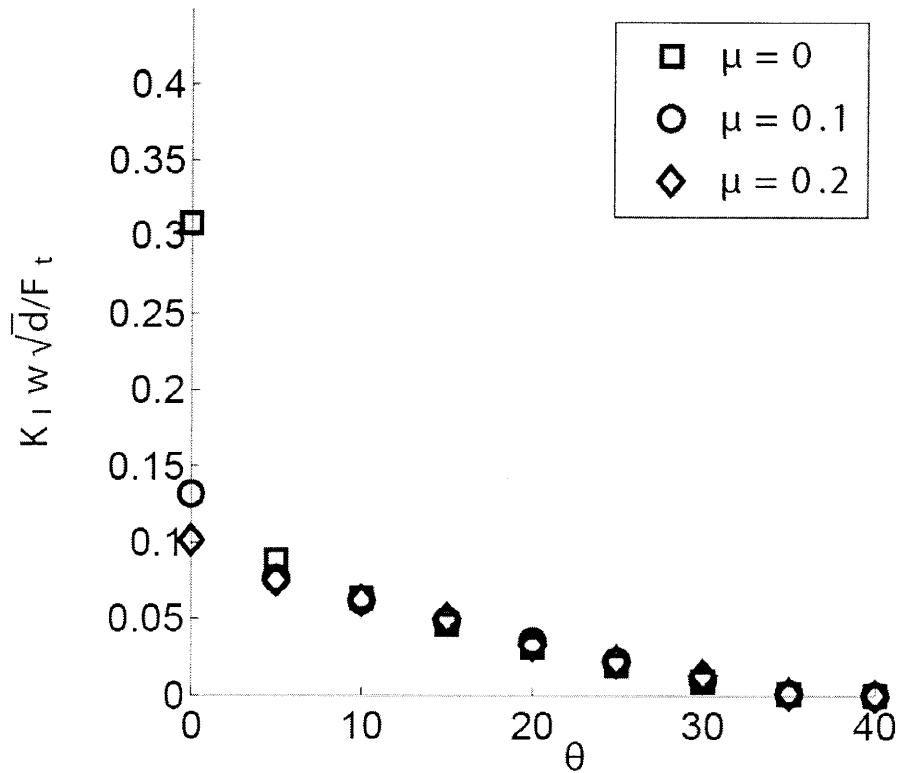
Figure 5-3: Displacement boundary conditions. Scaling of K_I.

5.2.3 Displacement Boundary Conditions

For the modeling of displacement-driven scratch tests, a rigid blade is in contact with the inclined interface of the material. A horizontal displacement u is prescribed to the blade whereas its vertical displacement is constrained, as well as any rotation around the Oz axis. The friction coefficient between the blade and the material varies, $\mu = 0$, 0.1, 0.2, and a hard contact is used to prevent any interpenetration between the blade and the material.
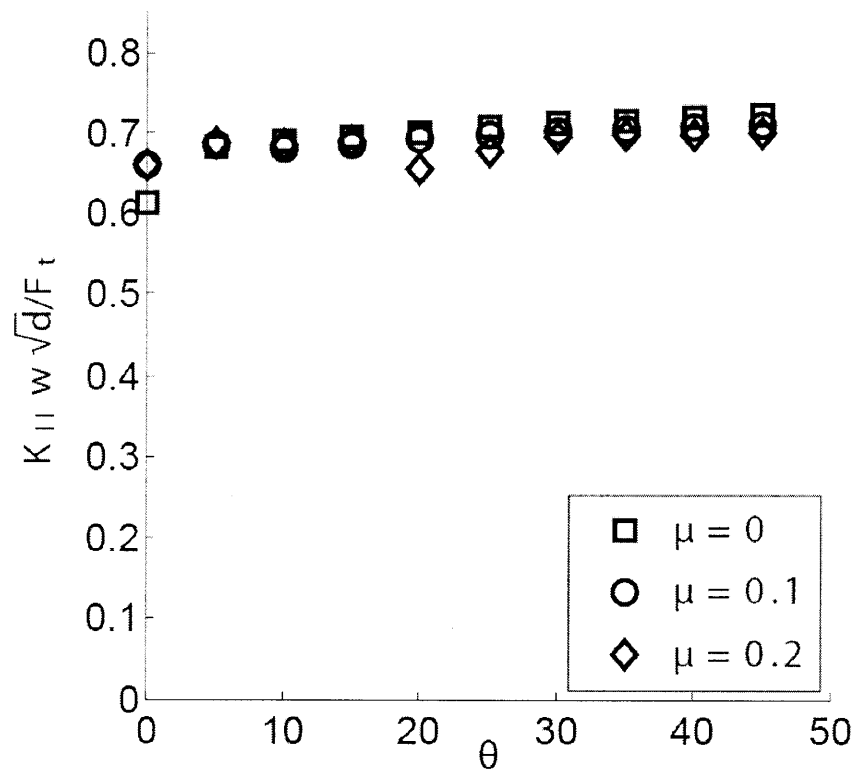
Figure 5-4: Displacement boundary conditions. Scaling of K_{II}.
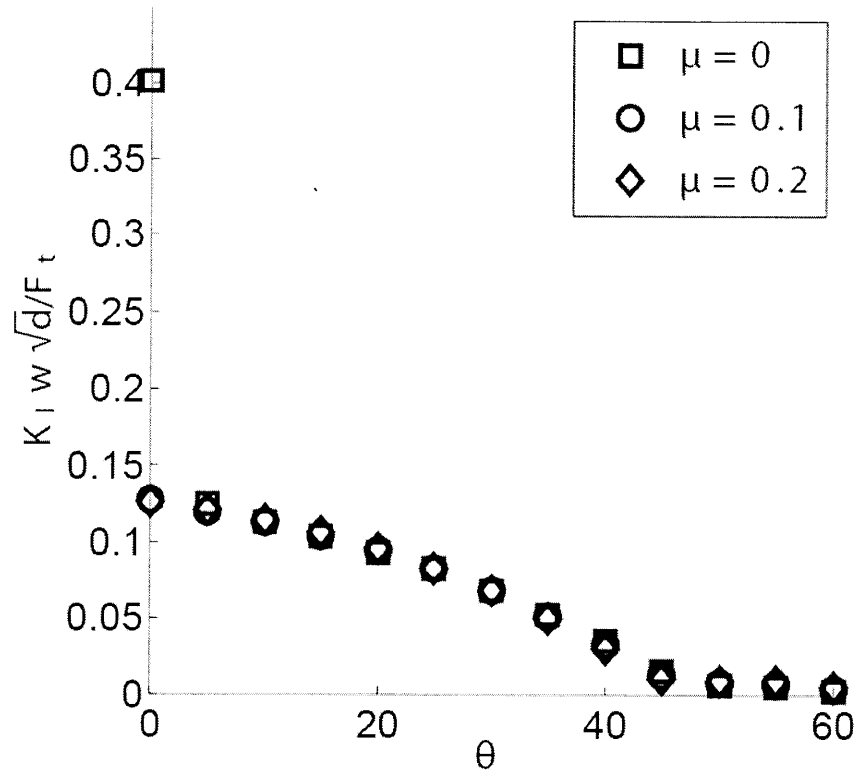
Figure 5-5: Force boundary conditions. Scaling of K_I.
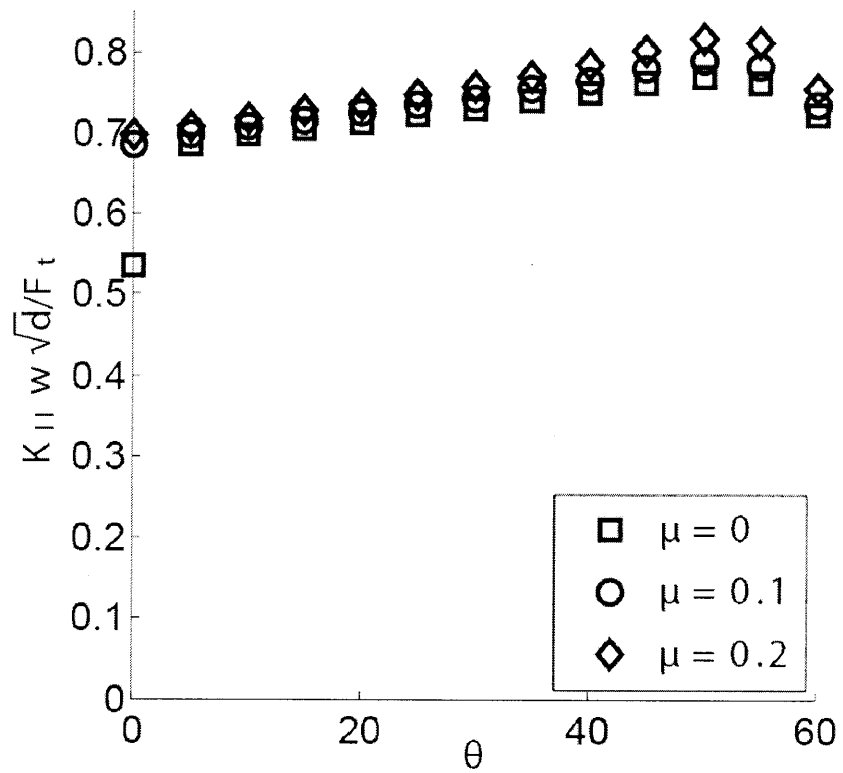
Figure 5-6: Force boundary conditions. Scaling of K_{II}.
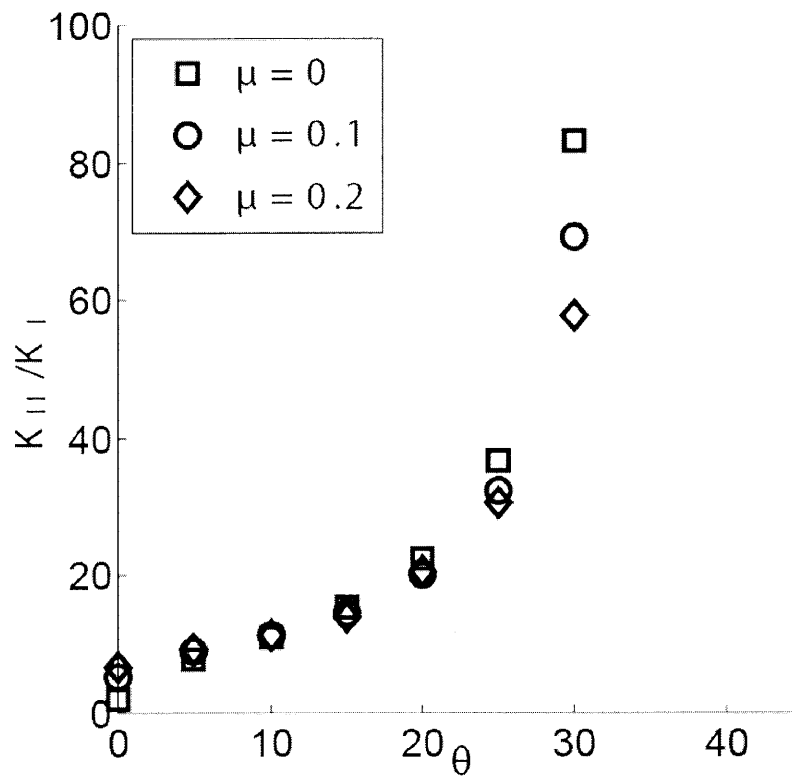
Figure 5-7: K_{II}/K_I versus θ. Displacement boundary conditions.
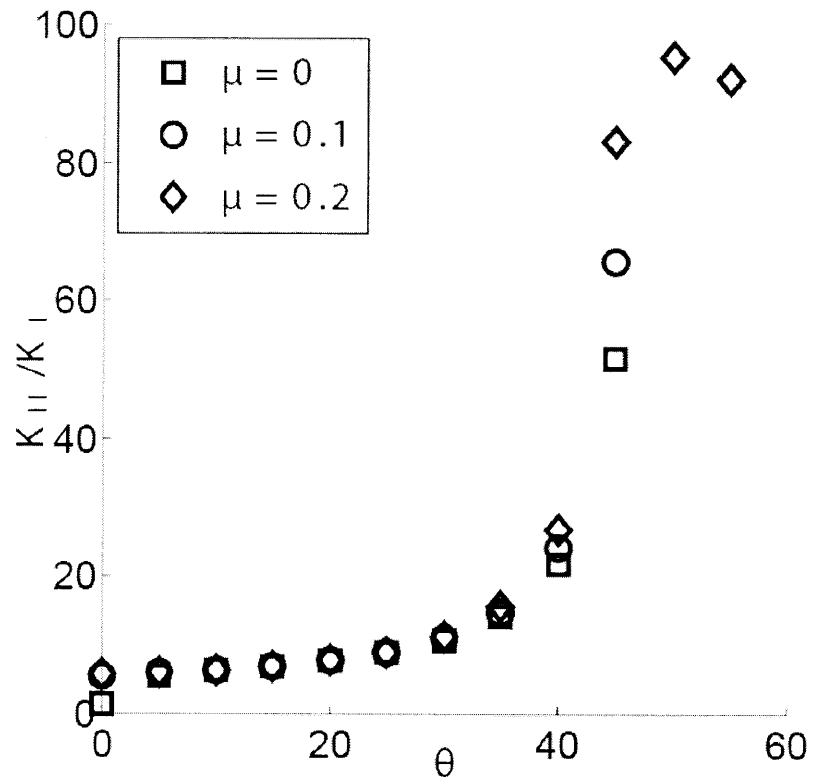
Figure 5-8: K_{II}/K_I . Force boundary conditions.

5.3 Results

In this section we will first discuss the dominant mode of crack propagation, mode I versus mode II, and then confront the scaling with the results of Chapter 4.

5.3.1 Fracture Propagation Modes

Figs. 5-3 to5-6 display the normalized stress intensity factors (Eqs. 5.1 and (5.2)) in mode I, $K_I w \sqrt{d}/F_T$, and mode II, $K_{II} w \sqrt{d}/F_T$, versus θ for both force and displacement boundary conditions. For both loading conditions the stress intensity factor in mode I decreases with θ and even becomes negative, for values of $\theta > 34°$ in displacement-controlled tests (Fig. 3-3) and $\theta > 45°$ in force-controlled tests (Fig. 3-5). In fact, as θ increases, the crack opening decreases and, upon crack closure, compressive stresses develop on the crack faces. On the other hand, the stress intensity factor in mode II increases with θ for $0 \leq \theta \leq 45°$. Moreover, for both modes, the ratio K_{II}/K_I (Figs. (5-7) and (5-8))is always than two and it rises sharply with θ. Therefore, mode II, plane shear fracture mode, is identified as the dominant mode of fracture propagation.

5.3.2 Fracture Toughness Scaling

Figs. 5-9 and 5-10 display the variation of the dimensionless parameter $F_{eq}/(Kw\sqrt{d})$ according to the analytical solution Eq. (4.33). Here we define $K = \sqrt{K_I^2 + K_I^2}$, and $F_{eq} = \sqrt{F_T^2 + \frac{3}{5}F_V^2}$ for $\theta > 0$, and $F_{eq} = \sqrt{F_T^2}$ for $\theta = 0$. The analytical model predicts for large values of the ratio w/d that $\frac{F_{eq}}{Kw\sqrt{d}} = \sqrt{2}$. Simulations show that, for $0° \leq \theta < 20°$, the square root of the normalized energy release rate is within 15% of the analytical value. As θ increases and as the friction coefficient μ at the inclined interface increases, this dimensionless parameter increases. However, it remains bounded. Simulations show that $F_{eq}/(Kw\sqrt{d}) < 2$ for $0 \leq \theta \leq 60°$ in case of force boundary conditions and $F_{eq}/(Kw\sqrt{d}) < 1.5$ for $0 \leq \theta \leq 45°$. Although the simulations presented here do not model crack propagation, given that $G = G_f$ and $K = K_c$ when the crack advances,
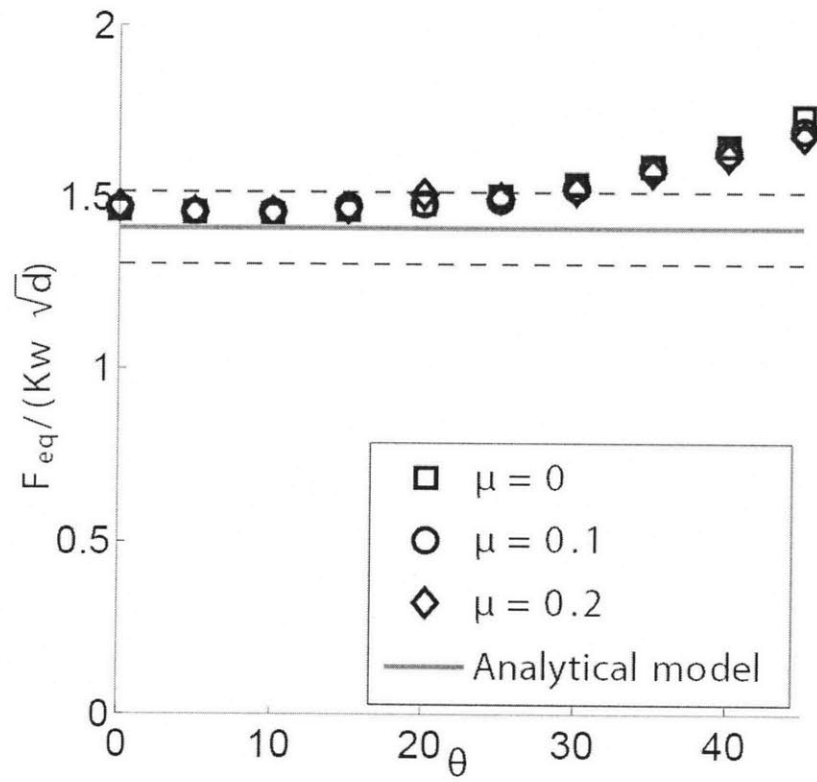
Figure 5-9: Dimensionless parameter $F_{eq}/(Kw\sqrt{d})$ versus θ. Displacement boundary conditions. $K = \sqrt{K_I^2 + K_{II}^2}$. Dotted lines: $\sqrt{2} * (1 \pm 7.5\%)$
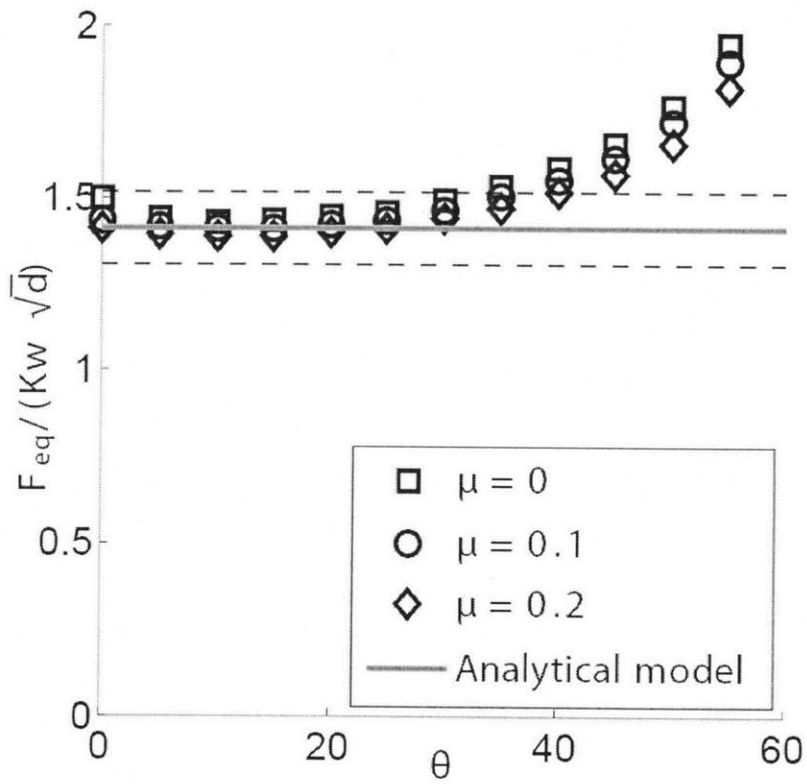
Figure 5-10: Dimensionless parameter $F_{eq}/(Kw\sqrt{d})$ versus θ. Force boundary conditions. $K = \sqrt{K_I^2 + K_{II}^2}$. Dotted lines: $\sqrt{2} * (1 \pm 7.5\%)$

we can conclude that for $0° \leq \theta < 20°$ the analytical solution Eqs. (4.14) and (4.31) give the fracture toughness within an accuracy greater than 85%.

5.4 Chapter Summary

The aim of this chapter was to assess the accuracy of the analytical models derived in Chapter 5. A 2-D Finite Element model was developed to simulate scratch tests with a rectangular blade and a back-rake angle of $0 \leq \theta \leq 60°$. Both force and displacement boundary conditions were considered as well as friction effects at the blade-material interface. Simulations show that mode II is the dominant mode of fracture propagation. Simulations identify the domain of application of our models as the interval of back-rake angles: $0 \leq \theta \leq 20°$. Therefore for this range of θ, we have a highly accurate model for linear elastic isotropic brittle materials that allows one to determine the fracture toughness from results of scratch tests. The possibilities offered by the models will be illustrated in the next part of this thesis through the development of an inverse application scheme and its application to some interesting materials, cement paste, Jurassic limestone, red sandstone and Vosges sandstone.

Part III

From Inverse to Industrial

Applications

Chapter 6

Inverse Application Scheme

The last part of the thesis is devoted to the application of the validated fracture scratch model to the determination of the fracture toughness of different materials. This part is composed of two chapters. This chapter develops an inverse application based on the analytical model developed in Section 4.2.2, for scratch tests with a small back-rake angle, that is, within the domain of application of the model as discussed in Chapter 5. We then confront the predicted toughness values with results from conventional fracture testing methods such as three-point bending tests on notched specimens. In particular, we apply the inverse application scheme to cement paste, Jurassic limestone, red sandstone and Vosges sandstone. We start by presenting the materials, then we describe the two techniques that compose our scheme and finally we discuss the accuracy and limits of the proposed methods. The next chapter then will present an example of industrial application of the method to oil cement slurries hydrated at high temperatures and pressures.

6.1 Materials and Methods

6.1.1 Materials and Fracture Properties

For the development of an inverse scheme for fracture toughness determination, we consider four materials: cement paste, Jurassic limestone, red sandstone and Vosges sandstone. The cement paste material is a based-line oil-cement of Schlumberger: a class G cement hydrated at ambient conditions with no mixed additives. Its slurry density is 1.9 g/cc, which corresponds to a solid volume fraction of 41.5% and a water-to-cement ratio is equal to 0.44. The detailed composition of class G cement is given in Table 6.1. The Jurassic limestone, red sandstone and Vosges limestone are materials of Epslog S.A., who carried out the scratch tests. For purpose of comparison, the fracture properties of similar materials found in the literature will serve as reference values for the inverse application schemes. For cement paste, the reported fracture toughness values were obtained by three-point bending tests on large notched specimen, $K_c = 0.67$ MPa$\sqrt{\text{m}}$ [18], or by means of extrapolation techniques that avoid interference with specimen size, $K_c = 0.65$ MPa$\sqrt{\text{m}}$ [25]. As for sandstone, Ferreira et $al.$ [22] performed three-point bending tests on notched sandstone beams and found $K_c = 1.01$ MPa$\sqrt{\text{m}}$. Barker [8], using specimens configurations that exhibited initial crack growth stability, measured a fracture toughness value of $K_c = 0.73$ MPa$\sqrt{\text{m}}$ for dry silt stones. This value can be used as an approximation for the toughness value of the Vosges sandstone tested here, because these Vosges sandstone have a composition close to that of a cemented silt stone. In order to estimate the fracture process zone, r_c, we approximate the tensile strength σ_0 by $UCS/10$. r_c is then given by [34, 26, 34]:

$$r_c = \frac{1}{2\pi} \left(\frac{K_c}{\sigma_0} \right)^2 \tag{6.1}$$

We assume a uniaxial compressive strength of 60MPa, 45-60 MPa, 60-130 MPa and 20-30 MPa for cement paste, Jurasssic limestone, red sandstone and Vosges sandstone,

Composition of Portland Cement/ Class G				
CaO	SiO$_2$	Al$_2$O$_3$	Fe$_2$O$_3$	minor elements
67%	22%	5%	3%	3%

Table 6.1: Typical composition of a Class G oil well Portland Cement (In Mass%).

respectively. This yields the following estimates for r_c: 1.6 mm, 2-7 mm, 1-5 mm, and 10-20 mm for cement paste, Jurasssic limestone, red sandstone and Vosges sandstone, respectively.

6.1.2 Scratch Device

All scratch tests were carried out by Epslog S. A. [20] with a Wombat scratch tester like the one shown in Fig. 6-1. During these tests, a polycrystalline diamond blade, with a back-rake angle of $\theta = 15°$, traces a groove of fixed width, w, and depth, d, at a constant velocity of a few mm/s. The blade is held by a rigid steel frame with a compliance smaller than 0.027 mm/kN. The forces generated, F_T and F_V, are measured at a high sampling rate, 10 measurements/mm, by force sensors with a maximal capacity of 4,000 N and an absolute precision of 1 N. Simultaneously, the depth of the scratch d is measured with an absolute precision of 0.01 mm.

6.1.3 Data Treatment

Three series of approximately 25 scratch tests each were performed on cement paste. Each series differs by the width, $w = 2.5, 5, 10$ mm. The depth of the scratch d ranged from 0.09 mm to 0.6 mm and the width-to-depth ratio, w/d ranged from 4 to 111, spanning nearly two orders of magnitude. As for Jurassic limestone, four series of five tests each were performed, corresponding to different scratch widths $w = 2.5, 5, 10, 15$ mm. d ranged from 0.1 mm to 0.5 mm and w/d from 5 to 150. Four widths, $w = 2.5, 5, 10, 15$ mm, were also considered for red sandstone. The total number of tests performed were 20; d ranged from 0.1 mm to 0.4 mm while w/d ranged from 7 to 100. As for Vosges
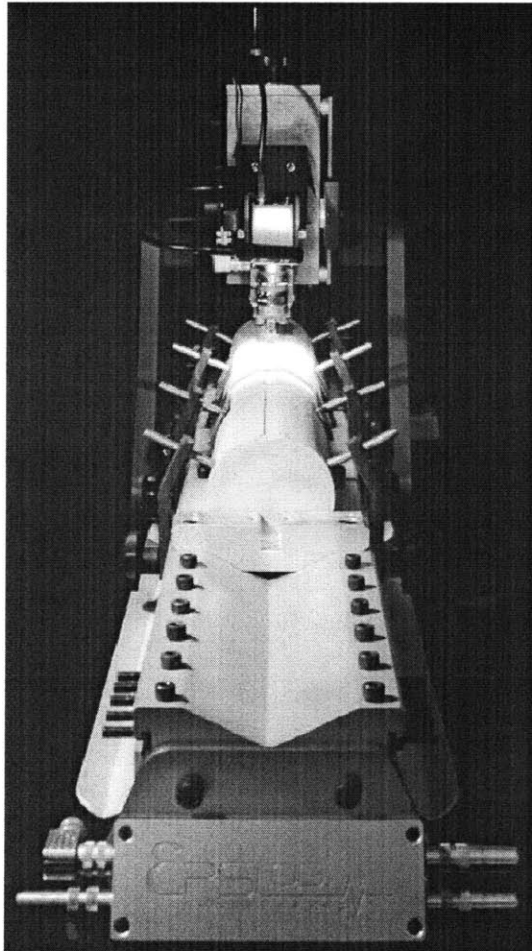
Figure 6-1: Wombat scratch tester. Source [20]

sandstone, four series of 4-5 tests corresponding to the widths $w = 2.5, 5, 10, 15$mm were carried out. d ranged from 0.25 to 0.5 mm and w/d from 5 to 60. The scratch tests data for cement paste presented here were already used in Section Scratch Strength Perspective to illustrate Schei et $al.$ [35, 36] and Bard and Ulm [7] strength methods. This data as well as those from red and Vosges sandstone were also used in Section 2.4 to challenge both Atkins' [3, 4, 2] and Patel et $al.$'s [28] fracture methods.

Fig. 6-2 shows a representative scratch test time series for $w = 10mm$ and $d = 0.2$ mm; the data is from cement paste. For each scratch tests, the horizontal and the vertical forces, F_T and F_V respectively, are averaged over a scratch patch of 3-4 mm. The average value $< F_{eq} >$ and standard deviation ΔF_{eq} of the equivalent force $F_{eq} = \sqrt{F_T^2 + \frac{3}{5}F_V^2}$ were approximated by:

$$< F_{eq} > = \left\langle \sqrt{F_T{}^2 + \frac{3}{5}F_V{}^2} \right\rangle \tag{6.2}$$

$$\Delta F_{eq} = \sqrt{\left\langle F_T{}^2 + \frac{3}{5}F_V{}^2 \right\rangle - \left\langle \sqrt{F_T{}^2 + \frac{3}{5}F_V{}^2} \right\rangle^2} \tag{6.3}$$

6.2 Inverse Schemes

In contrast to the scratch analysis on paraffin wax presented in Chapter 3, and supported by theory developments in Chapter 4, the aim of an inverse scheme is to estimate the fracture toughness from scratch data. The model as expressed by Eqs. (4.33) and (4.16), and recalled below, allows two concurrent methods for fracture toughness measurement:

$$\frac{F_T}{K_c w \sqrt{d}} \leq \sqrt{2\left(1 + 2\frac{d}{w}\right)} \text{ if } \theta = 0 \tag{6.4}$$

$$\frac{\sqrt{F_T^2 + \frac{3}{5}F_V^2}}{K_c w \sqrt{d}} \leq \sqrt{2\left(1 + 2\frac{w}{d}\right)} \text{ if } \theta > 0 \tag{6.5}$$
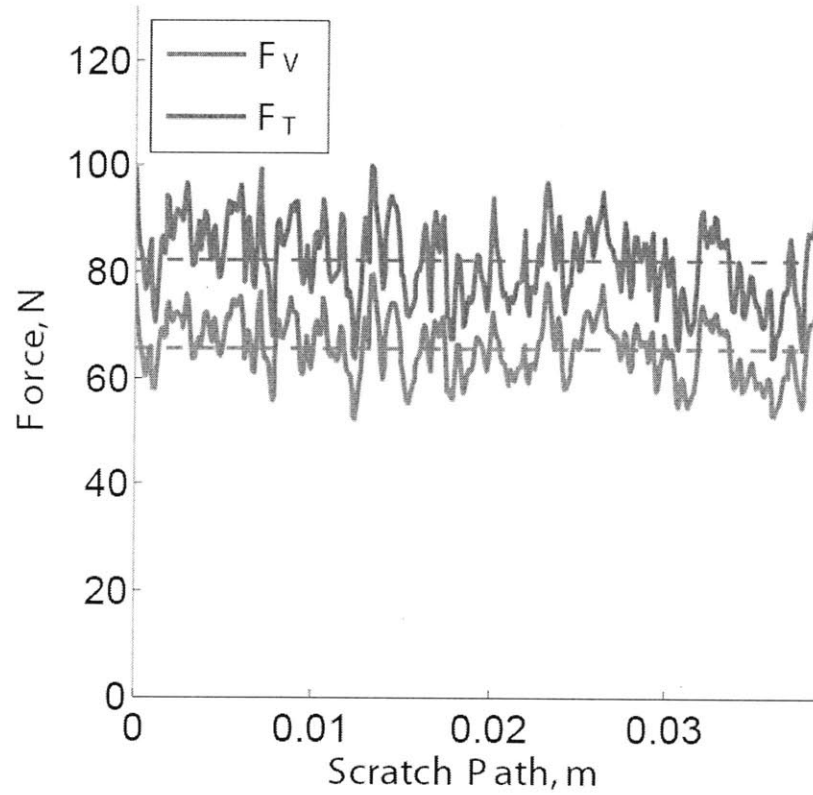
Figure 6-2: Example of scratch test result: measured vertical F_V and horizontal F_T forces along the scratch path. The dotted lines represent the mean F_V and F_T values. Test on cement paste: width $w = 10$ mm, depth $d = 0.1$ mm. The test was carried out by Epslog S. A.; data courtesy of Schlumberger.

6.2.1 Scheme 1: Linear Fitting of the Equivalent Force

The first scheme consists in a linear fit of the equivalent force F_{eq} versus $w\sqrt{d}$ for each width w:

$$K_c^w = \left.\frac{dF_{eq}}{d(w\sqrt{2d})}\right|_{w=constant} \tag{6.6}$$

K_c^w is the slope of the curve $(F_{eq}, w\sqrt{2d})$. In the light of the theoretical development of Chapter 4, this scheme assumes large values of w/d for each test series, which may well be one of its limitations.

6.2.2 Scheme 2: non-linear Fitting of the Normalized Force

This scheme is based on the invariant form Eq. (6.5). In this scheme, the normalized force, $F_{eq}/w\sqrt{2d}$, converges to K_c for large w/d values. This scheme estimates directly the asymptotic value K_c by fitting the normalized force with a particular type of function. In this thesis we consider two fitting functions:

- From the asymptotic development of $\sqrt{1 + 2/x}$, given in Eq. (6.7), $K_c\sqrt{2}$ can be approximated by a polynomial function of $1/x$ with $x = w/d$. We restrict ourselves to a 3rd degree polynomial, given in Eq. (6.8).

$$\sqrt{1 + \frac{2}{x}} = 1 + \frac{1}{x} - \frac{1}{2x^2} + \frac{1}{2x^3} + O\left(\frac{1}{x^4}\right), x \to +\infty \tag{6.7}$$

$$y = a_0 + \frac{a_1}{x} + \frac{a_2}{x^2} + \frac{a_3}{x^3}, \ a_0 > 0, a_3 > 0 \tag{6.8}$$

We require the first constant, a_0 and the last constant, a_3, to be positive to avoid negative values of the fitted normalized force function. In return, a_0 gives the size-independent fracture toughness.

- The second fitting function is an exponential decay function:

$$y = ae^{-bx} + c, \ b \leq 0 \tag{6.9}$$

In which c gives the size-independent fracture toughness. As we will see, the advantage of the exponential decay function is a greater precision on the asymptotic value, resulting in reduced confidence intervals.

To perform the non-linear fitting, the MATLAB bisquare weights algorithm is used. This flexible algorithm makes it possible to define interval bounds for the fitting constants. Moreover it yields confidence intervals for the fitted constants: we choose to have confidence intervals at 95%.

6.3 Results and Discussion

6.3.1 Inverse Scheme 1

Figs. 6-3a)-6-6a) display the strength scaling for the materials presented above. The slopes of the doted lines represent the intrinsic specific energy ε as defined by Eq. (2.23). For all four materials, ε decreases with w, confirming once more that strength drives the test only for small values of wd. For greater values of wd, fracture dissipation becomes predominant and this is corroborated by the highly curved shape of the plot (F_T, wd). By application of Eq. (2.24), the scratch hardness is 67.68±2.07 MPa, 21.48±1.27 MPa, 146.70±28.77 MPa and 54.37±5.23 MPa for cement paste, Jurassic limestone, red sandstone and Vosges sandstone, respectively. For red sandstone in particular, cf Fig 6-5a), the data points (F_T, wd) do not go through the origin. This initial offset, in the horizontal force, can be attributed to frictional dissipation resulting for instance from the presence of a flat wear on the blade.

Figs. 6-3b)-6-6b) apply the first scheme to the materials of this study. For each value of w, there is a linear scaling between the equivalent force F_{eq} and $w\sqrt{d}$: this indicates
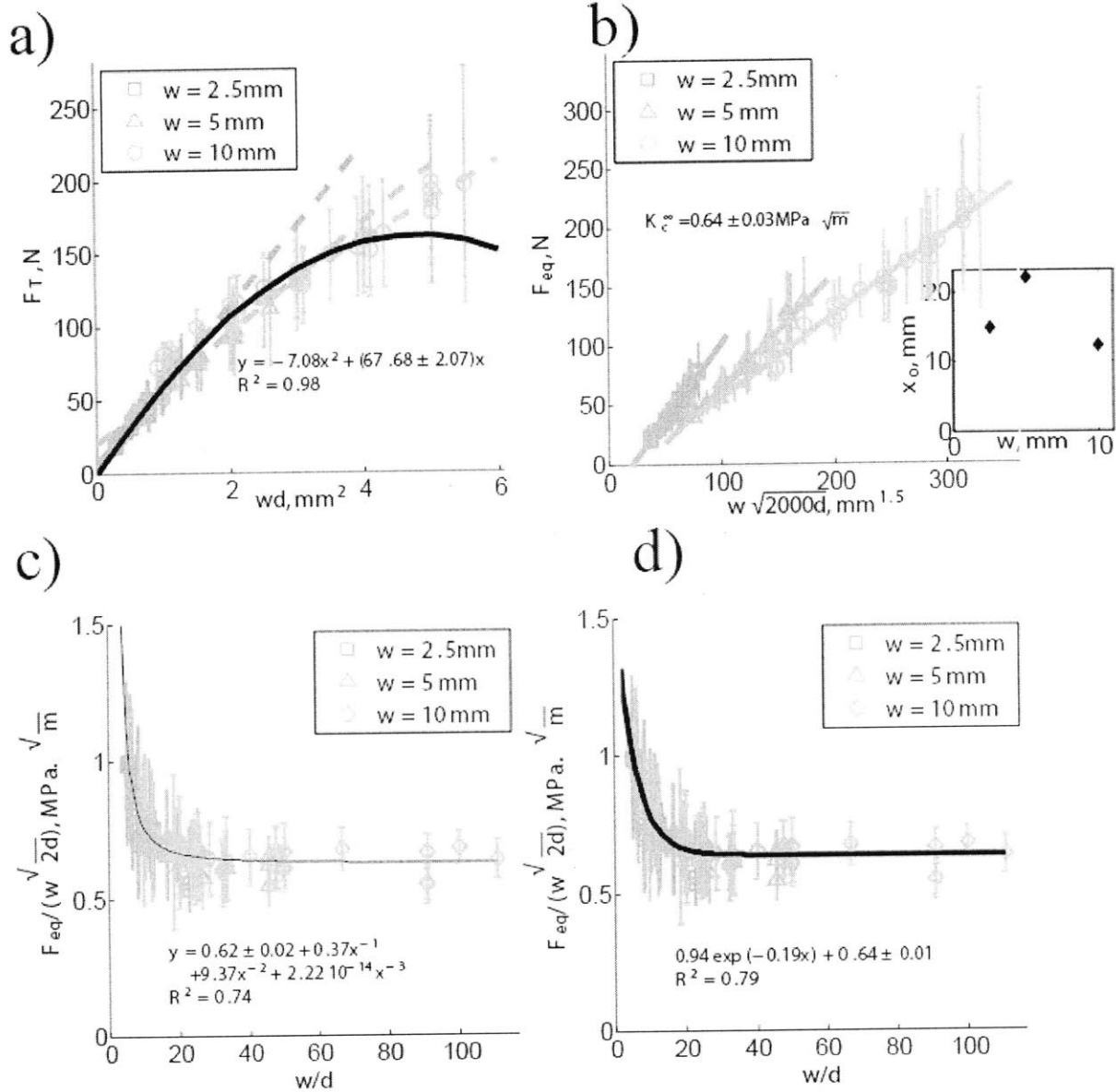
Figure 6-3: Scratch tests on cement paste w/c=0.44. a) Strength scaling. The slopes of the dotted lines give the intrinsic specific energy ε for each width(cf Eq. (2.23)). The constant value of the quadratic fit , curve in black, yield H_T, cf Eq. (2.24) with a 95% confidence interval. b) Inverse application scheme 2: $F_{eq}/\sqrt{2}$ versus $w\sqrt{d}$. The inset plots the initial offset x_0 versus w. c) Inverse application: scheme 1 with a fitting function that is a polynomial is $1/x$. b) Inverse application: scheme 2 with an exponential decay fitting function. For c) and d), the constant value of the fitting function measures the fracture toughness K_c with a confidence interval of 95%. For a), b), c) and d) the bars represent the standard deviation. Tests carried out by Epslog S. A.; data courtesy of Schlumberger.

Figure 6-4: Scratch tests on Jurassic limestone. a) Strength scaling. The slopes of the dotted lines give the intrinsic specific energy ε for each width(cf Eq. (2.23)). The constant value of the quadratic fit , curve in black, yield H_T, cf Eq. (2.24) with a 95% confidence interval. b) Inverse application scheme 2: $F_{eq}/\sqrt{2}$ versus $w\sqrt{d}$. The inset plots the initial offset x_0 versus w. c) Inverse application: scheme 1 with a fitting function that is a polynomial is $1/x$. b) Inverse application: scheme 2 with an exponential decay fitting function. For c) and d), the constant value of the fitting function measures the fracture toughness K_c with a confidence interval of 95%. For a), b), c) and d) the bars represent the standard deviation. Tests carried out by Epslog S. A.; data courtesy of Schlumberger.

91

Figure 6-5: Scratch tests on red sandstone. a) Strength scaling. The slopes of the dotted lines give the intrinsic specific energy ε for each width(cf Eq. (2.23)). The constant value of the quadratic fit , curve in black, yield H_T, cf Eq. (2.24) with a 95% confidence interval. b) Inverse application scheme 2: $F_{eq}/\sqrt{2}$ versus $w\sqrt{d}$. The inset plots the initial offset x_0 versus w. c) Inverse application: scheme 1 with a fitting function that is a polynomial is $1/x$. b) Inverse application: scheme 2 with an exponential decay fitting function. For c) and d), the constant value of the fitting function measures the fracture toughness K_c with a confidence interval of 95%. For a), b), c) and d) the bars represent the standard deviation. Tests carried out by Epslog S. A.; data courtesy of Schlumberger.

Figure 6-6: Scratch tests on Vosges sandstone. a) Strength scaling. The slopes of the dotted lines give the intrinsic specific energy ε for each width(cf Eq. (2.23)). The constant value of the quadratic fit , curve in black, yield H_T, cf Eq. (2.24) with a 95% confidence interval. b) Inverse application scheme 2: $F_{eq}/\sqrt{2}$ versus $w\sqrt{d}$. The inset plots the initial offset x_0 versus w. c) Inverse application: scheme 1 with a fitting function that is a polynomial is $1/x$. b) Inverse application: scheme 2 with an exponential decay fitting function. For c) and d), the constant value of the fitting function measures the fracture toughness K_c with a confidence interval of 95%. For a), b), c) and d) the bars represent the standard deviation. Tests carried out by Epslog S. A.; data courtesy of Schlumberger.

93

that fracture processes occur even at small scales. K_c^w is given in Table 6.2, with a 95% confidence interval, for all widths. In general, K_c^w decreases with w. For cement paste, it decreases from 1.22±0.14 MPa$\sqrt{m}$ to 0.61±0.05 MPa$\sqrt{m}$. For Jurassic limestone, it decreases from 0.57±0.21 MPa$\sqrt{m}$ to 0.39±0.07 MPa$\sqrt{m}$. For red sandstone, it decreases from 4.58±0.44 MPa$\sqrt{m}$ to 1.06±0.05 MPa$\sqrt{m}$. Finally, for Vosges sandstone, it decreases from 1.69±0.21 MPa$\sqrt{m}$ to 0.92±0.09 MPa$\sqrt{m}$. To evaluate K_c^∞, the asymptotic value of K_c^w, a linear fit is carried out for a certain range of widths. For instance, all widths were considered for cement paste, whereas only the two series with the largest width w were considered for red sandstone. For Jurassic limestone and Vosges sandstone, K_c^w was determined from the largest width, $w = 15$ mm. More generally, the assumption of small scale yielding remains valid as long as all geometric parameters are at least an order of magnitude greater than the fracture process zone r_c [5, 34]. Hence, convergence will occur for values of w greater than the fracture process zone r_c:

$$K_c \approx K_c^\infty = K_c^w(w \gg r_c) \tag{6.10}$$

For instance, for cement paste with a fracture process zone of $r_c \approx 1.6$mm (as evaluated in section 6.1.1), $K_c^w(10mm)$ yields a value close to the literature toughness value, 0.67 MPa$\sqrt{m}$ [18, 25]. The asymptotic toughness value for cement paste, estimated by considering all data points, is $K_c^\infty = 0.64 \pm 0.03$ MPa$\sqrt{m}$. An estimated value for the fracture process zone of red sandstone is $r_c = 1 - 5$ mm and, by considering all data points in the range $w \geq 10$ mm, we obtain an asymptotic toughness value, $K_c^\infty = 1.06 \pm 0.05$ MPa$\sqrt{m}$. This value is in close agreement with the literature value, $K_c = 1.01$ MPa$\sqrt{m}$ [22]. In contrast to cement paste and red sandstone, the asymptotic toughness value, $K_c^\infty = 0.92 \pm 0.09$ MPa$\sqrt{m}$, do not converge to the literature value, $K_c = 0.73$ MPa$\sqrt{m}$ [8] because the widths considered, $w = 2.5 - 15$ mm, are of the same order of magnitude than the fracture process zone $r_c = 10 - 20$ mm.

It should be noted that, in the linear fitting of $(F_{eq}/\sqrt{2}, w\sqrt{d})$, there is an initial offset x_0 that is not accounted for in the analytical model, Eqs. (6.4) and (6.5). The values

94

width (mm)	Cement Paste	Jurassic Limestone	Red Sandstone	Vosges Sandstone
2.5	1.22±0.14	0.57±0.21	4.58±0.44	1.69±0.21
5	0.93±0.07	0.45±0.14	2.47±3.73	1.42±0.13
10	0.61±0.05	0.43±0.06	1.02±0.15	1.24±0.15
15	N/A	0.39±0.07	0.91±0.34	0.92±0.09
K_c^∞	0.64±0.03[a]	0.39±0.07	1.06±0.05[b]	0.92±0.09
r_c (mm)	1.6[c]	2-7[d]	1-5 [e]	10-20[f]
Literature K_c	0.67[g]	N/A	1.01[h]	0.73[i]

Table 6.2: Inverse scheme 1: Fracture toughness values K_c (MPa$\sqrt{\mathrm{m}}$). [a] Considering all data points. [b] Considering only w=10,15 mm. [c] Based on ultimate tensile strength 6 MPa. [d] Based on ultimate tensile strength 4.5-6 MPa. [e] Based on ultimate tensile strength 6- 13 MPa. [f] Based on ultimate tensile strength 2-3 MPa. [g] Source [18, 25]. [h] Source [22]. Source [8].

of x_0 are displayed in the inset in Figs.6-3b)-6-6b : x_0 can be positive or negative and it is not always monotonic. x_0 could result from friction dissipation at the blade-material interface, from plastic dissipation inside the material. x_0 could also be due to residual internal stresses in the material, resulting from sample preparation. Such non-linear phenomena are not taken into account in the linear model developed in this thesis. This limits the general applicability of scheme 1, which is why we considered a second scheme.

6.3.2 Inverse Scheme 2

Figs. 6-3c),d)-6-6c),d) display the quantity $F_{eq}/(w\sqrt{2d})$ fitted with a 3rd degree polynomial function of $1/x$ (Eq. (6.7)) and with an exponential decay function (Eq. (6.8)). For all materials except Vosges sandstone, all data points $(F_{eq}/(\sqrt{2}w\sqrt{d}), w/d)$ collapse into one curve. This is a strong evidence of the validity of the fracture scaling derived in Section 2.2.2 and recalled below:

$$F_T = K_c w\sqrt{d} \times \Pi\left(\frac{\sigma_0}{E}, \nu, \mathcal{I} = \frac{w}{(K_c/\sigma_0)^2}, \theta, \mu\right) \tag{6.11}$$

The two fitting functions considered yield close estimates of the size-independent fracture toughness. The fitting with a 3rd degree polynomial yields $K_c = 0.62 \pm 0.02$

MPa$\sqrt{\text{m}}$, 0.40±0.04 MPa$\sqrt{\text{m}}$, 1.55±0.26 MPa$\sqrt{\text{m}}$, and 0.76±0.18 MPa$\sqrt{\text{m}}$ for cement paste, Jurassic limestone, red sandstone and Vosges sandstone, respectively. Meanwhile the fitting with an exponential decay function yields $K_c = 0.64\pm0.01$ MPa$\sqrt{\text{m}}$, 0.45±0.03 MPa$\sqrt{\text{m}}$, 1.30±0.09 MPa$\sqrt{\text{m}}$, 0.77±0.04 MPa$\sqrt{\text{m}}$ for cement paste, Jurassic limestone, red sandstone and Vosges sandstone, respectively. These estimates are also close to the asymptotic toughness values found using the inverse scheme 1 as well as to the values of fracture toughness for cement paste, red sandstone and Vosges sandstone, reported in the open literature. Finally, fitting with an exponential decay function is more accurate than fitting with a polynomial of $1/x$, which, in turn, is more accurate than the inverse scheme 1.

Fig. 6-7 shows a strong correlation between the scratch tests fracture toughness estimate, estimated with inverse scheme 2 and with an exponential decay function, and reported values. As explained in Section 6.1.1, these literature values were obtained via conventional testing methods such as three-point bending tests on notched specimens or double-cantilever tests.

6.4   Chapter Summary

In this chapter an inverse scheme was developed that allows the assessment of the fracture toughness from results of scratch tests. The first method uses linear fits of the equivalent force F_{eq} whereas the second one uses non-linear fitting of the normalized force $F_{eq}/(w\sqrt{2d})$. Both methods converge for large values of $w\sqrt{d}$ and w/d toward a size-independent fracture toughness that is in good agreement with conventional testing methods such as notched-beam tests or double-cantilever tests. The more robust method among those two schemes is the second method based on the dimensionless scaling relation of the force with w/d. This is the method we recommend for fracture toughness determination from scratch tests.
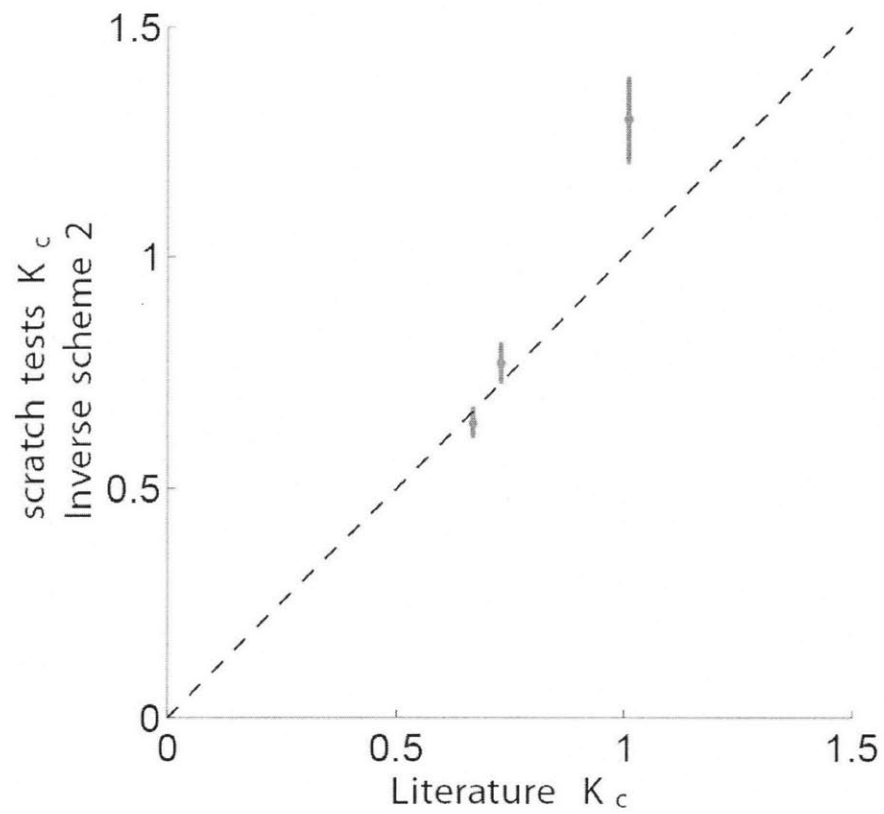
Figure 6-7: Scratch tests model versus conventional fracture testing methods (found in the literature).

Chapter 7

Industrial Applications

The chapter presents an industrial application of the tools developed in this thesis. The application deals with oil cement slurries hydrated at high temperatures and pressures. The focus of this chapter is to show how the scratch test model can be used in such a challenging industry application for both strength and fracture properties determination.

7.1   Industrial Context

The primary objectives of well cementing, that is the placement of cement in the annulus between the pipe or casing and the rock formation, is zonal isolation. That is, the annular cement sheath must isolate zones containing pressurized fluids from each other and from the surface and maintain this isolation even when the cement sheath is subjected to changes in stress and strain during the operating life of the well.

From a mechanics point of view, this objective needs to be met by an appropriate cementitious material that can withstand high temperatures and pressures which are typically encountered in down-hole applications. The key to choosing the appropriate material is a method that allows the control of an appropriate material parameter. Like in the construction materials industry, the classical parameter in use has been the compressive strength of the material, which is part of the cultural baggage of engineers, be

this in infrastructure applications of concrete, or in well-cementing applications. On the other hand, given the objectives of well cementing, one can arguably make the case that the material parameter that controls scaling and stability of the in-situ material does not relate to a limit in strength but rather to a risk of cracking and fracture. A performance based design of such functions would thus need to consider fracture properties; for instance fracture energy or fracture toughness.

The main challenge of using fracture properties in industrial applications is that their determination typically requires a much-more sophisticated test set-up that can deal with fracture size effects inherent to fracture phenomena in brittle and quasi-brittle materials [11], which need to be taken into account in the determination of concrete's fracture properties [18],[25],[24],[19]. The scratch test analysis presented in this thesis offers an attractive alternative. The focus of this chapter thus is to apply this technique in order to shed light on the effect of high temperature and pressure on the fracture toughness of a series of baseline oil well cement formulations.

To this end, we will first present the materials considered in this study. Then, we will apply both a the strength interpretation (see section 2.3.2) and a fracture inverse application scheme to the experimental data.

7.2 Materials and Methods

' The materials considered here are made of class G cement; their composition was given in the previous chapter, Table 6.1. As reference, we consider the cement paste w/c=0.44, used all along in this thesis. With respect to high temperature and pressure applications, two further base-line cement mixes in frequent use in oil well application are investigated. These mixes contain in addition 35% of silica flour (by weight of cement). Silica flour is crystalline silica, containing at least 98% silicon dioxide and with a mean particle size around 20 microns. It is formed by grinding of quartz sand in ball or vibration mills. For comparison with the reference sample the two materials where designed either at the

		Reference	Sample A	Sample B
Slurry Density	g/cc	1.9	2.03	1.89
w/c	M%	44	45	58
w/b	M%	44	33	43
s/c	M%	0	35	35
		Curing Conditions		
Temperature	°C	25	200	1 week 50, then 300
Pressure	MPa	Atm.	20.7	20.7
Duration	week		1 (A-1w)	4 (B-4w)
	week		51 (A-51w)	8 (B-8w)
	week			12 (B-12w)

Table 7.1: Tested Oil-well cement samples. Mix formulation and temperature pressure curing conditions.

same water–to–cement mass ratio or the same water–to–binder mass ratio. Sample A of slurry density 2.03 g/cc contains 70 Vol% of class G cement and 30 Vol% of silica flour. This corresponds to a solid volume fraction of 50% representative of a water to binder mass ratio of $w/b = 0.33$, and a water to cement ratio of $w/c = 0.45$. Sample series B of slurry density 1.89 g/cc and solid volume fraction of 43.9% has almost the same water–to–binder mass ratio as the reference sample ($w/b = 0.43$); yet due to the the solid mix of 70.3 Vol% cement and 29.7 Vol% of silica flour ($s/c = 0.35$), its water-to-cement ratio is significantly higher, $w/c = 0.58$. Finally, each sample series was subjected to different curing conditions: The curing temperature of sample A is 200°C and the pressure is 20.7 MPa, applied 1 week and 12 months, respectively. Sample B was cured for 1 week at 50°C and then subjected to a temperature of 300°C and a pressure of 20.7 MPa for 1 month, 2 months and 3 months, respectively. All materials were prepared by Schlumberger (Simon James). Table 7.1 summarizes the different mixes and curing conditions and durations considered in this study.

7.2.1 Scratch Hardness and Scratch Toughness Determination

The scratch test device considered here is the same device as described in Section 6.1.2: an inclined blade of back-rake angle $\theta = 15°$ and of out-of-plane width w is held at a

Figure 7-1: Scratch tests on sample A-1w. a) Strength scaling. The slopes of the dotted lines give the intrinsic specific energy ε for each width(cf Eq. (2.23)). The constant value of the quadratic fit , curve in black, yield H_T, cf Eq. (2.24) with a 95% confidence interval. b) Inverse application scheme 2: $F_{eq}/\sqrt{2}$ versus $w\sqrt{d}$. The inset plots the initial offset x_0 versus w. c) Inverse application: scheme 1 with a fitting function that is a polynomial is $1/x$. b) Inverse application: scheme 2 with an exponential decay fitting function. For c) and d), the constant value of the fitting function measures the fracture toughness K_c with a confidence interval of 95%. For a), b), c) and d) the bars represent the standard deviation. Tests carried out by Epslog S. A.; data courtesy of Schlumberger.

101

Figure 7-2: Scratch tests on sample A-51w. a) Strength scaling. The slopes of the dotted lines give the intrinsic specific energy ε for each width(cf Eq. (2.23)). The constant value of the quadratic fit , curve in black, yield H_T, cf Eq. (2.24) with a 95% confidence interval. b) Inverse application scheme 2: $F_{eq}/\sqrt{2}$ versus $w\sqrt{d}$. The inset plots the initial offset x_0 versus w. c) Inverse application: scheme 1 with a fitting function that is a polynomial is $1/x$. b) Inverse application: scheme 2 with an exponential decay fitting function. For c) and d), the constant value of the fitting function measures the fracture toughness K_c with a confidence interval of 95%. For a), b), c) and d) the bars represent the standard deviation. Tests carried out by Epslog S. A.; data courtesy of Schlumberger.

a)

$y = -8.07x^2 + (71.64 \pm 5.02)x$
$R^2 = 0.98$

Legend: $w = 2.5\,mm$, $w = 5\,mm$, $w = 10\,mm$

y-axis: F_T, N

x-axis: wd, mm^2

b)

$K_c^\infty = 0.64 \pm 0.06\,MPa\,\sqrt{m}$

Legend: $w = 2.5\,mm$, $w = 5\,mm$, $w = 10\,mm$

y-axis: F_{eq}, N

x-axis: $w\sqrt{2000d}$, $mm^{1.5}$

Inset y-axis: x_o, mm; x-axis: w, mm

c)

$y = 0.49 \pm 0.12 + 8.54x^{-1}$
$-143.35x^{-2} + 905.91x^{-3}$
$R^2 = 0.66$

Legend: $w = 2.5\,mm$, $w = 5\,mm$, $w = 10\,mm$

y-axis: $F_{eq}/(w\sqrt{2d})$, $MPa.\sqrt{m}$

x-axis: w/d

d)

$0.23\exp(-0.026x) + 0.54 \pm 0.11$
$R^2 = 0.63$

Legend: $w = 2.5\,mm$, $w = 5\,mm$, $w = 10\,mm$

y-axis: $F_{eq}/(w\sqrt{2d})$, $MPa.\sqrt{m}$

x-axis: w/d

Figure 7-3: Scratch tests on sample B-4w. a) Strength scaling. The slopes of the dotted lines give the intrinsic specific energy ε for each width(cf Eq. (2.23)). The constant value of the quadratic fit , curve in black, yield H_T, cf Eq. (2.24) with a 95% confidence interval. b) Inverse application scheme 2: $F_{eq}/\sqrt{2}$ versus $w\sqrt{d}$. The inset plots the initial offset x_0 versus w. c) Inverse application: scheme 1 with a fitting function that is a polynomial is $1/x$. b) Inverse application: scheme 2 with an exponential decay fitting function. For c) and d), the constant value of the fitting function measures the fracture toughness K_c with a confidence interval of 95%. For a), b), c) and d) the bars represent the standard deviation. Tests carried out by Epslog S. A.; data courtesy of Schlumberger.

103

a)

$y = -8.49x^2 + (76.28 \pm 6.14)x$
$R^2 = 0.98$

b)

$K_c^\infty = 0.65 \pm 0.05\text{MPa } \sqrt{m}$

c)

$y = 0.56 \pm 0.15 + 6.96x^{-1}$
$\quad - 125.57x^{-2} + 858.05x^{-3}$
$R^2 = 0.56$

d)

$1.63 \exp(-0.21x) + 0.64 \pm 0.04$
$R^2 = 0.38$

Figure 7-4: Scratch tests on sample B-8w. a) Strength scaling. The slopes of the dotted lines give the intrinsic specific energy ε for each width(cf Eq. (2.23)). The constant value of the quadratic fit , curve in black, yield H_T, cf Eq. (2.24) with a 95% confidence interval. b) Inverse application scheme 2: $F_{eq}/\sqrt{2}$ versus $w\sqrt{d}$. The inset plots the initial offset x_0 versus w. c) Inverse application: scheme 1 with a fitting function that is a polynomial is $1/x$. b) Inverse application: scheme 2 with an exponential decay fitting function. For c) and d), the constant value of the fitting function measures the fracture toughness K_c with a confidence interval of 95%. For a), b), c) and d) the bars represent the standard deviation. Tests carried out by Epslog S. A.; data courtesy of Schlumberger.

104

a)

Legend: w = 2.5mm (□), w = 5 mm (△), w = 10 mm (○)

F_T, N (y-axis), wd, mm^2 (x-axis)

$y = -7.98x^2 + (76.75 \pm 7.73)x$
$R^2 = 0.97$

b)

Legend: w = 2.5mm (□), w = 5 mm (△), w = 10 mm (◇)

F_{eq}, N (y-axis), $w\sqrt{2000d}$, mm$^{1.5}$ (x-axis)

$K_c^\infty = 0.69 \pm 0.06 \text{MPa} \sqrt{m}$

Inset: x_o, mm vs w, mm

c)

Legend: w = 2.5mm (□), w = 5 mm (△), w = 10 mm (○)

$F_{eq}/(w\sqrt{2d})$, MPa. $\sqrt{m}$ (y-axis), w/d (x-axis)

$y = 0.62 \pm 0.20 + 5.01x^{-1}$
$\quad - 103.24x^{-2} + 807.10x^{-3}$
$R^2 = 0.45$

d)

Legend: w = 2.5mm (□), w = 5 mm (△), w = 10 mm (◇)

$F_{eq}/(w\sqrt{2d})$, MPa. $\sqrt{m}$ (y-axis), w/d (x-axis)
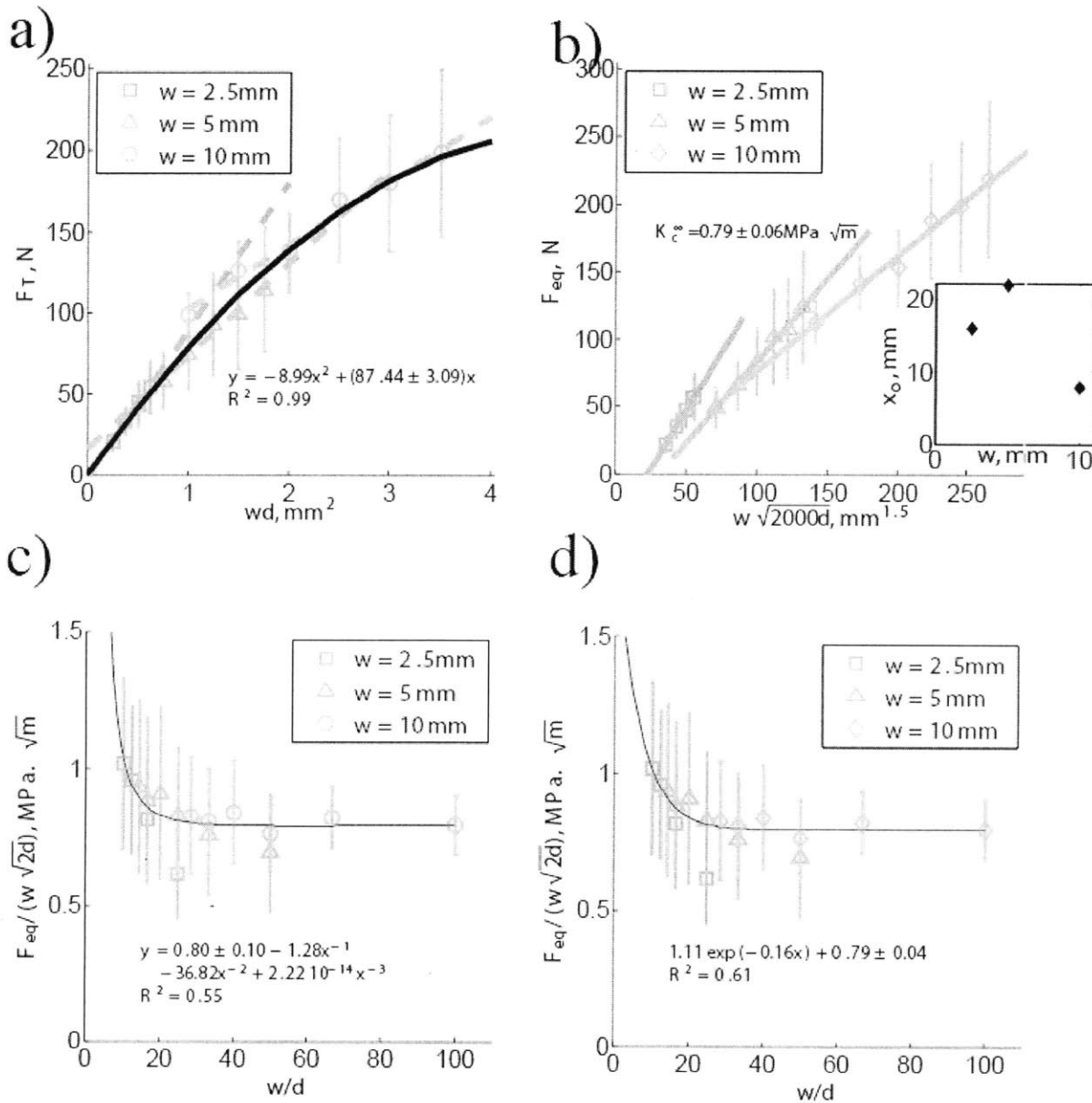
$2.80\exp(-0.27x) + 0.68 \pm 0.04$
$R^2 = 0.47$

Figure 7-5: Scratch tests on sample B-12w. a) Strength scaling. The slopes of the dotted lines give the intrinsic specific energy ε for each width(cf Eq. (2.23)). The constant value of the quadratic fit , curve in black, yield H_T, cf Eq. (2.24) with a 95% confidence interval. b) Inverse application scheme 2: $F_{eq}/\sqrt{2}$ versus $w\sqrt{d}$. The inset plots the initial offset x_0 versus w. c) Inverse application: scheme 1 with a fitting function that is a polynomial is $1/x$. b) Inverse application: scheme 2 with an exponential decay fitting function. For c) and d), the constant value of the fitting function measures the fracture toughness K_c with a confidence interval of 95%. For a), b), c) and d) the bars represent the standard deviation. Tests carried out by Epslog S. A.; data courtesy of Schlumberger.
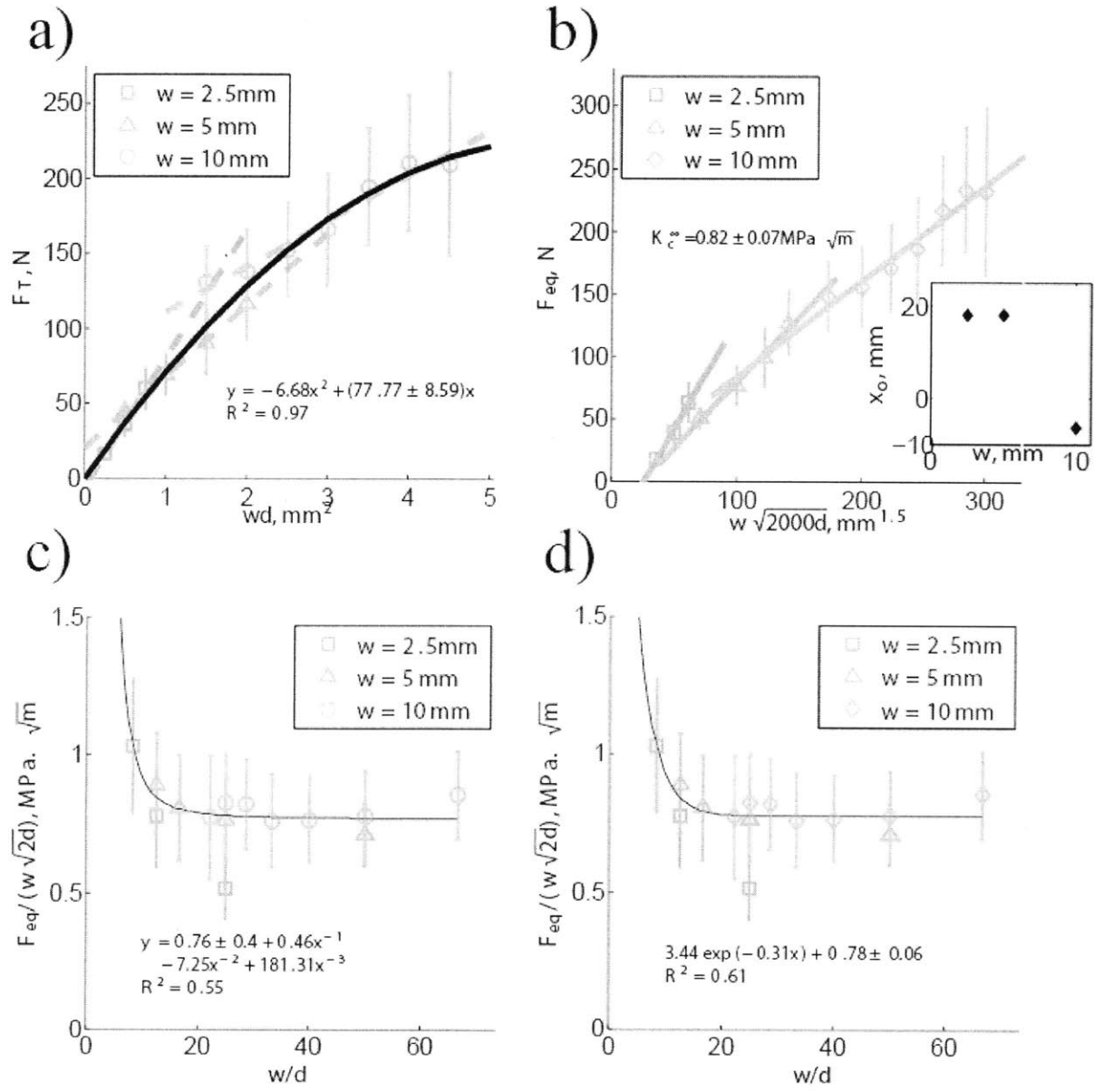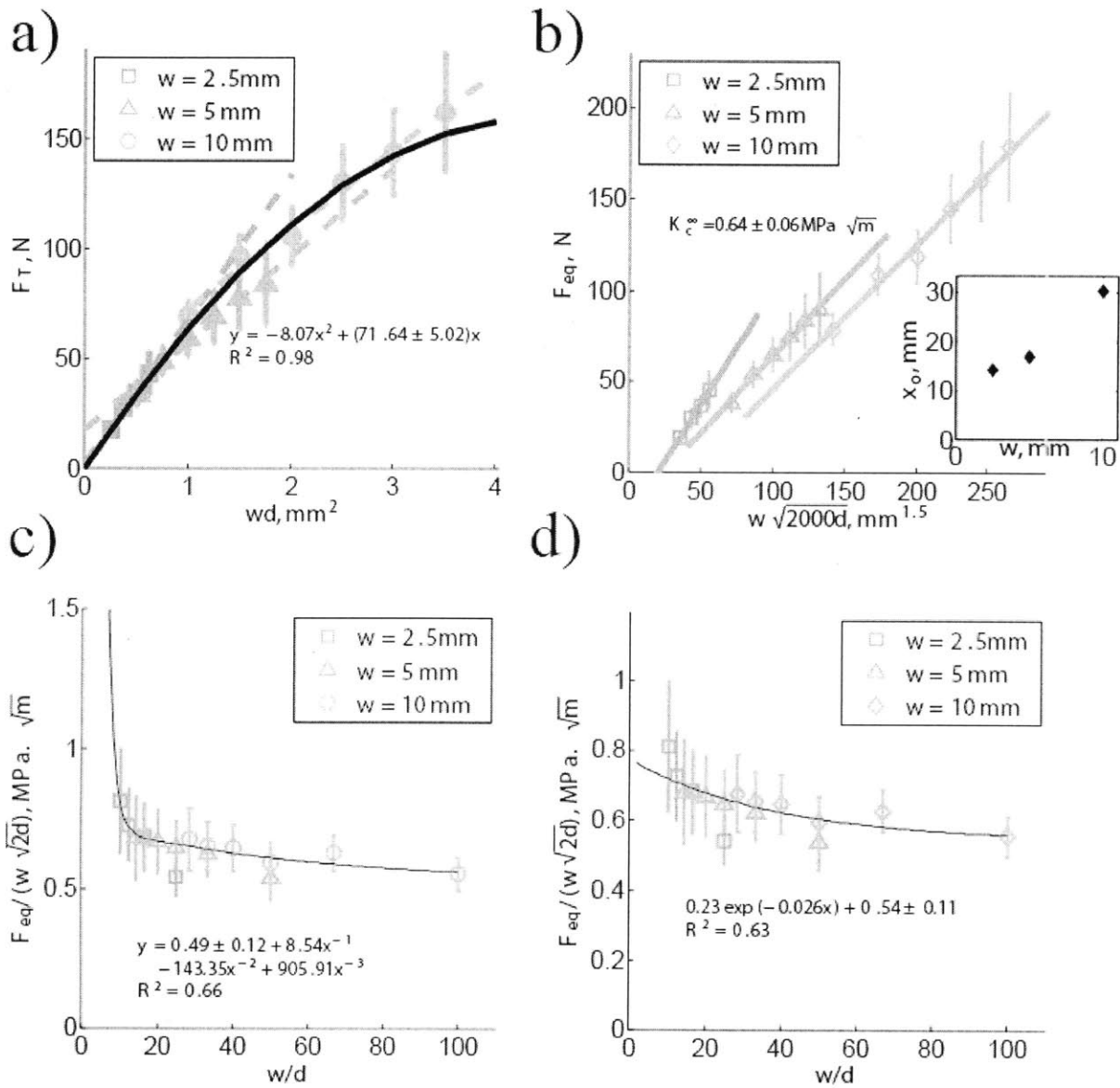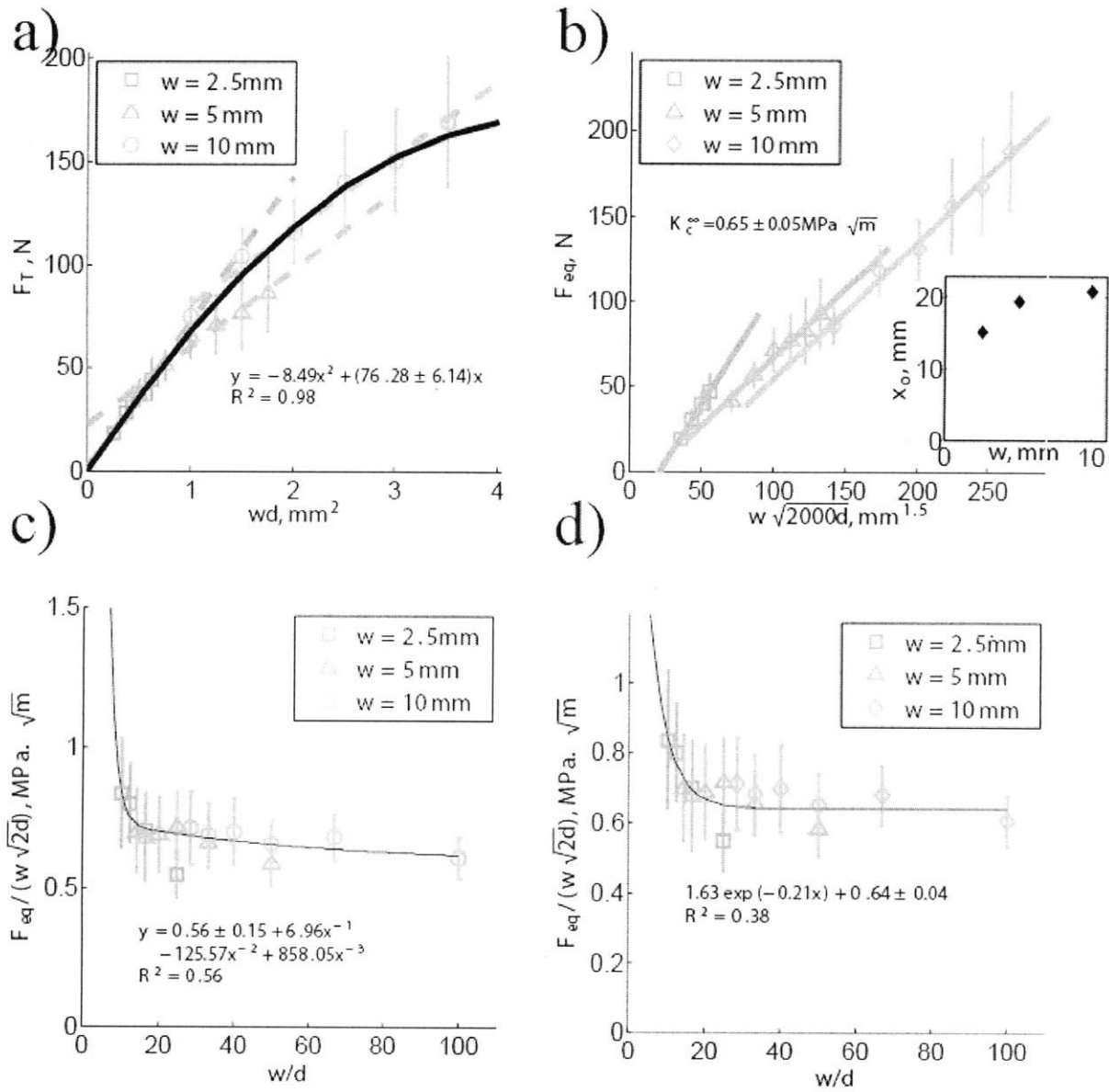
depth d by means of a vertical force F_V. A horizontal force F_T is applied to move the blade over a scratch length of 5 cm. For each material sample and curing conditions, we carry out such tests with three different widths, $w = 2.5, 5, 10$ mm; and up to six different depths, varying between $d = 0.1$ mm and $d = 0.35$ mm; typically a total number of 16 scratch tests per sample; thus spanning a large range of w/d ratios between 10 and 100. The strength interpretation presented in Section 2.3 and the fracture model developed in Chapter 4 are both applied to assess the strength and fracture properties of the materials.

Strength Interpretation

Figs. 7-1a)-7-4a) display the horizontal force F_T versus the projected contact area $A_{LB} = wd$ for all materials except cement paste w/c=0.44. As expected, there is a linear scaling for small values of wd, however at greater values, the curve becomes non-linear. This confirms the predominance of plastic yielding at small widths and depths and the prevalence of fracture dissipation at large widths and depths. The scratch hardness is estimated from Eq. (2.24), which we recall below :

$$H_T = \left. \frac{dF_T}{d(wd)} \right|_{wd=0} \qquad (7.1)$$

The relationship between the scratch hardness and the uniaxial compressive strength, developed by Bard and Ulm [7] and listed in Table 2.3.2 is used to characterize the strength properties of the materials. In particular, if the ratio of the scratch hardness to the uniaxial compressive strength, H_T/UCS is strictly greater than $1+\sin\theta$ (value for a Tresca type criterion) the material exhibits internal friction. Given that we are dealing with cementitious materials, we can discard any symmetric and hydrostatic pressure-independent criteria like the Von-Mises criteria. Moreover, if we assume that the material obeys a Mohr-Coulomb type criterion, the scratch hardness, H_T, and the uniaxial compressive

106

strength, UCS, are linked to the cohesion, C, and to the internal friction angle, φ, by:

$$H_T = 2C \frac{\cos\varphi \left(1 - \sin^2\theta\right)}{1 - \sin\theta \cos\varphi\sqrt{1 + (\tan\varphi\sin\theta)^2} - \sin\varphi\cos^2\theta} \qquad (7.2)$$

$$UCS = 2C \frac{\cos\varphi}{1 - \sin\varphi} \qquad (7.3)$$

Therefore, from the results of scratch tests and from independent measurements of the uniaxial compressive strength, one can estimate the cohesion and the internal friction angle.

Fracture Inverse Application

We apply the inverse application method developed in Chapter 6 to evaluate the fracture toughness. This scheme is based on the analytical expression derived in Chapter 4:

$$\frac{F_{eq}}{w\sqrt{d}} \leq K_c\sqrt{2\left(1 + 2\frac{w}{d}\right)} \qquad (7.4)$$

$$F_{eq} = \sqrt{F_T^2 + \frac{3}{5}F_V^2} \quad \text{if } \theta > 0 \qquad (7.5)$$

The first scheme approximates K_c by the asymptotic value K_c^∞ of the slope, at fixed width, of the plot $(F_{eq}, w\sqrt{2d})$. The second scheme directly fits the curve $(F_{eq}/(w\sqrt{2d}), w/d)$ with either a polynomial function of $1/x$ (i.e. Eq. (6.7)), or an exponential decay function (i.e. Eq. (6.8)), and approximates K_c by the asymptotic value of the fitting function.

Figs. 7-1 b), c)and d)-7-5 b), c) and d) display the fracture scaling obtained for all materials except the reference cement paste. Some observations are worthwhile mentioning:

- For each width of the blade w, there is a linear scaling between the equivalent force F_{eq} and $w\sqrt{d}$, and the slope decreases with the width w. A plateau is reached for values of w greater than the fracture process zone $r_c = 1/(2\pi)(K_c/\sigma_0)^2$.

- The normalized force $F_{eq}/(w\sqrt{2d})$ converges for large values of w/d toward a con-

Sample	T°C	p/MPa	UCS/MPa	H_T/MPa	C/MPa$^{(*)}$	K_c/MPa.m$^{1/2}$
Reference	25	p_{atm}	43 ± 2	67.7±2.1	14.5	0.64 ± 0.01
A-1w	200	20.7	67 ± 5	87.4±3.1	22.6	0.79 ± 0.4
A-51w	200	20.7	53 ± 5	77.8±8.6	17.9	0.78 ± 0.06
B-4w	300	20.7	57 ± 5	71.6±5.0	19.3	0.54 ± 0.11
B-8w	300	20.7	47 ± 5	76.3±6.1	15.9	0.64 ± 0.04
B-12w	300	20.7	58 ± 5	76.8±7.7	19.8	0.68 ± 0.04

Table 7.2: Results: UCS = unconfined compressive strength (Mean ± St.Dev. of 5 tests); H_T = Scratch hardness; K_c = fracture toughness. (*) Cohesion C is determined from Eq. (7.3) under the assumption of a constant friction angle. Details provided in the text.

stant representative of the fracture toughness.

- Of all the inverse methods presented, the non-linear fitting of of the normalized force, $F_{eq}/(w\sqrt{2d})$, using an exponential decay function (Scheme 2) yields the most accurate estimate of K_c.

These observations confirm those made in Chapter 6, for cement paste, Jurassic limestone, red sandstone and Vosges sandstone.

7.3 Results

Table 7.2 lists for the materials and curing conditions considered the scratch hardness, H_T, and fracture toughness, K_c, determined from each series of scratch tests as described here before; together with the unconfined compressive strength, UCS, determined on cylinder samples. The data display a fair amount of consistency: the general trend is that both the scratch hardness (Fig. 7-6) and the fracture toughness (Figs. 7-7) increase with the compressive strength, UCS. Two observations deserve particular attention: The first relates to the positive correlation of H_T with UCS, the second to the correlation of H_T or UCS with the fracture toughness.
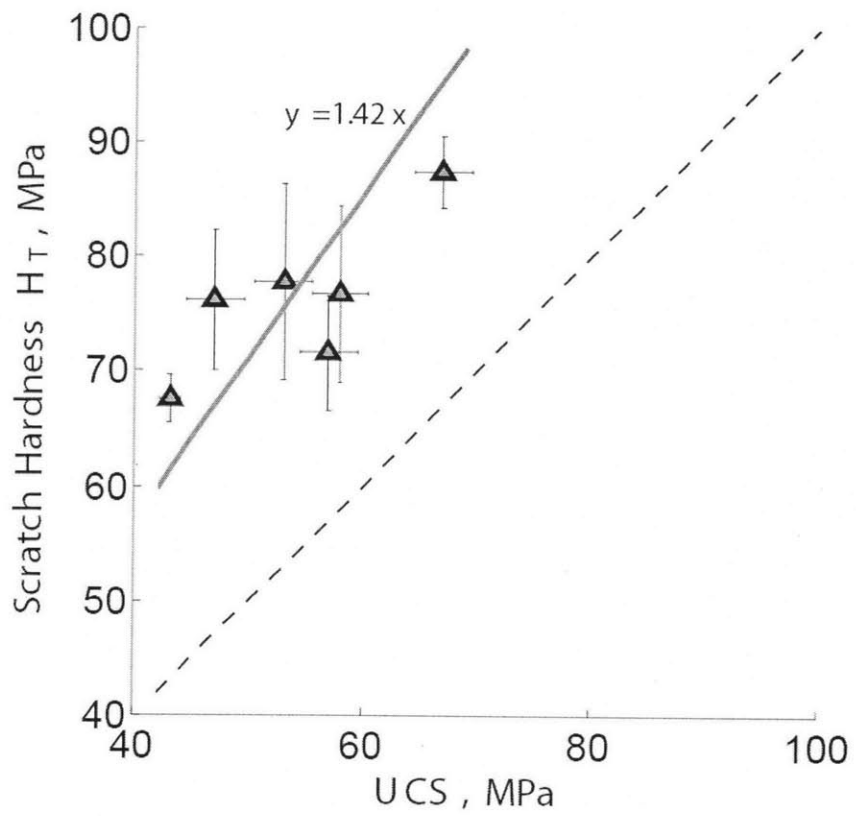
Figure 7-6: Scratch hardness H_T versus UCS. Tests carried out by Epslog S. A.; Data Courtesy of Schlumberger.
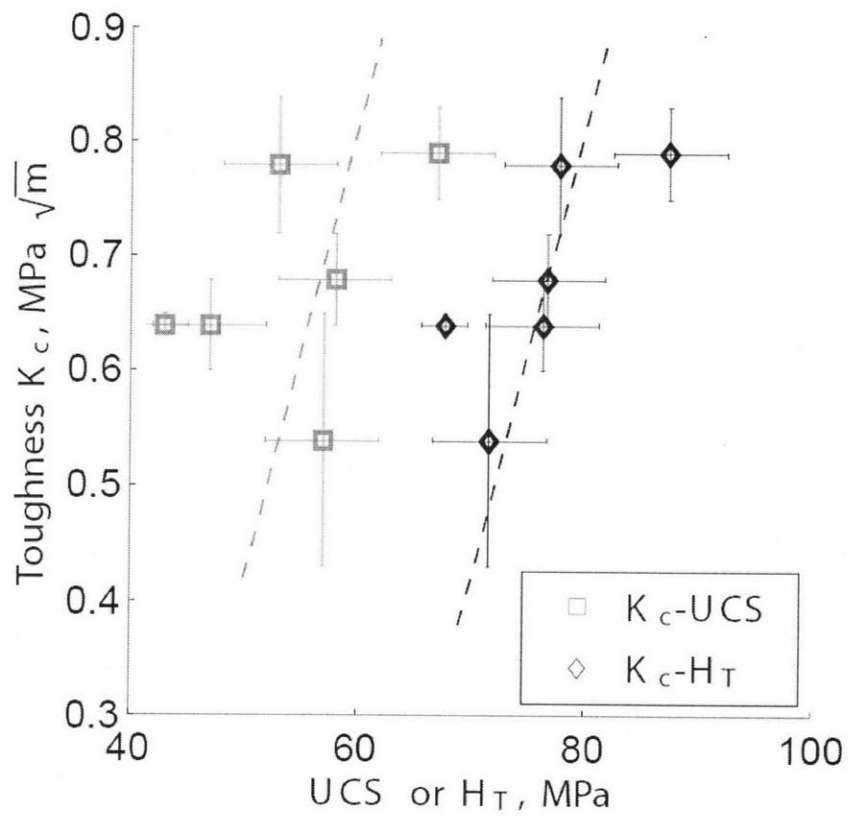
Figure 7-7: Toughness versus UCS or H_T. Tests carried out by Epslog S. A.; Data Courtesy of Schlumberger.

7.3.1 Cohesive-Frictional Strength Behavior

The positive correlation of H_T with UCS(Fig. 7-6) by Bard and Ulm [7] has been recently identified to relate the cohesive-frictional nature of the scratched material. The mean H_T/UCS for all samples is equal to 1.42. This value is strictly greater than $1 + \sin\theta = 1.26$ therefore there is internal friction at play. From Eqs. (7.2) and (7.3), the friction coefficient is $\mu = 0.40$, that is a friction angle of $\varphi = 21.9°$. This value is in very good agreement with previously reported friction angle for oil cement slurries obtained by triaxial testing (confined compressive strength tests) [39],[16]. While there is no doubt some variability in H_s/UCS ratios between samples, the results provide some insight that the dominant source of different scratch hardness is the cohesion of the material. For illustration, Table 7.2 also lists the cohesion values, C, determined with a constant friction angle of $\varphi = 21.9°$ from Eq. (7.3). What thus emerges is that for the same water-to-binder (w/b) mass ratio (compare Reference sample to Sample B), cementitious materials achieve similar values of cohesion that are only slightly affected by the high temperature–pressure curing conditions. This observation is also consistent with the fact that the lower $w/b-$ ratio of the A sample compared to both the reference sample and B-samples entails a higher cohesion. Compared to this dominating effect related to the mix design, the duration of temperature–pressure curing conditions appear, as a second order effect, to affect the frictional behavior. For instance, the H_s/UCS ratio for the A-samples increases from 1.30 to 1.47 due to prolonged curing (compare sample A-1w and A-51w), which corresponds to an increase of the friction coefficient (friction angle) from $\mu_{A-1w} = 0.117$ ($\varphi = 6.7°$) to $\mu_{A-51w} = 0.45$ ($\varphi = 26.02°$). A similar trend is found for samples B-4w and B-8w (but less so for B-12w). Such a variability of the friction angle has also been found in triaxial testing of oil cement slurries [13],[31], for which the method proposed is an attractive alternative.

7.3.2 Toughness–Ductility Behavior

An important observation is the positive correlation between fracture toughness, K_c, on one hand, and UCS or scratch hardness, H_T, on the other hand (Fig. 7-7). In particular, as for scratch hardness, we observe that materials with same w/b ratio display almost the same fracture toughness (compare Reference with Samples B) independent of the different curing conditions. In return, materials with lower w/b ratio exhibit a significant higher fracture toughness (compare Sample A with Reference Sample or Sample B). For many materials, such an increase in fracture toughness is often associated with a higher brittleness respectively a lower ductility. However, the concurrent increase in fracture toughness and hardness, $K_c \sim H_T$, for the samples considered here is an indication that the ductility of the material is preserved across all samples. A good means to quantify the ductility is the characteristic size of the fracture process zone (FPZ), which we estimate from,

$$r_c = \frac{1}{2\pi} \left(\frac{K_c}{C} \right)^2 \tag{7.6}$$

The values for r_c calculated for each sample and curing condition from Table 7.2, vary indeed little around the mean of $r_c = 0.23 \pm 0.07$ mm, without any pronounced relation with strength or hardness. This means that the ductility of the materials tested here is, in first order, independent of the specific mix formulation. Finally, it is useful to note that the size of this fracture process zone is much smaller than the characteristic size of the scratch defined by the blade width w, which a posteriori justifies the use of LEFM for scratch test analysis, i.e. Eq. (7.4).

7.4 Chapter Summary

The aim of this chapter was to show an industrial application of the methods developed throughout this thesis. In particular this chapter has investigated the strength and

fracture properties of oil well cements cured at high temperatures and pressures. This investigation led to two main results. First, the key material design parameter for cohesion and fracture toughness is the water–to–binder ratio (w/b), not the water–to–cement ratio (w/c). Secondly, prolonged high temperature and high pressure curing induces some second order effects, manifesting themselves by a frictional enhancement together with a softening of cohesion and the fracture toughness.

The scratch test thus emerges as a self-consistent technique for both cohesive-frictional strength and fracture properties that are highly relevant for oil-well cementing applications. The fact that it is highly reproducable, almost non-destructive and not more sophisticated than classical compression tests, makes this test highly attractive for performance based field applications.

Part IV

Conclusion

Chapter 8

Conclusions and Perspectives

The fracture model for scratch tests analysis and the proposed inverse application scheme developed constitute a step forward toward a better use of the scratch test for fracture testing of cohesive-frictional materials. Further developments could allow the scratch test technique to become a complementary tool to measure fracture properties of such materials at a micro-scale. We here summarize the main contributions and limitations of our work.

8.1   Main Findings

Our major results are:

1. Plastic yielding is dominant for small values of the projected horizontal load bearing contact area $A_{LB} = wd$. In particular at this scale there is a linear relationship between the horizontal force F_T and wd. For greater values of wd, size effects inherent to fracture processes appear.

2. A dimensional analysis of the scratch tests predicts that the dimensionless force $F_T/(K_c w \sqrt{d})$ depends only on materials properties, on the friction at the blade-material interface and on the width-to-depth ratio. A controlled scratch test experiment was designed, using paraffin wax as a model material, that confirmed the

scaling relation. In particular, the dimensionless force $F_T/(K_c w \sqrt{d})$ converged for great values of the width-to-depth ratio toward a constant value 1.42 ± 0.02 .

3. Two 2-D analytical model were developed to link the fracture toughness to the results of scratch tests. Both models rely on Linear Elastic Fracture Mechanics, especially the use of the J-Integral, to estimate the energy release rate. The first model assumes a constant uniaxial stress field in the structure and applies to scratch tests with an inclined blade. The second model applies to scratch tests with a back-rake angle, $\theta > 0$, and uses an Airy stress function approach for a better representation of the stresses. These models predict that, for large width-depth ratios, the normalized force $F_{eq}/(K_c w \sqrt{d})$ converges toward the square root of 2, as found in the experiments. The equivalent force F_{eq} is equal to the horizontal force if the blade is vertical; else it is equal to $\sqrt{F_T^2 + \frac{3}{5}F_V^2}$.

4. Finite Element simulations of force-controlled and displacement-controlled scratch tests help us define the domain of application of the model, which is restricted to small back-rake angles, $0 \leq \theta \leq 20°$. Moreover, the dominant fracture propagation mode appears to be mode II, plane shear fracturing.

5. An inverse application method is developed to assess the fracture toughness from scratch test data. This method involves two schemes. Experiments show a linear scaling between $F_{eq}/\sqrt{2}$ and $w\sqrt{d}$ for a given width. Moreover, the resulting slopes decrease with the width and then reach a plateau. Scheme 1 then approximates the fracture toughness by the asymptotic slope of F_{eq} versus $w\sqrt{2d}$ for a given width. In particular, convergence occurs for values of the width much larger than the fracture process zone of the material. On the other hand, scheme 2 estimates directly the fracture toughness by fitting the quantity $F_{eq}/(w\sqrt{2d})$ with a polynomial function or an exponential decay function of the width-to-depth ratio. In general an exponential decay fit yields a more accurate estimate.

6. The application of these methods in an industrial application (oil well cementing),

116

illustrates the relevance of the developed approach for engineering application.

8.2   Current Limitations and Future Perspectives

1. The analytical models developed and the expressions derived apply only to homogeneous linear elastic isotropic brittle materials. A non-linear material behavior such as viscoelasticity, viscoplasticity was not taken into account. Moreover the effect of internal residual stresses in the material were not considered.

2. In the fitting of the equivalent force F_{eq} versus $w\sqrt{2d}$, an initial offset appears, that could be attributed to an imperfect fracture geometry, friction effects at the blade-material interface, plastic dissipation phenomena or residual internal stresses, that are not considered in the derivation of the LEFM models.

3. Fracture dissipation occurs even at small scales. In fact the linear scaling between F_{eq} and $w\sqrt{2d}$ is valid even for small values of w. However the slope is much higher than the actual fracture toughness. Nevertheless, this scalability of the fracture toughness suggests first, that micro and even nano scratch tests could be used to access the fracture toughness at these scales. Secondly, it hints that the fracture toughness maybe greater at small scales, in which case there is a need of an upscaling model to relate nano and micro to macro fracture toughness.

8.3   Conclusion

The models presented in this thesis were developed to predict the fracture toughness from results of scratch tests. These models have proved to be applicable to a wide variety of materials: paraffin wax, Jurassic limestone, red sandstone, Vosges sandstone, cement-based materials, etc. Therefore, the scratch test appears to be an alternative to conventional fracture testing methods to measure the fracture toughness of materials, in particular when the interference of the fracture process zone is a limiting parameter.

Appendix A

MATLAB Script 1: Atkins [3, 4, 2] Fracture Interpretation

```
clear all;
%————Importing the scratch tests data————————

    allt=xlsread('Schlumberger'.'A1:G204');
d=allt(:,1);w=allt(:,3);Ft=allt(:,4);Fn=allt(:,5);stdFt=allt(:,6);stdFn=allt(:,7);
theta=15*pi/180;E=9200; % theta is the back-rake angle
p1=polyfit(Ft,Fn,1);
beta=atan(p1(1))-theta; %beta is the friction angle at the
                %blade-material interface
%-          -Initialisation of the main variables
phi=zeros(length(d),1); %phi is the shear plane angle
Gf=zeros(length(d),1); % Gf is the fracture energy
tauy=zeros(length(d),1); % tauy is the shear yield stress
Zeta=zeros(length(d),1); % Z is the ratio Gf/(tauy x d)
gamma=zeros(length(d),1); % gamma is the shear strain
    %              Estimation of the shear plane

Z=linspace(0.1,20,1000)'; %potential Z values
for i=1:length(d)
    x=d(w==w(i));y=Ft(w==w(i));
    p=polyfit(d(w==w(i)),w(w==w(i)),1);
    Phi=zeros(100,1);
    for j=1:length(Z)
    Phi(j)=newtonraph(theta,beta,Z(j)); % newtonraph uses a Newton-Raphson
                % mehtod to solve for phi
```

```
                %given theta, beta and Z
end
Gamma=cos(theta)./(sin(Phi).*cos(Phi+theta));
Q=1-sin(beta)*sin(Phi)./(cos(beta+theta).*cos(Phi+theta));
                %Q is the friction correction factor
IS=Z*d(i)./Gamma;
[B,IX]=sort(abs(IS-p(2)/p(1)));
gamma(i)=Gamma(IX(1));
phi(i)=Phi(IX(1));
Zeta(i)=Z(IX(1));
Gf(i)=p(2)*Q(IX(1))/w(i);
tauy(i)=p(1)*Q(IX(1))/(w(i)*Gamma(IX(1)));


end
```

Appendix B

MATLAB Script 2: Patel's [28]

Fracture Interpretation

```
clear all;

%           Importing the scratch tests data
allt=xlsread('Schlumberger','A1:G204');
d=allt(:,1);w=allt(:,3);Ft=allt(:,4);Fn=allt(:,5);stdFt=allt(:,6);stdFn=allt(:,7);


%————————non-linear fitting scheme for each width————————


f= @(x,xdata)x(1)+x(2)*xdata(:,1).*sqrt(1+2*xdata(:,2)/x(2));
x1 = lsqcurvefit(f,[1 1],[d(w==2.5) Fn(w==2.5)./(2.5*d(w==2.5))],Ft(w==2.5)./2.5,[ 0 0],[+Inf +Inf]);
x2 = lsqcurvefit(f,[1 1],[d(w==5) Fn(w==5)./(5*d(w==5))],Ft(w==5)./5,[ 0 0],[+Inf +Inf]);
x3 = lsqcurvefit(f,[1 1],[d(w==10) Fn(w==10)./(10*d(w==10))],Ft(w==10)./10,[ 0 0],[+Inf +Inf]);
x4 = lsqcurvefit(f,[1 1],[d(w==15) Fn(w==15)./(15*d(w==15))],Ft(w==15)./15,[ 0 0],[+Inf +Inf]);


%           Final Gf and sigmay
Gf=[x1(1) x2(1) x3(1) x4(1)]; %Gf is the fracture energy


sigmay=[x1(2) x2(2) x3(2) x4(2)];%sigmay is the tensile yield stress
```

Appendix C

Tensile testing of Paraffin Wax

C.1 Tensile tests: description

A finite plate with a hole at its center is submitted to a tensile load. The plate is clamped at its top and bottom extremities and the experiment is displacement-controlled. The geometric parameter of the problem are:

- w plate width

- B plate thickness

- H plate half-height

- R center hole radius

In the following section we will give an upper bound and a lower bound of the vertical force F^u when failure occurs.

C.2 Upper Bound Model

In the following section we assume the material to be perfectly plastic of yield stress σ_y and we give an upper bound of the yield stress that depends on the applied vertical force

F and on the geometric parameters of the problem. We also assume the structure to be in plane stress. Finally because of the double symmetry of the structure, we model only a quarter of it as described in Fig. C-1. In order to give a lower bound on σ_y we imagine
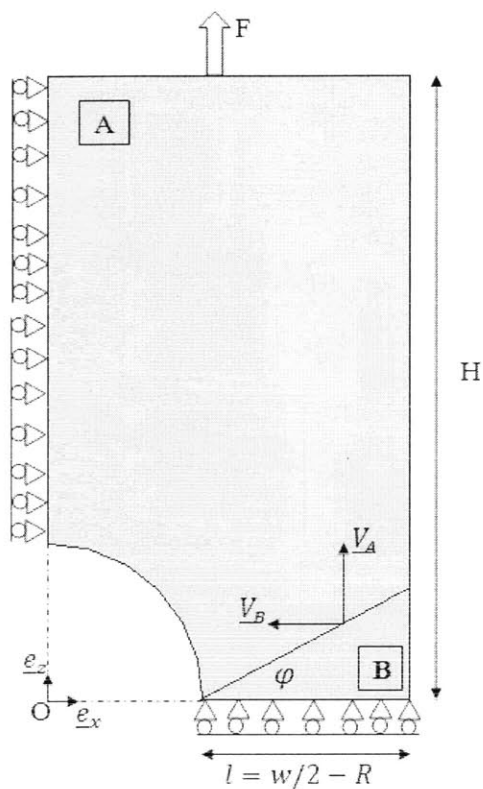
Figure C-1: Schematic description of the tensile test. One quarter of the hole sample is represented.

two sliding blocks, **A** and **B**. The velocity of block **A** is $\underline{V}_{\mathbf{A}} = V_A \underline{e}_y$. That of the block **B** is $\underline{V}_{\mathbf{B}} = -V_B \underline{e}_z$. The length of interface between **A** and **B** is:

$$l_{AB} = \frac{w/2 - R}{\cos \varphi} \tag{C.1}$$

and one of its unit normal is

$$\underline{n} = -\sin \varphi \, \underline{e}_x + \cos \varphi \, \underline{e}_z \tag{C.2}$$

122

For the velocity field to be kinematically admissible, we must have:

$$(\underline{V}_A - \underline{V}_B) \cdot \underline{n} = 0 \qquad (C.3)$$

which means : $-(0 + V_B) \sin \varphi + (V_A - 0) \cos \varphi = 0$. Therefore V_A and V_B are related by:

$$V_B = \frac{V_A}{\tan \varphi} \qquad (C.4)$$

To determine the upper bound, we need to calculate the internal dissipation rate, $\mathcal{D}_{int}$ corresponding to the assumed velocity field. In our case $\mathcal{D}_{int}$ is simply the shear force on the slip plane multiplied by the relative velocity across it. From the principle of virtual work, it comes that the external work rate is equal to the external work rate $\mathcal{W}_{ext}$ is equal to the sum of the internal plastic dissipation and of the strain energy stored in the system. Therefore the external work rate is always less than the internal plastic dissipation :

$$\mathcal{W}_{ext} \leq \mathcal{D}_{int}$$

The greatest value of the internal dissipation is when the stress on the slip plane is equal to the shear yield stress $k = \sigma_y / \sqrt{3}$:

$$\mathcal{D}_{int} \leq k \times l_{AB} \times |\underline{V}_A - \underline{V}_A| = k \times \frac{w/2 - R}{\cos \varphi} \times \sqrt{V_A^2 + V_A^2 \frac{1}{\tan^2 \varphi}}$$

The external rate of work corresponding to the assumed displacement field is:

$$\mathcal{W}_{ext} = FV_A$$

Therefore we always have:

$$\mathcal{W}_{ext} = FV_A \leq k \times \frac{w/2 - R}{\cos \varphi} \times \sqrt{V_A^2 + V_A^2 \frac{1}{\tan^2 \varphi}}$$

In particular for $\varphi = \pi/4$ and at collapse ($= F^u$), we have:

$$\frac{\sigma_y}{\sqrt{3}} 2(w/2 - R)V_A \geq F^u V_A$$

Finally the lower bound on σ_y is:

$$\sigma_y \geq \frac{\sqrt{3}}{2} \frac{F^u}{w/2 - R} \tag{C.5}$$
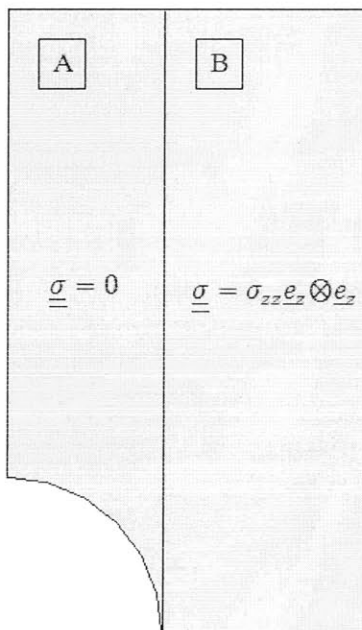

Figure C-2: Lower Bound model. Statically admissible stress field.

C.3   Lower bound model

We divide the structures in two regions **A** ($0 \leq x \leq R$)and **B** ($R \leq x \leq w/2$). We consider a field constant in each region: $\underline{\underline{\sigma}}_A = 0$ and $\underline{\underline{\sigma}}_B = \sigma_{zz}\underline{e}_z \otimes \underline{e}_z$. Such a field is

124

symmetric, satisfies the equilibrium conditions and the boundaries conditions implies:

$$\sigma_{zz} = \frac{F}{B(w/2 - R)}$$

Therefore such a field is statically admissible.

If we assume the material to obey a Von Mises criterion, therefore the potentially admissible fields are so that $\sigma_{zz} \leq \sigma_y$, which implies:

$$\forall \; F \; such \; that \; F \leq \sigma_y B(w/2 - R), \; F \; potentially \; admissible$$

The condition above is no longer true when the structure collapses:

$$F^u \geq \sigma_y B(w/2 - R)$$

This gives us an upper bound on σ_y.

In brief:

$$\frac{\sqrt{3}}{2} \frac{F^u}{B(w/2 - R)} \leq \sigma_y \leq \frac{F^u}{B(w/2 - R)}$$

which is:

$$0.866 \frac{F^u}{B(w/2 - R)} \leq \sigma_y \leq \frac{F^u}{B(w/2 - R)}$$

Bibliography

[1] Abaqus/Cac v.6. 9-1 User's Manual, Simulia, 2009.

[2] A. G. Atkins, Modelling metal cutting using modern ductile fracture mechanics: quantitative explanations for some longstanding problems. *International Journal of Mechanical Sciences* **45**(2): 373-396 (2003)

[3] A. G. Atkins and G. H. Liu, Toughness and the transition between cutting and rubbing in abrasive contacts. *Wear* **262**(1-2): 146-159 (2007).

[4] A. G. Atkins, The Science and Engineering of Cutting-The Mechanics and Processes of Separating, Scratching and Puncturing Biomaterials, Metals and Non-Metals. Butterworth-Heinemann, 2010

[5] L. Anand. *Lecture Notes on Mechanics of Materials*, MIT Department of Mechanical Engineering, Cambridge, February (2009).

[6] ASTM E399-90, Standard test method for plane-strain fracture toughness testing of high strength metallic materials. Philadelphia: American Society of Testing of Matererials; (1990).

[7] R. Bard, F.-J. Ulm, Scratch hardness strength solutions for cohesive-frictional materials. *International Journal for Numerical and Analytical Methods in Geomechanics*, DOI: 10.1002/nag.1008, In Press (2011).

[8] L.M. Barker, A simplified method for measuring plane strain fracture toughness, *Engineering Fracture Mechanics* **09**(2): 361-364 (1977)

[9] Z. P. Bažant, Size Effect in Blunt Fracture: Concrete, Rock, Metal. *Journal of Engineering Mechanics* (ASCE), **110**(4): 518-535 (1984)

[10] Z. P. Bažant, L. Cedolin, Stability of Structures: Elastic, Inelastic, Fracture and Damage Theories. New York: Oxford University Press. ISBN 0-486-42568-1, (1998).

[11] Z. P. Bažant, P. Jaime,Fracture and Size Effect in Concrete and Other Quasibrittle Materials. Boca Raton and London: CRC Press. ISBN 0-8493-8284-X. (1998).

[12] C. P. Bobko, B. Gathier, J. A. Ortega, F.-J. Ulm, L. Borges, Y. N. Abousleiman, The Nanogranular Origin of Friction and Cohesion in Shale-A Strength Homogenization Approach to Interpretation of Nanoindentation Results. *International Journal of Numerical and Analytical Methods in Geomechanics*, DOI: 10.1002/nag.984, 2010, In press.

[13] M. Bosma, K. Ravi, W. Van Driel, GJ. Schreppers, Design approach to sealant selection for the life of the well. SPE 1999; 56536.

[14] B.J. Briscoe, P. D. Evans, E. Pelillo, S. K. Sinha, Scratching maps for polymers, *Wear* **200**(1):137-147, (1996).

[15] E. Buckingham, On Physically Similar Systems; Illustrations of the Use of Dimensional Equations, *Physcial Review* **4** (4): 345376 (1914).

[16] C. Capacho, F. Baquero, K. Ravi, J. Vela, Cement design to optimize production in a highly active waterdrive reservoir, SPE 2007; 107701. (2007)

[17] GP Cherepanov, Crack propagation in continuous media, *Journal of Applied Mathematics and Mechanics* **31**(3): 503-512 (1967)

[18] B. Cotterell and Y.W. Mai, Slip-line field solutions of three-point bend specimens with deep notches, *International Journal of Mechanical Sciences* **22**(8): 2734 (1987)

[19] K. Duan, X. Hu and F. Wittman, Boundary effect on Concrete Fracture and Non-constant Fracture Energy Distribution, *Engineering Fracture Mechanics* **70**(16): 22572268 (2003)

[20] www.epslog.com

[21] M. Bonnet, A. Frangi, Analyse des solides déformables par la méthode des éléments finis. Les editions de l 'Ecole Polytechnique, ISBN : 2-7302-1349-X (2006).

[22] L.E. T. Ferreira, T. N. Bittencourt, J. L. A. O. Sousa, R. Gettu, *R*-curve behavior in notched beam tests of rocks, *Engineering Fracture Mechanics* **69**(17): 1845-1852 (2002)

[23] F. P. Ganneau, G. Constantinides, F.-J. Ulm, Dual-indentation technique for the assessment of strength properties of cohesive-frictional materials. *International Journal of Solids and Structures* **43**(6): 1727–1745 (2006) .

[24] X. Hu, An asymptotic approach to size effect on fracture toughness and fracture energy of composites, *Engineering Fracture Mechanics* **69**(5): 555-564 (2002)

[25] X. Hu and F. Wittman, Size effect on toughness induced by crack close to free surface, *Engineering Fracture Mechanics* **65**(2-3): 209-221 (2000)

[26] GR Irwin, Fracture strength of relatively brittle structures and materials, *Journal of the Franklin Institute* **290**(6): 513-521 (1970)

[27] H.Ollendorff and D.Schneider, A comparative study of adhesion test methods for hard coatings, *Surface Coating Technology* **113**(1-2): 86-102 (1999)

[28] Y. Patel *et al.*, Determining fracture toughness from cutting tests on polymers, *Engineering Fracture Mechanics* **76**(18): 27112730 (2009).

[29] P.E. Petersson, Fracture Energy of Concrete: Practical Performance and Experimental Results, *Cement and Concrete Research*, Cement and Concrete Research **10** (1): 91-101, (1980).

[30] www.polygonwax.com

[31] H. B. Ramirez, A. Santra, C. Martinez, A. X. Ramos, Gas-Migration Control and Mechanical Properties Improvement with a Right Angle-Set Slurry Design to Be Applied In a Production Cementing-Job for Ecuador. SPE 2009: 123085, (2009)

[32] N. X. Randall *et al.*, The Effect of Intrinsic Parameters on the Critical Load as Measured With the Scratch Test method, *Surface and Coatings Technology* **137**(2-3): 146-151, (2001).

[33] JR. Rice In: H. Liebowitz, Ed, *Fracture : an Advanced Treatise* Vol. 2 (Academic Press, New York, 1968)

[34] JR. Rice, Limitations to the small scale yielding approximation for crack tip plasticity, *Journal of the Mechanics and Physics of Solids* **22**(1): 17-26 (1974)

[35] T. Richard, E. Detournay, A. Drescher, P. Nicodème, D. Fourmaintraux, The scratch test as a means to measure strength of sedimentary rocks, SPE/ISRM 47196, DOI: 10.2118/47196-MS, (1998)

[36] G. Schei, E. Fjær, E. Detournay, C. J. Kenter, G. F. Fuh, F. Zausa, The Scratch Test: An Attractive Technique for Determining Strength and Elastic Properties of Sedimentary Rocks, SPE 63255, DOI:10.2118/63255-MS (2000).

[37] R. N. Singh and G. Sun, A numerical and experimental investigation for determining fracture toughness of Welsh limestone, *Mining Science and technology* **10** (1): 61-70 (1990).

[38] P. Suquet, *Rupture et Plasticite-Lecture Notes*, Editions de l Ecole Polytechnique, (2006)

[39] M. Thiercelin, C. Baumgarte, D. Guillot, A soil mechanics approach to predict cement sheath behaviour. SPE 1998: 47375, DOI: 10.2118/47375-MS, (1998)

[40] J. A. Williams, Analytical models of scratch hardness, *Tribology International* **29**(8): 675-694 (1996).

[41] F. Wredenberg and P.L Larsson, Scratch testing of metals and polymers: Experiments and numerics, *Wear* **266**(1-2):76-83 (2009)

[42] D.J. Wyeth and A. G. Atkins, Mixed mode fracture toughness as a separation parameter when cutting polymers, *Engineering Fracture Mechanics* **76** (18): 2690-2697 (2009)

[43] Y. Xie and H. M. Hawthorne, On the Possibility of Evaluating the Resistance of Materials to Wear by Ploughing Using a Scratch Method, *Wear* **240** (40180): 65-71,(2000).